

**Processing of Bi-2212 and Nb₃Sn
superconductors studied *in situ* by
high energy synchrotron
diffraction and micro-tomography**

by
Julian Kadar

**Diploma Thesis
2012**

Supervisor at CERN:
Christian Scheuerlein M.Sc.

Supervisor at
Friedrich-Alexander Universität Erlangen-Nürnberg:
Prof. Dr.-Ing. Peter Wellmann

CERN-THESIS-2012-206
04/01/2013



**FRIEDRICH-ALEXANDER
UNIVERSITÄT
ERLANGEN-NÜRNBERG**
TECHNISCHE FAKULTÄT

Acknowledgement

I would like to express my gratitude to all those people who have contributed to the completion of this project with their assistance and encouragement.

Special thanks go to my supervisor at European Organization for Nuclear Research (CERN), Christian Scheuerlein, and my academic supervisor at Friedrich-Alexander-Universität Erlangen-Nürnberg (FAU) Prof. Dr. Peter Wellmann for providing this interesting thesis work and giving invaluable support from the first steps of the project to the very end.

All experiments described in this thesis have been performed at the ID15 beam line at the European Synchrotron Radiation Facility (ESRF), Grenoble. The experiments have been set up by Marco Di Michiel, who has done the pre-processing of the diffraction and tomography data, too. The high pressure experiment was set up by Jérôme Andrieux who also supported me with training on X-ray diffraction analysis fundamentals.

It is a pleasure to have had a chance to cooperate with Mark Rikel from Nexans Superconductors GmbH with his great experience in Bi-2212 topics and the provision of precursor samples.

I want to thank Norberto Jimenez Mena for providing phase information on process wire samples with EDS.

The multifilament Bi-2212/Ag samples have been provided by the Applied Superconductivity Center (ASC) at the National High Magnetic Field Laboratory (NHMFL) in Tallahassee, Florida.

The single core Bi-2212/Ag sample has been provided by Oxford Instruments Superconducting Technology.

Erklärung

Ich versichere, dass ich die Arbeit ohne fremde Hilfe und ohne Benutzung anderer als der angegebenen Quellen angefertigt habe und dass die Arbeit in gleicher oder ähnlicher Form noch keiner anderen Prüfungsbehörde vorgelegen hat und von dieser als Teil einer Prüfungsleistung angenommen wurde. Alle Ausführungen, die wörtlich oder sinngemäß übernommen wurden, sind als solche gekennzeichnet.

Genf, den 27. November 2012

Julian Kadar

Abstract

Next generation superconducting wires have been studied to obtain more information on the evolution of phase growth, crystallite size and strain state during wire processing.

The high energy scattering beam line ID15 at the European Synchrotron Radiation Facility provides a very high flux of high energy photons for very fast *in situ* X-ray diffraction and microtomography studies of Bi-2212/Ag and Nb₃Sn/Cu wire samples. The typical wire processing conditions could be imitated in the X-ray transparent furnace at ID15 for diffraction and tomography studies.

Efficient data analysis is mandatory in order to handle the very fast data acquisition rate. For this purpose an Excel-VBA based program was developed that allows a semi-automated fitting and tracking of peaks with pre-set constraints. With this method, more than one thousand diffraction patterns have been analysed to extract d-spacing, peak intensity and peak width values. X-ray absorption micro tomograms were recorded simultaneously with the X-ray diffraction patterns during Bi-2212 processing in order to monitor microstructural changes. The influence of temperatures up to 900 °C and oxygen partial pressure on the Ag-Bi-Sr-Ca-Cu-O system in Bi-2212/Ag wires has been studied *in situ*. Inert gas and oxygen partial pressures of $P_{O_2} = 0.21$ and 21 bar have been used as process gas.

Without oxygen in the process gas, no Bi-2212 reformation is possible after the liquid state. Too much oxygen restrains the Bi-2212 crystal stability, making it melt already at 650 °C and preventing Bi-2212 recrystallisation during cool-down. The Bi-2212 filament size has no significant influence on the Bi-2212 decomposition and formation temperatures, but it strongly influences the Bi-2212 texture formation, as seen from the Bi-2212 diffraction peak intensity ratios.

The Nb₃Sn formation in Powder-In-Tube and Restacked-Rod-Process type wires has been compared by X-ray diffraction measurements during identical wire heat treatments.

Zusammenfassung

In dieser Arbeit wurde die Wärmebehandlung von supraleitenden Drähten *in situ* mittels Röntgenbeugung und Mikrotomographie untersucht. Die Beamline ID15 an der Europäischen Synchrotron Strahlenquelle (ESRF) in Grenoble bietet den erforderlichen sehr hohen Fluss von hochenergetischen Photonen, um schnelle *in situ* Röntgenbeugungs- und Mikrotomographiestudien an Bi-2212- und Nb₃Sn-Proben durchzuführen. Die typischen Wärmebehandlungen konnten im röntgentransparenten Ofen der ID15 Beamline nachgeahmt werden.

Die Auswertung der sehr großen Datenmengen, die während der Synchrotron Experimente gewonnen werden erfordert eine sehr effiziente Datenanalyse. Hierfür wurde ein auf Excel-VBA basierendes Programm entwickelt, um die Peakposition und die Peakbreite der Röntgendiffraktionen exakt zu bestimmen. Mit diesem Programm konnten über eintausend Beugungsmuster analysiert werden.

Während einer Bi-2212 Studie wurden gleichzeitig mit den Röntgenbeugungsmustern Röntgenmikrotomogramme aufgezeichnet, um die mikrostrukturellen Veränderungen während der Heizbehandlung untersuchen zu können. Der Einfluss des Sauerstoffpartialdruck bei Temperaturen von bis zu 900 °C auf das Ag-Bi-Sr-Ca-Cu-O System in Bi-2212/Ag Drähten konnte so *in situ* untersucht werden.

Ohne Sauerstoff im Prozessgas ist keine Bildung der kristallinen Bi-2212 Phase aus ihrem flüssigen Zustand möglich. Zu viel Sauerstoff hingegen verringert die Stabilität von Bi-2212 und bringt es bereits bei etwa 650 °C zum Schmelzen. Eine Rekristallisation von Bi-2212 ist bei einem Sauerstoffpartialdruck von $P_{O_2} = 21$ bar nicht mehr möglich. Der Faserdurchmesser beeinflusst die Schmelz- und Kristallisationstemperaturen von Bi-2212 kaum, jedoch konnte anhand der Intensitätsverhältnisse der Röntgenbeugungsmuster ein Einfluss der Filamentgröße auf die Kornorientierung beobachtet werden.

Die Bildung von Nb₃Sn in sogenannten Powder-In-Tube und Restacked-Rod-Process Drähten konnte mithilfe von Röntgenbeugungsmessungen während identischen Heizbehandlungen verglichen werden.

Table of Contents

1. Introduction.....	3
2. Basics	6
2.1. Manufacturing methods for multifilament superconducting wires.....	6
2.2. X-ray diffraction.....	10
2.3. Semi-automatic XRD peak fitting and tracking with Excel-VBA.....	17
2.4. X-ray absorption tomography.....	20
3. Description of the Bi-2212 and Nb ₃ Sn experiments.....	23
3.1. Samples.....	23
3.2. Applied heat treatments.....	24
3.3. Beam line setup at ESRF ID15.....	25
4. Analysis of XRD and μ -CT results acquired during the processing of Bi-2212/Ag wires.....	31
4.1. Diffraction pattern of Bi-2212 granulate.....	31
4.2. XRD of “green” Bi-2212/Ag wire (before HT).....	33
4.3. XRD of <i>ex situ</i> processed Bi-2212/Ag wire in 1 bar O ₂	35
4.4. XRD of <i>ex situ</i> processed Bi-2212/Ag wire quenched from 888 °C during in 1 bar O ₂ HT.....	38
4.5. <i>In situ</i> processing of multifilament Bi-2212/Ag wire in 1 bar air.....	39
4.6. Influence of the oxygen partial pressure on the phase evolution of a Bi-2212/Ag wire during the processing.....	47
4.7. <i>In situ</i> processing of multifilament Bi-2212/Ag wire in 100 bar air.....	51
4.8. <i>In situ</i> processing of single core Bi-2212/Ag wire in 1 bar air.....	55
5. Influence of process route and filament size on the Nb ₃ Sn growth in multifilament wires.....	66
5.1. Evolution of the Nb ₃ Sn and Nb diffraction peak areas.....	68
5.2. Nb ₃ Sn lattice parameter evolution.....	70
5.3. Nb ₃ Sn diffraction peak width.....	72
5.4. Asymmetry of Nb ₃ Sn diffraction peaks.....	73
6. Discussion.....	74
6.1. Influence of oxygen partial pressure on the phase evolution in Bi-2212/Ag wires.....	75
6.2. Comparison of Bi-2212 phase evolution and crystallite orientation in multifilament and single core wires.....	75
6.3. Second phase formation during the Bi-2212/Ag wire processing.....	76
6.4. Crystallite size evolution during the Bi-2212/Ag wire processing.....	77
6.5. Influence of process route and filament size on Nb ₃ Sn formation.....	77
7. Conclusion.....	79
8. Abbreviations.....	80
9. Bibliography.....	82

1. Introduction

The European Organization for Nuclear Research (CERN) near Geneva, Switzerland is the world's largest laboratory for particle physics. CERN's mission includes fundamental research, technology transfer and education. Thousands of scientists from all over the world come to do experiments, mostly in collaboration with their home institute, to the high energy particle accelerators hosted by CERN.

The Large Hadron Collider (LHC) [1] is a synchrotron collider housed in a 27 km long tunnel. In the vacuum tubes of the LHC, two counter-rotating beams are accelerated. The pre-acceleration of the particles is done by smaller accelerators (e.g. LINAC, PS and SPS) on the CERN site and they are injected at 450 GeV into the LHC that accelerates them to a nominal energy of 7 TeV per beam. The maximal collision energy of the LHC is thus 14 TeV. Collisions take place at the four experiments ALICE, ATLAS, CMS and LHCb. Each experiment is built up of detectors around the collision point that allow characterising the decay products created during a collision.

1232 main dipole bending magnets and more than 400 main quadrupole focusing and defocusing magnets, which can reach a nominal field of 8.3 Tesla, are used to guide the LHC beams. In accelerator magnets, such high fields can only be reached with superconducting magnet coils. A cross section of the LHC dipole magnets is shown in Figure 1.

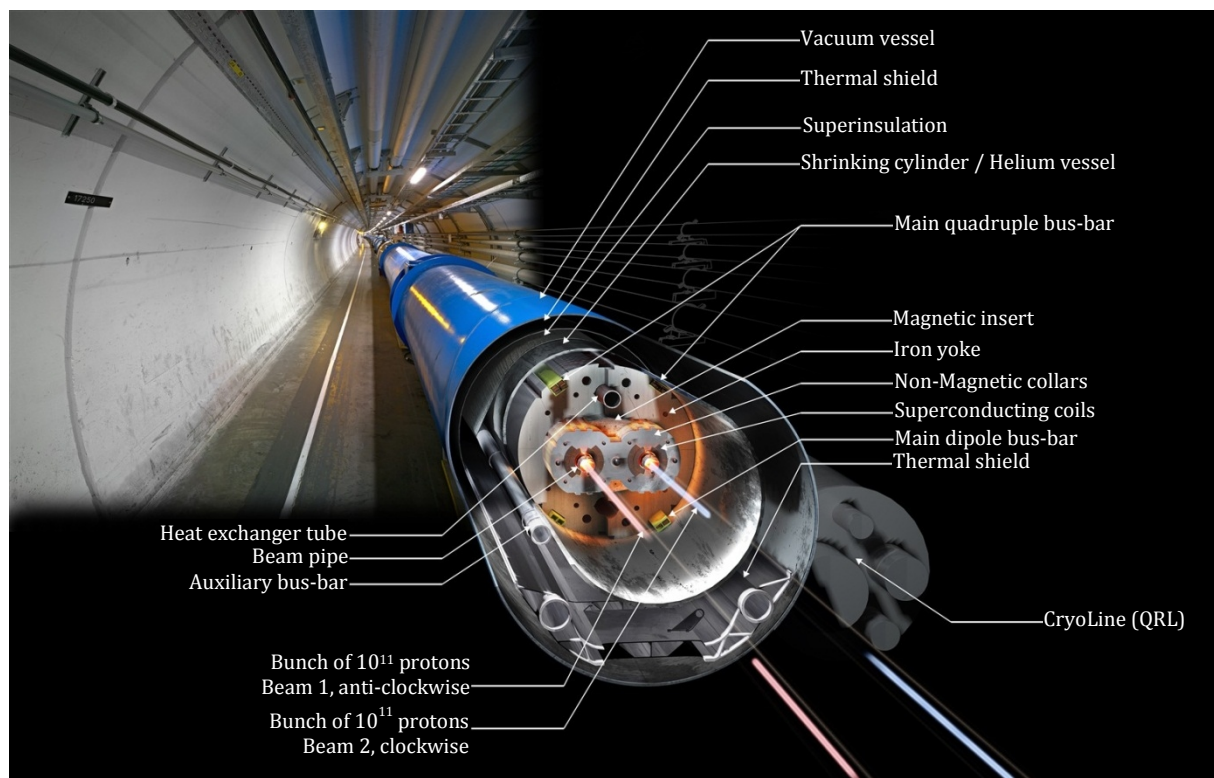


Figure 1 | Photograph inside the LHC tunnel including a 3D rendered cross section of the dipole bending magnets [2].

The superconductor used in the LHC magnet coils is a Nb-Ti alloy [3], which can provide the high current densities needed to reach the field of 8.3 T when cooled down to 1.9 K with superfluid helium.

The main goal of future LHC upgrades is to increase the collision rate and later the collision energy. The probability of particles colliding can be increased by reducing the beam size at the collision region in the experiments. This can for instance be achieved by replacing a few focusing magnets close to the interaction points by focusing magnets that can reach higher fields. For a beam energy increase, all bending magnets that keep the particles on orbit need to be replaced by magnets that can reach higher fields [4].

In order to achieve substantially higher magnetic fields, superconductors that can reach very high critical currents at higher fields than Nb-Ti alloy superconductors have to be used. An overview of the critical current density versus applied field is presented in Figure 2 for different superconductors at 4.2 K. The plot presents clearly the advantages of wires using new superconducting materials like YBCO, MgB_2 , Bi-2223, Nb_3Sn or Bi-2212 over the current Nb-Ti wires.

Unlike the ductile Nb-Ti alloy, which has excellent mechanical properties [5], all superconductors which reach high critical currents at higher fields are brittle. This makes it impossible to use the manufacturing techniques applied for the ductile Nb-Ti wires. Instead separated wire draw with ductile precursor, coil winding and subsequent heat treatment for superconducting phase formation are necessary.

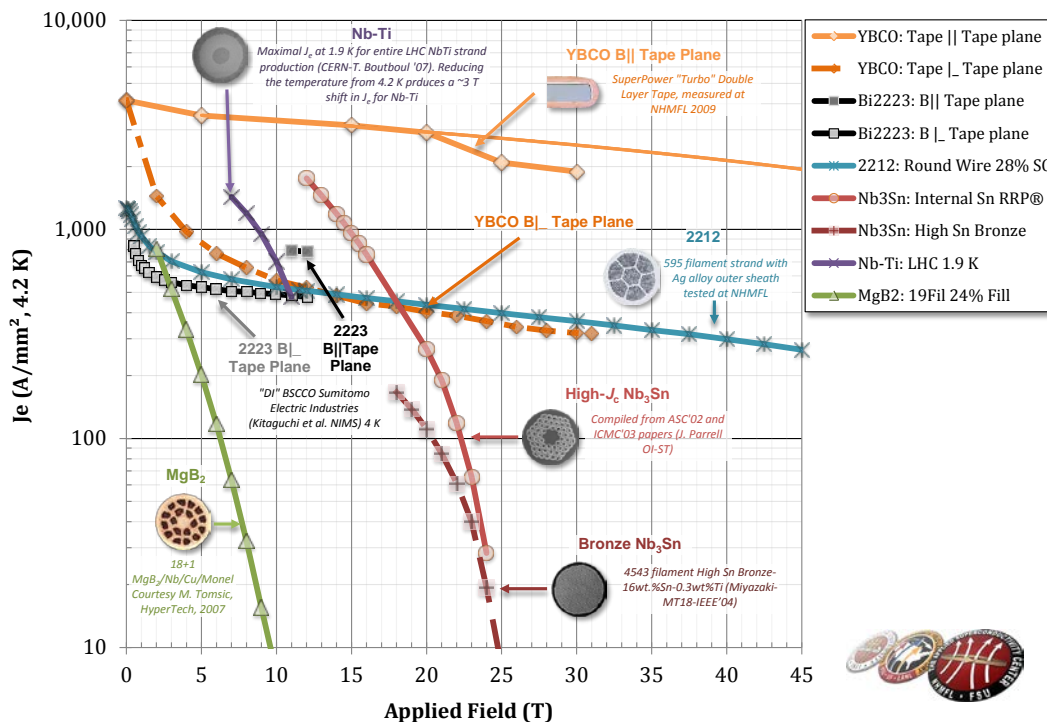


Figure 2 | Critical current density of superconducting wires currently available or in development as a function of critical applied field at 4.2 K [Courtesy Peter Lee, National High Magnetic Field Laboratory, Florida [6]]

Two types of the above mentioned materials will be analysed and discussed in this thesis, namely Nb_3Sn and Bi-2212. The characterisation of both materials during processing will be described on the basis of high energy synchrotron X-ray diffraction and micro tomography

experiments at the ID15 beam line of ESRF in Grenoble. Both techniques allow a non-destructive analysis of the wires during application of the heat treatments.

2. Basics

The samples studied in this thesis are round wires that were fabricated via the Powder-In-Tube (PIT) [7] [3] process or the Internal-Tin process (in the following referred to as Restacked Rod Process (RRP) [8]. A short description of their manufacturing principles and the initial precursor phases will be given. The *in situ* analyses of the samples are based on X-ray diffraction and X-ray absorption tomography. The basics of both methods are briefly explained below.

2.1. Manufacturing methods for multifilament superconducting wires

Nb₃Sn and Bi-2212, the materials that are presented in this thesis, can both be produced in multifilament round wire shape which is beneficial for magnet coil winding. A multifilament wire is basically built up of tens to hundreds of continuous parallel superconducting filaments surrounded by a normal conducting wire matrix. While the superconducting filaments are mainly responsible for the current flow, the normal conducting matrix provides mechanical, thermal and electrical stability. For example, when a single filament has a material defect that intersects the current flow, the normal conducting matrix can bridge and distribute the current to the surrounding filaments and the function of the wire is preserved.

Wires can be manufactured of ductile materials in a draw or extrusion process. As Nb₃Sn and Bi-2212 are brittle, they cannot be formed directly. Depending on the material, different solutions are available to bypass material forming limits. One possibility is to insert the brittle filament material into the wire matrix in powder form (Powder-In-Tube, PIT), so that the plasticity of the wire is preserved. Another option is to use ductile base materials which can be transformed to into the desired final phase by subsequent heat treatment (e.g. Restacked-Rod-Processing, RRP).

2.1.1. Powder-In-Tube (PIT) process for Bi-2212/Ag wire manufacturing

The Powder-In-Tube (PIT) process to manufacture Bi-2212/Ag wires is based on a composition of a ductile Ag matrix, pure Ag tubes and Bi-2212 powder filling [7]. Figure 3 shows a tomographic cross section of a Bi-2212/Ag wire [9] that has been studied here, before heat treatment.

As a first step, a granular Bi-2212 precursor is produced in a melting, casting and grinding process. The granular precursor is then filled into Ag tubes and drawn into hexagonal single core strands. In order to achieve Bi-2212 filament connectivity, the Bi-2212 needs to be melted and re-formed during HT in an atmosphere containing oxygen [10]. Ag is suitable as matrix material for Bi-2212/Ag wires as it has a higher melting point than Bi-2212 and allows oxygen diffusion into the filaments [11]. The hexagonal strands are then assembled into wires in multifilament configuration inside a Ag-Mg sheath with 0.2 wt.% Mg, and drawn to the final diameter. Mg alloy improves the mechanical properties of the wire.

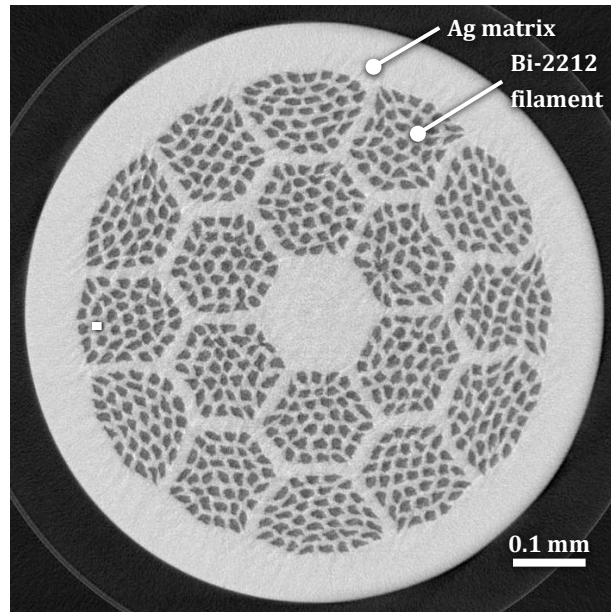


Figure 3 | Transverse tomographic cross section of the Bi-2212/Ag wire sample as drawn, before any HT. The Ag matrix is shown in light grey and the Bi-2212 filaments in dark grey.

A major problem of processing Bi-2212/Ag wires with the PIT technique affecting the critical current density of the transformed wires is the growth of voids in the filament. This has been studied by Kametani et al [12] and Scheuerlein et al [10] with *in situ* X-ray absorption tomography on multifilament wires and will be studied further within this thesis on a single filament of larger diameter.

The Bi-2212 crystal structure was studied in depth by Matheis and Snyder [13] and described as an orthorhombic structure with lattice parameters $a = 5.408(1) \text{ \AA}$, $b = 5.408(1) \text{ \AA}$ and $c = 30.869(2) \text{ \AA}$, with a modulated superstructure containing an additional oxygen atom in the bismuth oxide layer. Figure 4 presents a single, non-modulated unit cell of the Bi-2212 crystal.

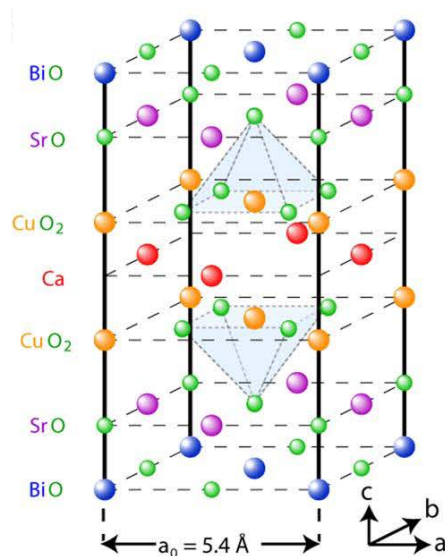


Figure 4 | Crystal structure of the Bi-2212 unit cell [14].

During heat treatment, other undesirable phases can be formed. Assal [15] has studied in detail the thermodynamics of the Ag-Bi-Sr-Ca-Cu-O system in thin layers processed in 0.21 bar oxygen. Figure 5 shows the phase diagram of the Bi-2212-Ag system in a temperature range of 1120 to 1220 K and a molar Ag content of 0.0 to 0.1. This information can be taken as a first estimate of possible phase formation during the wire heat treatments applied here.

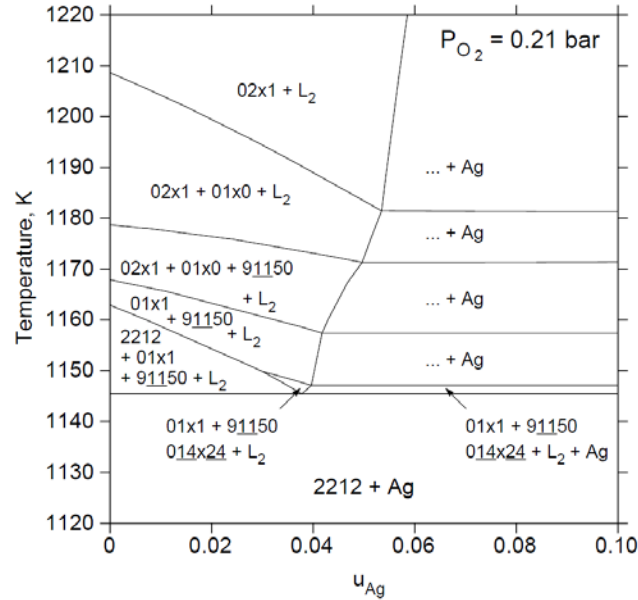


Figure 5 | Phase diagram of Bi-Sr-Ca-Cu-O and Ag at 0.21 bar oxygen partial pressure [15].

Table of reference diffraction patterns for Bi-2212 experiments

A summary of reference diffraction patterns used for comparison to the diffraction patterns acquired during the Bi-2212/Ag experiments is listed in Table 1.

Table 1 | Reference diffraction patterns for the analysis of Bi-2212/Ag wires.

Material	ICSD PDF#	Author
Bi-2212		Matheis et al. [13]
Bi-2201	46-0041	
2:3CF = Bi₂Sr₂CaO_{6+x}	46-0497	
(Ca_{0.4}Sr_{0.6})CuO₂		
Cu₂O	05-667	
Ag	89-3722	

2.1.2. Powder-In-Tube (PIT) process for Nb₃Sn/Cu wire manufacturing

The Powder-In-Tube process for Nb₃Sn/Cu wires [3] is fundamentally different from the Bi-2212 PIT process as it relies not on filament melting but solid state diffusion. The filaments are made of Sn and Nb₂Sn powder in Nb tubes. The matrix is made of high purity Cu. Figure 6 shows a metallographic cross section before reaction (a) and a backscatter electron image focusing on a

filament after 60 h of heat treatment at 620 °C (b). A drawback of the Nb₃Sn PIT process is the formation of intermediate phases like NbSn₂ and Nb₆Sn₅, which cause coarse grains with lower Sn content (~22.5 at.% instead of ~24.5 at.% in fine grains [16]) and lower critical current as the desired fine grains [17].

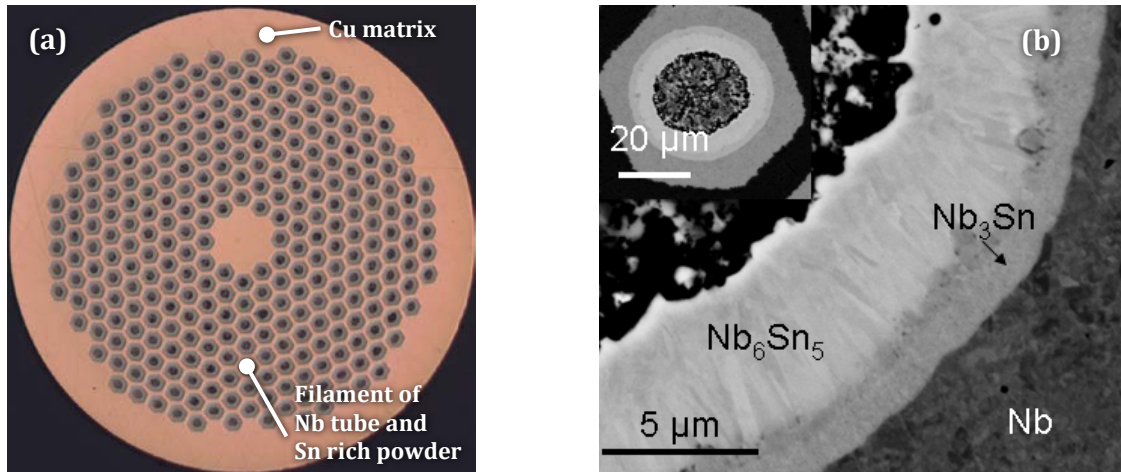


Figure 6 | (a) Optical microscopic image of a non-reacted Nb₃Sn/Cu PIT wire ($\varnothing = 1.25$ mm) (b) Backscatter electron image of a single filament in a Nb₃Sn/Cu PIT wire after 620 °C - 60 h heat treatment [Courtesy G. Arnaud and C. Scheuerlein, CERN]

With the PIT manufacturing process, the Nb₃Sn phase forms as coarse and fine grains during the heat treatment. The fine grains are located as an outer filament ring next to the Nb tubes and the coarse grains as an inner ring next to the porous non-Nb₃Sn phase in the centre. The grain size has an influence on magnetic flux pinning [18].

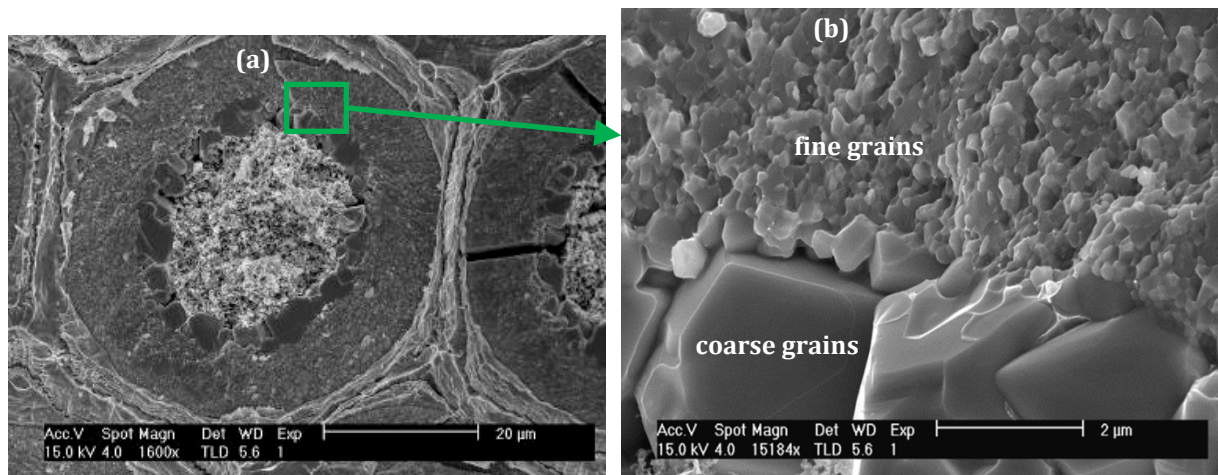


Figure 7 | SEM image showing (a) a reacted filament cross section inside a PIT wire and (b) in more detail the Nb₃Sn phase with fine (~180 nm) and coarse (> 1 μm) grains. [Courtesy M. Cantoni, EPFL Lausanne.]

2.1.3. Restacked-Rod-Processing (RRP) process for Nb₃Sn/Cu wire manufacturing

Restacked-Rod-Processing (RRP) [8] is a process where the Nb filaments are assembled around a Sn core within a common Cu matrix. An outer sheath (Nb or Nb(Ta)) prevents Sn diffusion into the Cu matrix of the wire. The chemical reaction of Sn and Nb happens by Sn diffusion through the Cu matrix, where Nb₃Sn in A15 crystal structure is the desirable final composition [19]. The

intermediate phases that are formed during the processing are, for instance, NbSn_2 and Nb_6Sn_5 . A cross section of a reacted [20] RRP wire is shown in Figure 8.

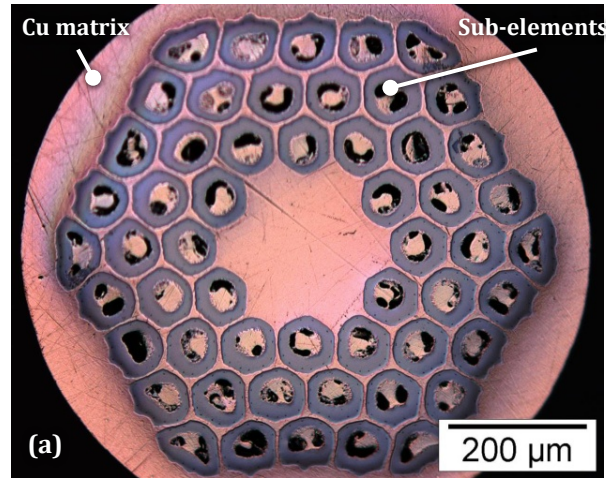


Figure 8 | Cross section of a reacted RRP wire [20].

2.2. X-ray diffraction

X-ray diffraction (XRD) is a method to analyse distances between atoms in a crystal structure [21]. The analysis is based on Bragg's equation (Equation 1), which gives the angles of constructive interference as a function of X-ray wavelength and interatomic distance. In angular dispersive XRD, the wavelength of the X-ray beam is known, the diffraction angle is measurable, and thus the distance between lattice planes can be calculated.

$$2d\sin(\theta) = n\lambda \text{ with } n \in \mathbb{N}$$

Equation 1 | Bragg's equation. (d : d-spacing in Å, 2θ : diffraction angle, λ : photon wavelength in Å)

The K-alpha radiation of copper ($E_{\text{Cu K}\alpha 1} \approx 8.03 \text{ keV}$ [22]; $\lambda_{\text{Cu K}\alpha 1} \approx 1.54 \text{ \AA}$) is commonly used to do XRD studies in laboratories. Instruments with a Cu K α X-ray source are broadly available as stand-alone and desktop versions for reasonable prices. Due to the high absorption rate of Cu-K α radiation in metallic samples, only thin slices can be analysed in transmission geometry. A possibility to bypass the absorption of Cu-K α radiation is the reflection configuration, wherefore the sample has to be prepared with destructive metallurgy methods.

With a synchrotron X-ray source as provided by ESRF, very high photon energies are available (at beam line ID15, energies as high as 500 keV are possible). The comparatively low absorption of high energetic photons in the sample allows analysing the samples in transmission geometry. Due to the high flux of photons, fast XRD pattern recording is possible that allows analysing time dependent changes in the samples.

Due to the classical reflection geometry used in XRD instruments, results are mostly presented as a function of 2θ in literature. Using constant wavelength Cu-K α radiation, the results of individual experiments are easily comparable to each other. But with the use of other X-ray

energies and especially synchrotron beams where the wavelength can vary from experiment to experiment to optimise photon transmission, the use of the 2θ angle is not very practical. Instead, the reciprocal lattice vector Q is used. Q does not vary with energy but is only dependent on the d-spacing of the crystal being studied (see Equation 2).

$$Q = \frac{2\pi}{d}$$

Equation 2 | Conversion rate of reciprocal lattice vector Q and d-spacing d .

The usage of the lattice plane distance d as x axis of an XRD plot can be misleading for analysis, even though it gives straightforwardly readable information on the lattice plane distances. Considering Equation 1 of Bragg's theorem above, a linear x axis of d would result in very little information at high values of d , with most of the information concentrated at low values of d . With the exception of the direct mapping of peaks to the d-spacing of crystallites, all analysis of XRD data is highly hindered. Choosing a linear x axis of Q instead, the diffraction peaks get homogeneously distributed over the diffraction pattern, similarly to the use of 2θ . Additionally, with the use of 2θ or Q , peak broadening effects (details below) appear almost identically on a large angular scale. This is important to allow comparing the peaks of a pattern and extracting information.

The X-ray diffraction patterns acquired during the experiments were recorded in the so-called Debye-Scherrer configuration [23]. The beam reaches the sample, crosses it and a fraction of the photons gets "diffracted" according to Equation 1. Since in this experiment, the photon source and the sample do not move and the photon beam is parallel, the angle between the beam axis and the diffraction rings acquired with the CCD has to be considered as 2θ .

2.2.1. Recording of X-ray patterns

An XRD pattern of a LaB_6 reference powder sample recorded with a 2D planar detector is presented in Figure 9 as an example. The Laue spots [24] resulting from diffraction on the single crystallites overlap to form closed circles on the detector due to the high amount and random orientation of the crystallites held in the X-ray transparent glass capillary. If the orientation of the crystallites were not random but it had preferred directions, then the rings would show circular inhomogeneities. The intensity ratios between entire diffraction rings compared to an ideal reference powder of the same material without texture would be affected as well.

In the example presented, the detector centre shows an absence of intensity. Using a parallel synchrotron beam for XRD, most of the beam intensity is transmitted through the sample without attenuation. To avoid damaging the photo-sensitive pixels of the detector by the high amount of photons, a lead photon absorber is placed in front of the detector. The diffuse intensity visible around the detector centre is random photon scatter, partly on the sample and partly on the air.

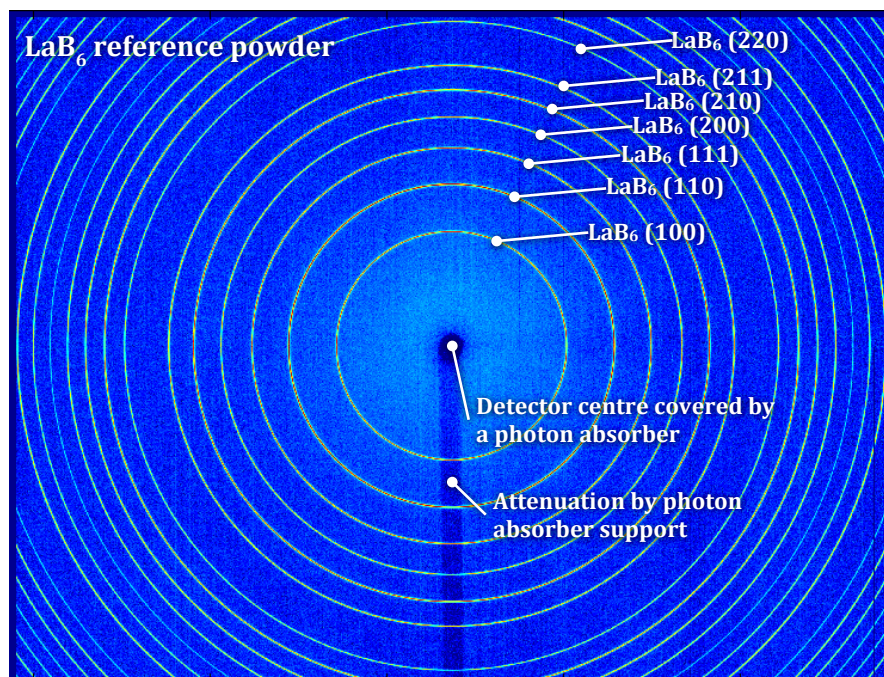


Figure 9 | Diffraction pattern of LaB₆ reference powder as recorded with a Trixell Pixium 4700 detector. Diffraction rings are labelled according to their Miller Indices.

Most XRD analysis techniques are based on patterns of diffraction intensity as a function of diffraction angle. To obtain this format, the intensities recorded and presented on the 2D pattern above have to be summed up circularly around the circumference of the concentric diffraction rings. Diffraction angle can then be determined by trigonometry based on the sample-to-detector and centre-to-diffraction ring distances. Subsequently, Q and d can be derived based on the known beam energy.

Figure 10 shows the circularly integrated diffraction pattern of the LaB₆ reference powder sample corresponding to Figure 9. With the settings used, the rectangular sensitive surface of the detector allows the registration of entire diffraction rings up to $Q \approx 4.4 \text{ \AA}^{-1}$, that is, down to $d \approx 1.4 \text{ \AA}$. The very low angles that are absorbed by the Pb photon dump have to be disregarded. The d -spacing range that can be recorded varies with beam energy, detector area and sample-to-detector distance.

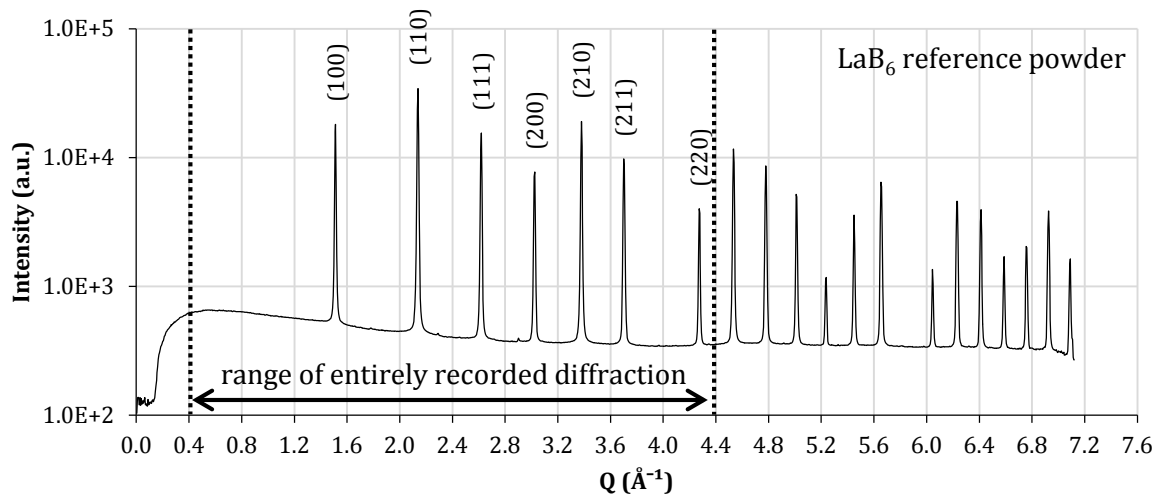


Figure 10 | Circularly integrated diffraction pattern of LaB_6 reference powder held in a glass capillary, acquired at RT, labelled with Miller Indices.

2.2.2. Analysis of diffraction patterns

The diffraction peak position, peak intensity and peak shape can be exploited to characterise the sample. The lattice structure of the observed crystalline phase with its plane distances is responsible for the peak positions, while peak intensity ratios are influenced by the atomic composition. The texture that describes preferred crystallite orientation in polycrystalline samples influences the intensity ratios as well. The peak shape, often reduced to peak width or integral breadth, is determined by crystallite size and its distribution, inhomogeneous strain and/or impurities in the lattice.

Phase volume vs. peak intensity

One property of interest during heat treatment is the evolution of the volume of certain phases in the studied sample. This can be observed through peak intensity, which is almost linearly dependent on the amount of similar unit cells forming a crystalline phase. To measure the diffraction intensity of a phase, all diffraction peaks have to be summed up. In practical use, the sum of several peaks that cover the three main lattice plane orientations is sufficient, because, according to the n in Scherrer's equation, most of the peaks at higher angles are only repetitions of lower angle peaks. The intensity analysis of texture free phases can even be reduced to a single peak because the intensity ratios of all other peaks remain constant. The intensity measurement of each single peak is approximated by first defining local peak boundaries that are usually where the intensity is not distinguishable from the background scatter anymore, and second, subtracting background scatter within these boundaries. An approximation of background scatter by linear interpolation between the intensity values at the boundaries of the relevant peak is a reliable method in most cases. With nearby peaks, or even peak superposition, the definition of peak boundaries requires relying on hypotheses and this method of background subtraction loses in reliability. After correct background subtraction, the intensity data which represents the photon count on the detector pixels can simply be summed up to obtain the peak intensity.

Fitting of X-ray diffraction peaks

To extract further information from the diffraction peak than the intensity, peak fitting is obligatory. In contrast to the discrete data of a recorded diffraction pattern that is a kind of a histogram, the continuous curve of a proper fitting function allows various analyses. The choice of the fitting function needs to have a physical basis to obtain reliable results. Prominent peak broadening effects, as for example anisotropic strain of crystallites, result in a symmetric normal distribution that is described by the Gaussian function (see Equation 3). Identically small sized crystallites show a normal distribution of the scattering angle as well, but the superposition of various sized crystallites in the same phase results in a cumulative distribution as described by the Lorentzian function (see Equation 4). The smooth transition between the two characteristic curves is achieved by using the Voigt function, which is a convolution of both with a weighting factor η . Due to computational constraints, the Voigt function is usually approximated with the pseudo-Voigt function (see Equation 5).

$$G(x) = \frac{1}{\sigma\sqrt{2\pi}} e^{-\frac{(x-x_0)^2}{2\sigma^2}}$$

Equation 3 | Gaussian function. σ^2 : variance; x_0 : expectation

$$L(x) = \frac{1}{\pi} \left[\frac{\gamma}{(x-x_0)^2 + \gamma^2} \right]$$

Equation 4 | Lorentzian function. γ : half-width at half-maximum; x_0 : expectation

$$V_p(x) = \eta L(x) + (1 - \eta)G(x) \text{ with } 0 < \eta < 1$$

Equation 5 | pseudo-Voigt function. $G(x)$: Gaussian function; $L(x)$: Lorentzian function.

In addition to a visual check of the fit, its quality can be quantified by calculating the profile R-factor (see Equation 6) [25]. R_p is then basically the difference between the measured and calculated data divided by the sum of measured data. A squared weighting of data deviation yields sensitivity to strongly deviating single data points.

$$R_p = \sqrt{\left(\sum_{i=1}^N (y_i - b_i - g_i)^2 \right) / \left(\sum_{i=1}^N (y_i - b_i)^2 \right)} \text{ with } i \in \mathbb{N}$$

Equation 6 | Profile R-factor R_p , i : data identity, N : number of data points, y_i : measured value, b_i : background value, g_i : function value.

Peak broadening induced by the instruments

In the studies presented here, instrument-induced diffraction peak broadening is mainly affected by the beam bandwidth, causing slightly varying diffraction angles dependent of the wavelengths and the detector pixel pitch. To measure instrument-induced peak broadening, a

reference sample (e.g. LaB₆ reference powder) that causes little sample induced peak broadening can be used.

The beam bandwidth has to be adjusted respecting two major criteria. It should be the narrowest achievable with this instrument, while maintaining a sufficient photon flux in order to achieve a high signal to noise ratio which is important for detailed peak analysis. A special compromise has to be found for combined XRD and μ -CT studies, as performed during this work. For X-ray absorption tomography, the photon flux has to be considerably higher than in XRD studies to keep exposure time short. Thus, combined *in situ* XRD and μ -CT recordings can only be executed with a high bandwidth, which causes high instrument-induced broadening.

An example of three different settings affecting instrumental peak broadening is presented in Figure 11. Best results for XRD measurements have been obtained with a small beam bandwidth (here ~ 25 eV of a 81 keV beam) and a high sample to detector distance.

To have sufficient photon flux for μ -CT recordings, the bandwidth has to be increased (here, it is about 800 eV) which increases the instrument-induced peak broadening. The medium bandwidth example is a compromise of the high bandwidth experimental setup optimised for XRD-only measurements, enabling μ -CT without major modifications in the beam line setup.

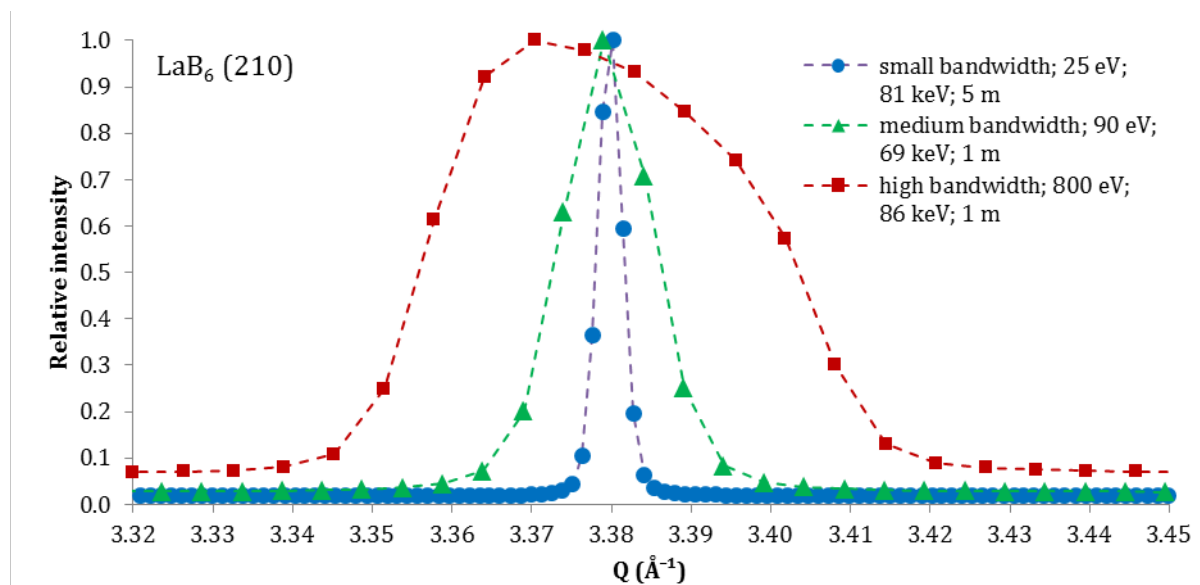


Figure 11 | LaB₆ peak of three diffraction pattern with a narrow bandwidth and an inhomogeneous broad bandwidth.

Peak broadening induced by the sample

The reasons for sample-induced broadening are manifold and cannot always be distinguished definitely. Defining constraints with knowledge of sample properties obtained in other experiments helps to iteratively specify the remaining effects.

Two major reasons for sample induced peak broadening are presented here: crystallite size and anisotropic strain. Details on further reasons are explained for example by Ungár [26].

Small crystallites in a phase increase the amount of boundaries where interatomic distances in the lattice vary slightly. Paul Scherrer described the dependence of peak broadening on crystallite size and diffraction angle (see Equation 7). The width of a peak increases with decreasing crystallite size. The effect is stronger at high diffraction angles.

$$B_{size} = \frac{K\lambda}{L\cos(\theta)}$$

Equation 7 | Scherrer's theorem to describe the relation between crystallite size and peak broadening. B_{size} : integral breadth of the peak; K : material specific constant. Usually simplified to 0.9; λ : wavelength in Å; L : crystallite size in Å; θ : diffraction angle of the peak. [27]

When crystallites are under the influence of random individual strain, the effect of all the small diffraction angle differences results in a broadening of the peak. Just like crystallite size-induced broadening, anisotropic strain-induced broadening is angle dependent as well. Equation 8 gives a relation between peak broadening, anisotropic strain and global diffraction angle. Unlike anisotropic strain, uniform strain would solely expand/contract the lattice in a uniform way leading to a shift of the lattice parameters without peak broadening.

$$B_{strain} = 4\varepsilon_0\tan(\theta)$$

Equation 8 | Relation between strain and peak broadening. B_{size} : integral breadth of the peak; ε_0 : average crystallite strain; θ : angular position of the peak.

In favourable cases, the different angular dependences of the two broadening effects allow distinguishing between size- and strain-induced peak broadening, provided a sufficiently wide angular range is recorded.

In the recorded diffraction patterns, all broadening effects combined result in a total peak width. In Figure 12, the influence of the three effects is presented as a simulation for a typical situation. The larger the recorded Q range, the stronger are the differences between strain- and grain size-induced peak broadening. The dotted lines indicate the Q range recorded during the Bi-2212 diffraction experiments described here.

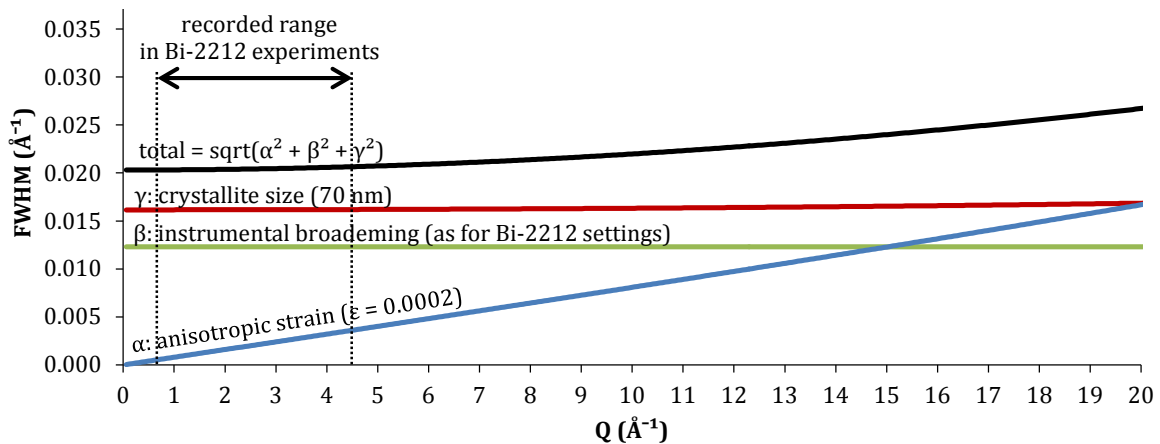


Figure 12 | Simulation of instrument-, crystallite size- and anisotropic strain-induced peak broadening effects as a function of diffraction angle.

2.3. Semi-automatic XRD peak fitting and tracking with Excel-VBA

For a fast and precise analysis of the diffraction patterns recorded *in situ*, multiple tools were developed in the context of this thesis. The most comprehensive tool, which is based on Microsoft Excel and its integrated Visual Basic for Applications (VBA), will be presented here. Basically, the tool allows fitting individual peaks of an XRD dataset with the Gaussian, Lorentzian or pseudo-Voigt function. The superposition of two curves to a conjoint fit is possible as an option. After a successful initial static fit, a VBA routine advances automatically through the dataset and refits the functions to each diffraction pattern iteratively. The progress speed of the routine is approximately one diffraction peak per second (including peak fitting and measurement of peak area, d-spacing and width). The acquired parameters of each fit and their evolution are then summarised in a separate spreadsheet. Preview plots present the evolution of peak intensity, lattice parameter and peak width as a function of HT duration and temperature.

Data input (database)

Data input is carried out through a specifically tailored spreadsheet, designed for easy pasting of tabulator separated ASCII values from XYE files commonly used in XRD, containing XRD datasets after circular integration and pre-processing. This spreadsheet operates as a database that has to be filled once and is not modified at any time afterwards. The first four lines contain information about file number (ID of each diffraction pattern), time and temperature. The first three columns on the left contain the diffraction angle 2θ , the reciprocal lattice vector Q and the lattice plane spacing constant d . The further cells contain the intensity (i.e., photon count) assigned to each recorded diffraction angle (see Figure 13).

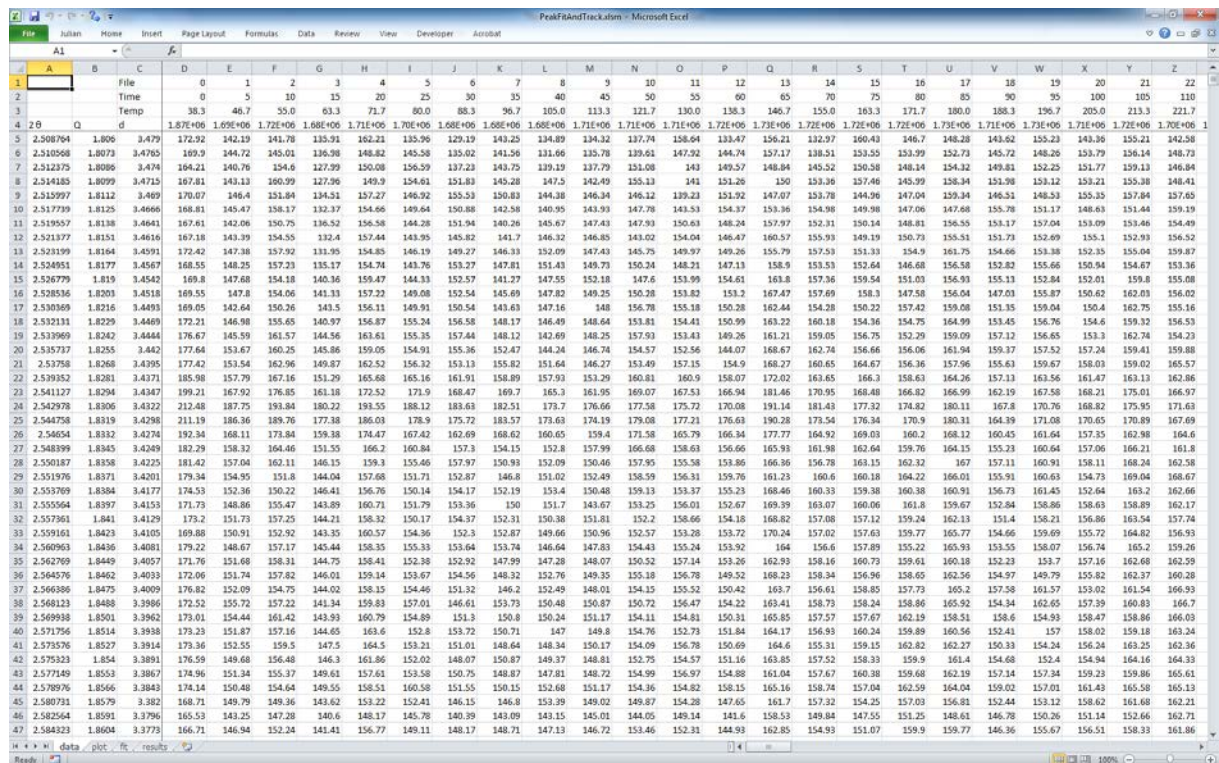


Figure 13 | Screenshot of the data input sheet in “PeakFitAndTrack.xlsm” tool.

Preview of entire diffraction pattern

The XRD-plot preview sheet (see Figure 14) provides a graph showing a selected diffraction pattern of the dataset. This preview of the XRD data is useful for peak identification, to facilitate the settings for the subsequent peak fit. The horizontal axis of the plot can be set to be a function of 2θ , Q or d .

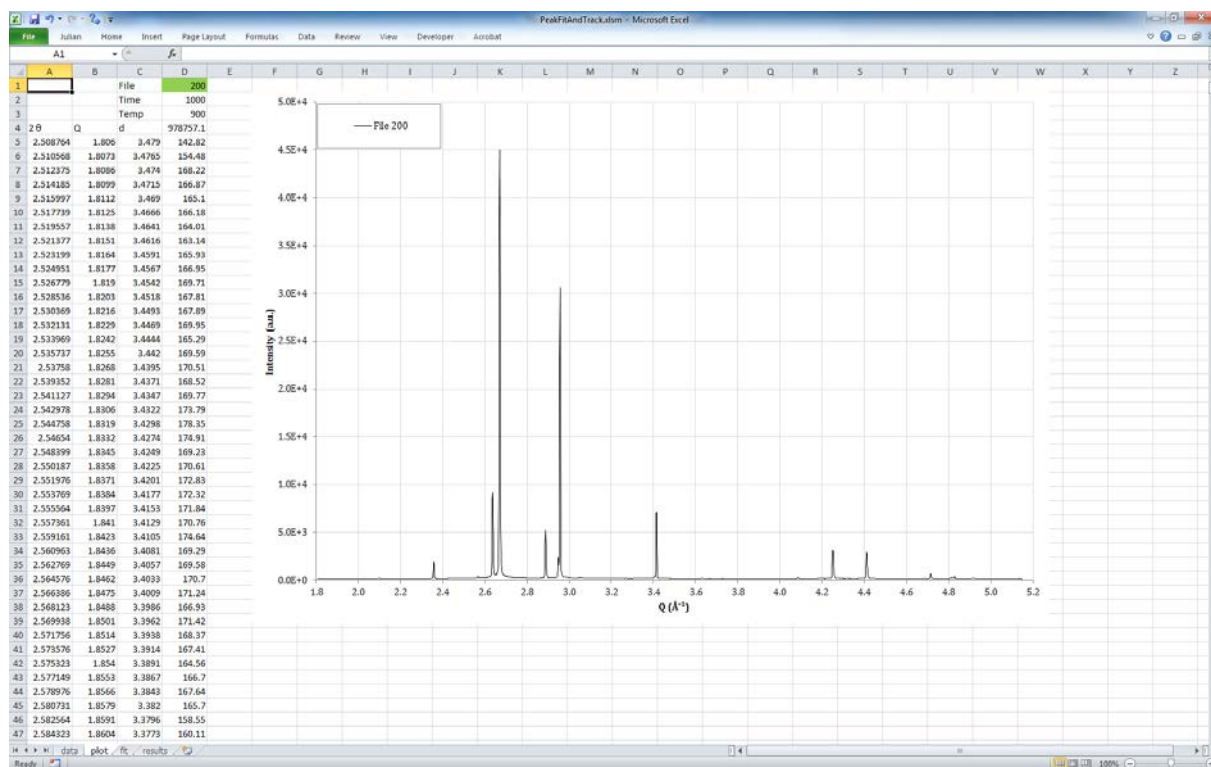


Figure 14 | Screenshot of the XRD-plot preview sheet in “PeakFitAndTrack.xlsm” tool.

Peak fitting and tracking

The actual fit is done on a separate sheet that is divided into three parts (see Figure 15). On the left the settings and the results are visible. The centre presents the current fit as a plot. The calculation of the curves is on the right but not entirely visible in this screenshot.

The “settings” area, where all frequently changeable cells are highlighted green, is divided into further topics. In the “General” part, an initial file for the static fit has to be set, as well as the margins left and right of the peak centre to specify the raw data to be included in the fit. The “Peak settings” contain cells to set the peak position Q for “peak A” and “peak B” separately, the Gaussian or Lorentzian weighting η of the pseudo-Voigt function, the width ω of the distribution, a scale factor Y and the Miller Indices h , k and l . Up to here, a first initial fit has to be done visually by changing the values manually. The “Peak results” part then presents the calculated d -spacing, lattice parameter, peak area and FWHM in real-time. The profile R-factor R_P shows the per cent accuracy of the fit. The labels for the plot are pre-set in the sector below to show wide-ranging information in the plot with values linked to the results. The “Automatic fitting” settings

consist only of a single cell with the number of the target file where the automatic fitting should end.

Upon pressing the “Start fitting” button, the program based on Visual Basic code gets launched. The entire code is shown in the appendix of this thesis. After the user has selected the desired peak, the program starts with the peak fit using the Excel Solver plug-in by modifying Q , η , ω and Y within the given constraints for each peak. When the fit is completed, the program automatically selects the next diffractogram and fits the selected peak again. After each single fit during the automatic routine, the input settings, results and the plot is updated so that the user can monitor the progress and quality. If a single peak fit is desired, the intensity of A or B has simply to be set to “0”. With the single peak settings, the fitting routine will not affect any settings of the second peak and the results are solely dependent on the first peak (no matter if A or B).

The calculation of the fit is done with functions contained in the faded cells on the right side (e.g. pseudo-Voigt, linear background interpolation and profile R-factor). The presentation of the values might be useful for debugging in case of unsatisfying fit results. The fitting function is evaluated for every Q value present in the input data, then additionally for 1000 data points per curve to facilitate visual evaluation of the fitting results by interpolation. None of the data or curves is smoothed.

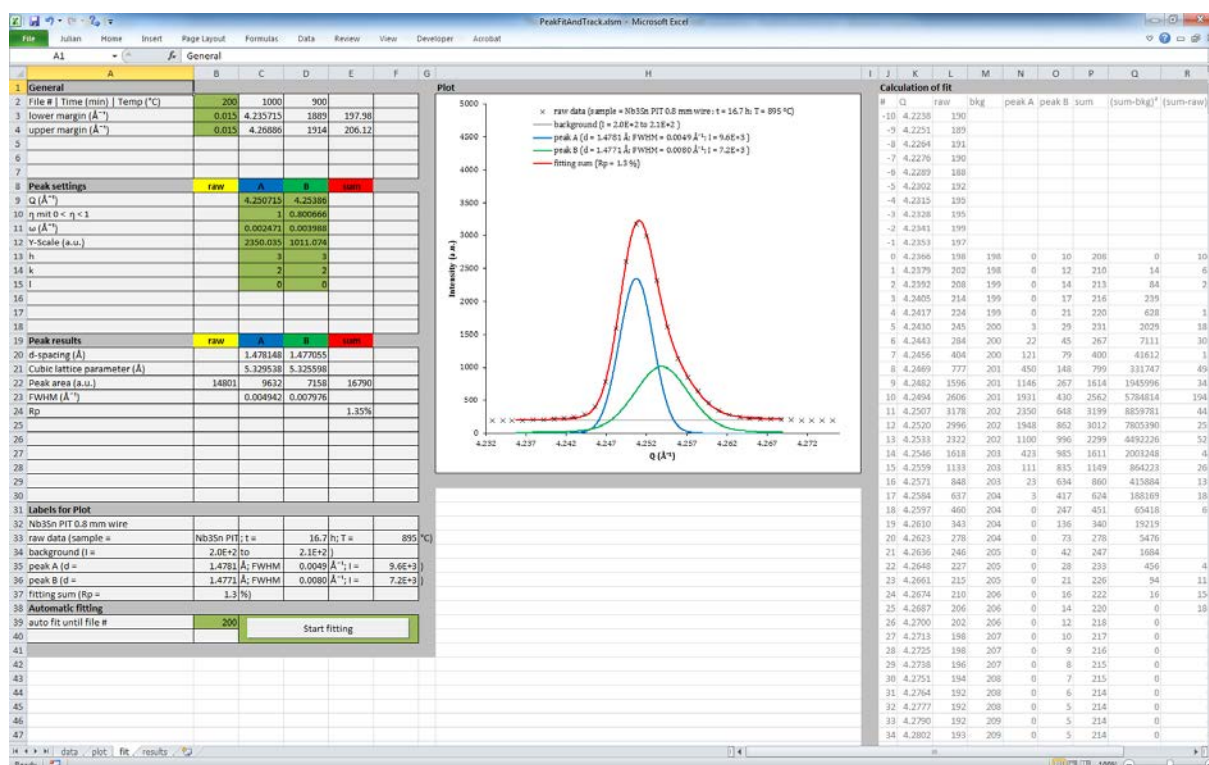


Figure 15 | Screenshot of the settings and fit execution sheet in “PeakFitAndTrack.xlsx” tool.

Summary of peak evolution

The results of the fits are summarised on the “results” sheet. On the left, three plots present the evolution of lattice parameter, intensity and FWHM for both peaks as a function of HT duration.

The appropriate temperature curve is shown as well on the secondary axis. Each column on the right represents the previously calculated fitting parameters for a single file (e.g. column “E” for file “1”, “F” for file “2”, ..., column “ZZ” for file “699”). If a new fit with changed constraints is desired, as might be necessary with data with a low signal-to-noise ratio, the automatic fitting routine can simply be rerun and the appropriate columns will get updated. By keeping the “old” data in the other columns, the different settings become comparable.

The arrangement of rows and columns is optimised to allow copying and pasting it into other Excel sheets, where the data can be summarised and compared to other data, for example for multiple peak reflections of a single phase.

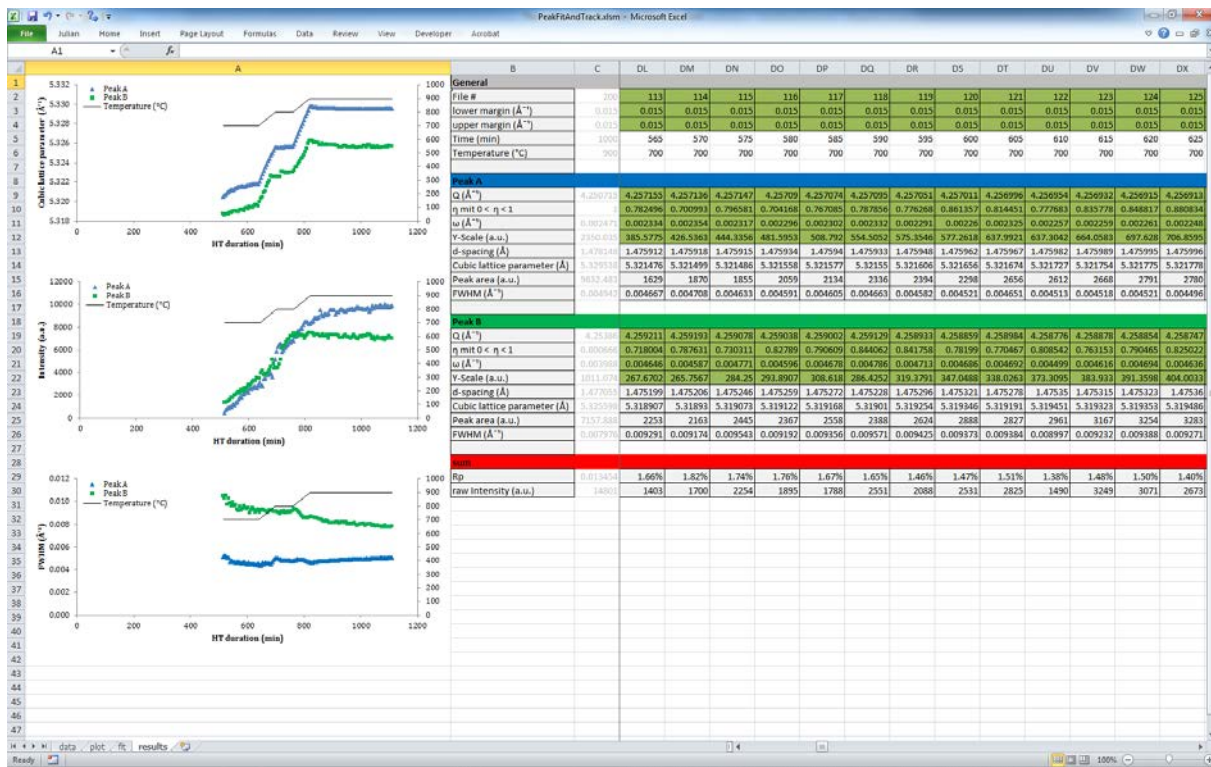


Figure 16 | Screenshot of the results sheet in “PeakFitAndTrack.xlsxm” tool.

2.4. X-ray absorption tomography

A sample analysis with three dimensional spatial resolution can be obtained with computed tomography. A tomogram is a reconstruction made of many hundred radiographs, which are acquired from different projection angles while the sample rotates. In this thesis the μm scale synchrotron X-ray absorption computer tomography ($\mu\text{-CT}$) [28] will be utilised.

Depending on the attenuation coefficients μ/ρ of the elements in the sample and the X-ray energy E a certain fraction of the photons is absorbed. The attenuation coefficients of the elements present in Bi-2212/Ag wires are shown in Figure 17 as a function of photon energy.

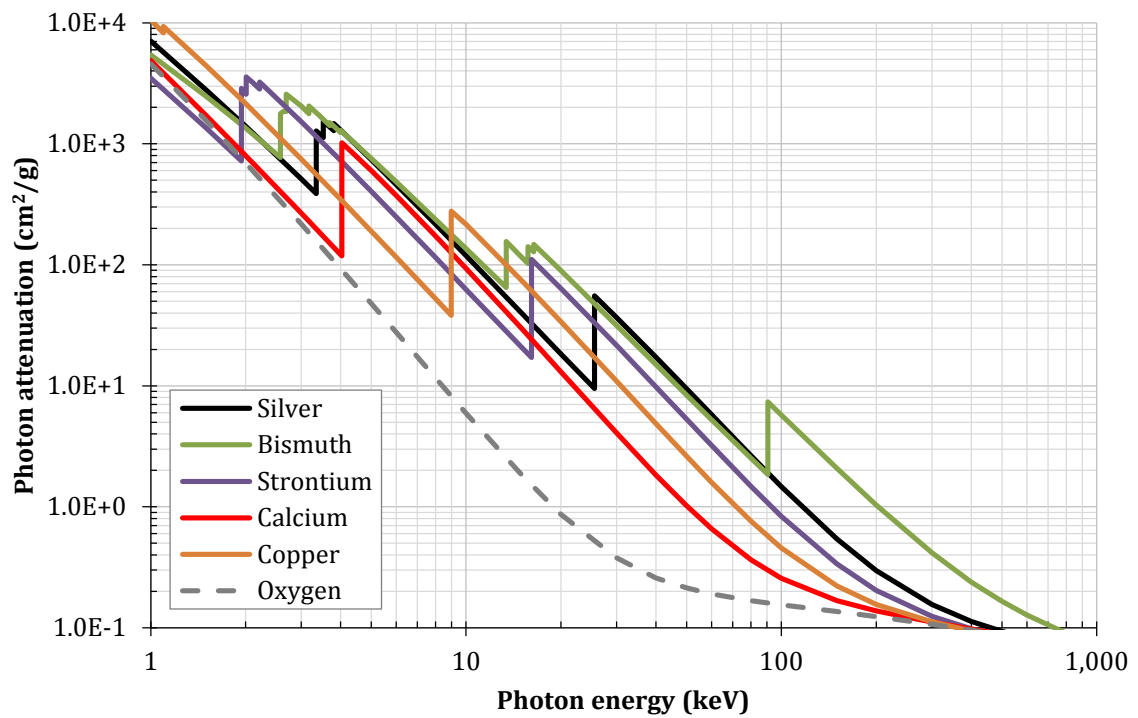


Figure 17 | Photon attenuation as a function of photon energy for Silver, Bismuth, Strontium, Calcium, Copper and Oxygen.

In the synchrotron tomography the transmitted part of the photon beam is transformed by a scintillator into visible light, which can be magnified, and recorded by a CCD image sensor. For magnification, standard visible light optics can be used. Figure 18 presents a schematic configuration of X-ray photon beam, sample, scintillator, magnification optics and image sensor.

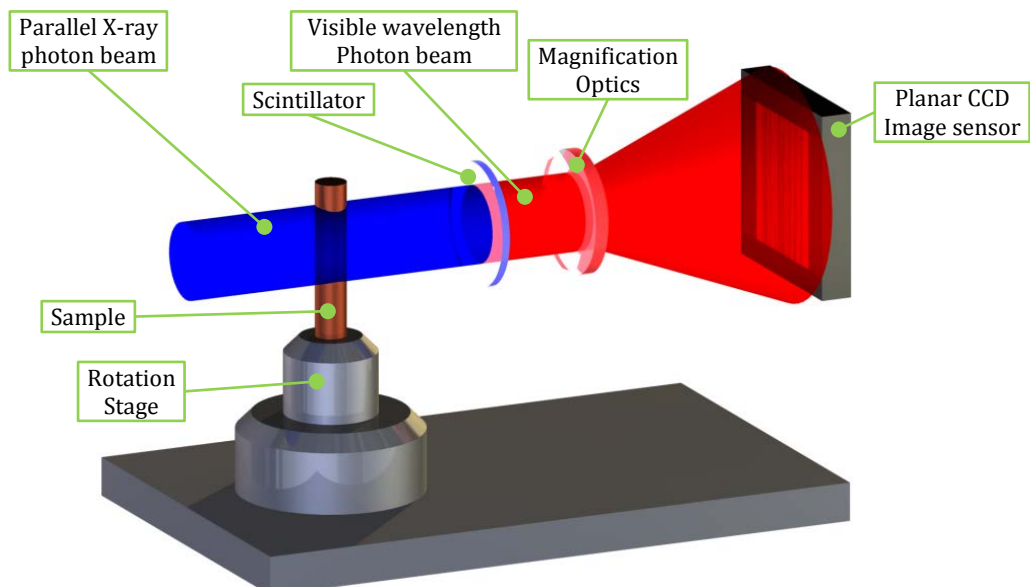


Figure 18 | Schematic configuration of the X-ray tomographic experiments.

With a single radiograph, only a 2D image is recorded. Each pixel is a grayscale representation of the total attenuation experienced by the parallel beam rays crossing the sample. For a 3D image,

a large series of radiographs have to be recorded at different angles. The radiographs are then reconstructed by software to achieve 3D tomography [29].

For high quality tomographic images, several guidelines have to be respected:

- The X-ray energy has to be high enough to enable sufficient transmission through the sample (see Figure 17).
- The rotation axis has to be accurate and angular rotation steps need to be synchronised in time with detector movement to be able to reconstruct the entire tomogram from the single radiographs.
- A “dark field” image (without X-ray beam) has to be recorded before each tomogram to allow subtraction of the detector noise caused for example by defect or burnt-in pixels.
- A “white field” image (with X-ray beam but without sample) has to be recorded before each tomogram to allow eliminating variation in photon intensity caused by a non-homogeneous beam.

With developed reconstruction and filtering software, most remaining artefacts can be eliminated but well-adjusted instruments remain a key element in image quality.

3. Description of the Bi-2212 and Nb₃Sn experiments

3.1. Samples

The different samples that have been studied are described below.

3.1.1. LaB₆ reference powder

Lanthanum hexaboride is a standard reference powder with a body-centred cubic unit cell [30] delivered by the National Institute of Standards and Technology (NIST). According to the certificate SRM 660b, LaB₆ has a lattice parameter of $a = 0.415\,688\,46(25)$ nm [31].

Using the LaB₆ reference powder for calibration purposes in the experiments gives a good knowledge of the functionality of the instrument (i.e. the diffraction peak broadening caused by the experiment). Sample to detector distance and X-ray energy can be determined iteratively.

3.1.2. Bi-2212 granulate precursor

The Bi-2212 precursor produced by Nexans, which is used for the fabrication of the PIT Bi-2212/Ag wires, has been used as a reference material [9] [32]. Bi-2212 powder has randomly distributed crystal orientations and is in a nearly stress-free state. The diffraction pattern is expected to show peaks without asymmetry or shift and with intensity ratios corresponding to a texture-free material.

A tomographic cross section of the granulate particles is shown in Figure 19. The Bi-2212 particle size is up to 0.2 mm. The space between the particles is filled by air. When the particles are filled into the silver tubes and the compound is drawn to filament size, the particle size decreases further by breaking.

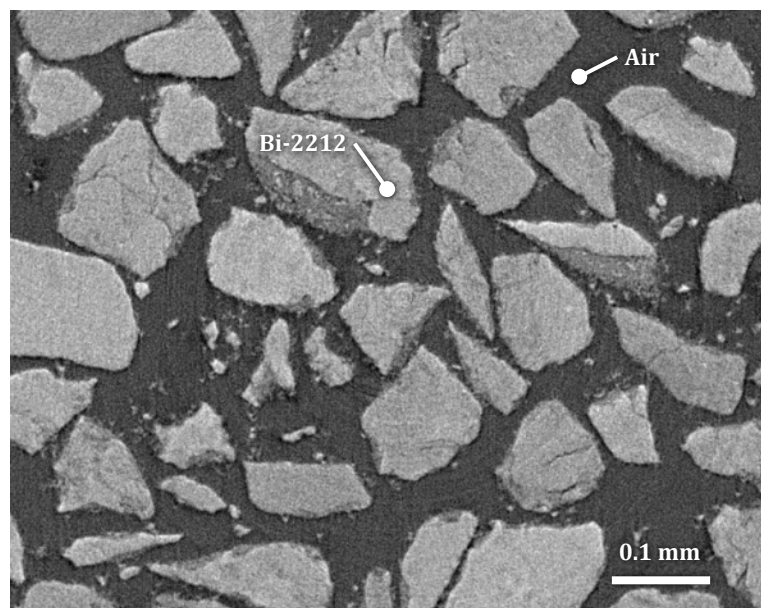


Figure 19 | Tomographic cross section of Bi-2212 powder particles held in a glass capillary.

3.1.3. Bi-2212/Ag single core wire

Prior to the fully stacked multi-filament wires, a hexagonal single core wire with 2.4 mm face to face size is produced, bundles of which are then restacked as parallel filaments in a Ag-Mg tube with 0.2 wt.% Mg. For the experiments presented here, this wire was drawn into a circular cross section with 1 mm outer diameter and 0.6 mm core diameter. This sample was produced by Oxford Instruments Superconducting Technology.

3.1.4. Bi-2212/Ag multifilament wire

Bi-2212/Ag composite wires are the principal samples studied here. A transverse tomographic cross section of the multifilament wire is presented in Figure 3. The Bi-2212/Ag wire has been produced by Oxford Instruments Superconducting Technology using the PIT process. The matrix consists of pure Ag and the outer sheath is Ag with 0.2 wt.% Mg [7]. Bi-2212 and its residual porosity takes about 25-30 vol.% of the as-drawn, so-called green state wire [33]. The wire has a diameter of $\varnothing = 0.8$ mm and was cut into about 5 cm long pieces.

3.1.5. Nb₃Sn/Cu multifilament wire

Three different Nb₃Sn samples were studied here. The RRP wire [8] is produced by Oxford Instruments Superconducting Technology (OIST) and has a diameter of $\varnothing = 0.8$ mm with 54 sub elements each containing Nb rods and surrounded by diffusion barriers [34]. The PIT wires [35] were produced by Shape Metal Innovation (now BAS) with an original diameter of 1.25 mm. The $\varnothing = 1.25$ mm PIT wire was drawn down to $\varnothing = 0.8$ mm diameter. This reduced filament size from about 50 μm to about 33 μm , and allowed a similar absorption of X-rays resulting in XRD patterns of both wire types more suitable for comparison using identical experimental settings.

3.2. Applied heat treatments

Bi-2212 experiments

The heat treatments that were applied to the Bi-2212/Ag samples in this thesis are based on the experiments of Shen et al. [36] to reach high J_c , but have been modified to analyse individual influences. For *in situ* heat treatment (HT), the cool-down rate is raised and the isothermal period is shortened to allow the execution of more experiments during the available beam time. The temperature, measured by type S thermocouples spot welded to the samples, is regulated by an electronic furnace system. A temperature accuracy of ± 2 °C could be maintained. The pressure of the 100 bar air HT was kept within ± 2 bar deviation.

Table 2 | Heat-up and cool-down rates during the heat treatments performed on the Bi-2212/Ag samples.

	Bi-2212/Ag wire 1 bar air high-res XRD (Chapter 4.5)	Bi-2212/Ag wire 1 bar air / inert gas low-res XRD (Chapter 4.6)	Bi-2212/Ag wire 100 bar air low-res XRD (Chapter 4.7)	Bi-2212/Ag single core 1 bar air low-res XRD + μ -CT (Chapter 4.8)	Bi-2212/Ag wire 1 bar oxygen <i>ex situ</i> NHMFL-ASC (Chapter 4.4 and 4.3)
1st heat-up (1/2)	200 °C/h to 840 °C	160 °C/h to 825 °C	160 °C/h to 825 °C	200 °C/h to 825 °C	160 °C/h to 820 °C
isothermal	-	1 h	-	0.5 h	2 h
1st heat-up (2/2)	25 °C/h to 890 °C	50 °C/h to 900 °C	50 °C/h to 900 °C	25 °C/h to 890 °C	50 °C/h to 890 °C
isothermal	-	0.2 h	0.2 h	1 h	0.2 h
cool-down (1/3)	-25 °C/h to 830 °C	-25 °C/h to 830 °C	-25 °C/h to 830 °C	-25 °C/h to 830 °C	-10 °C/h to 880 °C
isothermal	-	-	2 h	-	-
cool-down (2/3)	-	-	-200 °C/h to RT	-200 °C/h to RT	-2.5 °C/h to 832 °C
isothermal	-	-	-	-	48 h
cool-down (3/3)	-	-	-	-	-200 °C/h to RT
isothermal	-	-	-	-	-
2nd heat-up (1/1)	160 °C/h to 965 °C	160 °C/h to 965 °C	-	-	-

Nb₃Sn experiments

The three Nb₃Sn *in situ* experiments were performed with identical HTs in inert gas. The heat cycle initially heats up (heating rate 100 °C/h) to 700 °C and stays at this temperature for 4 hours. Two further heat-ups to 800 and 900 °C follow subsequently, each lasting 1 hour. During the isothermal periods, the evolution Nb₃Sn, Nb, Sn and Cu can be observed without heating rate influence. The temperature was regulated by a thermocouple that measures the furnace temperature. The estimated sample temperature accuracy is ± 5 °C.

3.3. Beam line setup at ESRF ID15

The experiments have been performed at the high energy scattering beam line ID15 of the ESRF (ID15A for XRD and μ -CT studies and ID15B for XRD studies) [37]. A photograph of the ID15A beam line set-up taken during the single core Bi-2212/Ag wire experiment of beam time MA-

1475, showing the sample on the rotation stage, the XRD flat panel detector and the μ -CT camera, is shown in Figure 20.

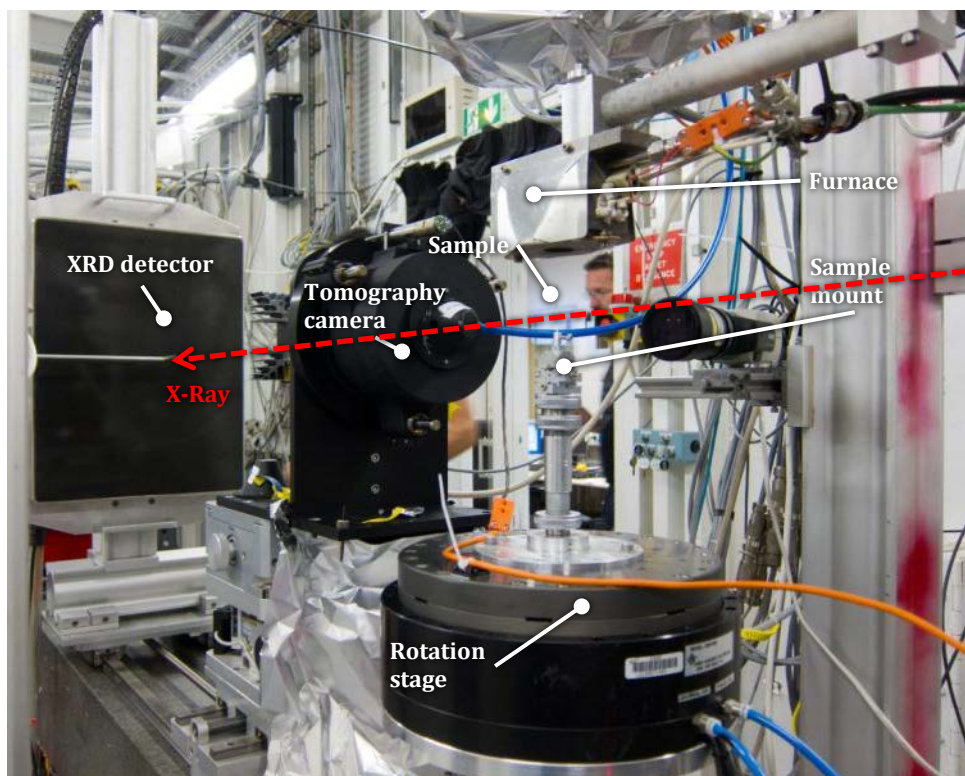


Figure 20 | Test environment in ID15A with rotating table, furnace, XRD detector and tomography camera.

ID15A is a flexibly configurable beam line designed for fast high energy X-ray scattering and imaging experiments. The synchrotron beam energy can be varied in the range of 30 to 500 keV. The photon beam size can be adjusted from $20 \times 5 \mu\text{m}^2$ to $1.2 \times 1.2 \text{mm}^2$. The relatively small scattering angles of high energy photons make it easier to add auxiliary equipment like a furnace to the experiment, and at the same time record a wide d-spacing range. ID15B has additional equipment for high pressure sample environments, but is limited to fixed energies of 30, 60 or 90 keV, and offers no possibilities for tomography. The HTs that are described in Chapter 3.2 were applied with dedicated furnaces. The furnace for atmospheric pressure experiments is equipped with thin aluminium windows that are nearly X-ray transparent.

For high pressure XRD experiments, single crystal sapphire capillary was used. To avoid an overexposure of the detector, the areas on the detector where the sapphire diffraction spots appear were covered with lead pieces to absorb the photons (see Figure 21). Thus, some diffraction peaks of the actual sample have not been recorded at their entire intensity.

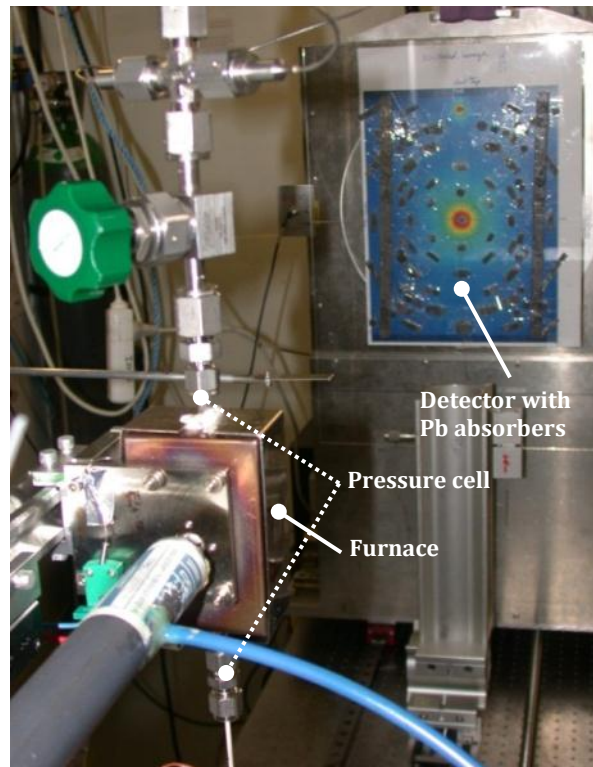


Figure 21 | Test environment in ID15B with furnace, pressure cell and detector. Courtesy J. Andrieux.

The same flat rectangular detector was used to record X-ray diffraction patterns in all experiments. The “Triaxell Pixium 4700” is a photosensitive detector with a pixel pitch of 154 μm and a sensitive area of 381.9 x 294.1 mm. The A/D conversion dynamic range is 14 bit. All Bi-2212 experiments described here were done with approximately 1 m sample to detector distance. The Nb₃Sn high resolution diffraction experiments were performed with \sim 5 m sample to detector distance.

For tomographic recordings a 15 μm thick LuAG:Ce²⁺ scintillator was used to convert the X-ray photon beam into visible light. After 10x optical magnification, the tomograms were recorded with a high speed CCD camera (DALSTAR Pantera 1M60).

For both XRD and μ -CT experiments, the sample was mounted vertically on a high precision rotation stage. For μ -CT measurements, a rotating sample is essential to record a series of radiographs at different projection angles. To record XRD patterns, the rotation of the sample is beneficial to capture diffraction spots from a higher number of crystallites. With the sample being (almost) rotationally symmetrical, no relevant information is lost for XRD measurements during rotation.

ID15A is equipped with a setup to perform combined XRD and μ -CT measurements. A computer controlled translation stage can move the μ -CT detector in or out of the photon beam to switch between μ -CT or XRD measurements. A schematic view of the combined XRD and μ -CT experiment configuration is presented Figure 22. Exclusive XRD configuration is identical but without the tomographic camera.

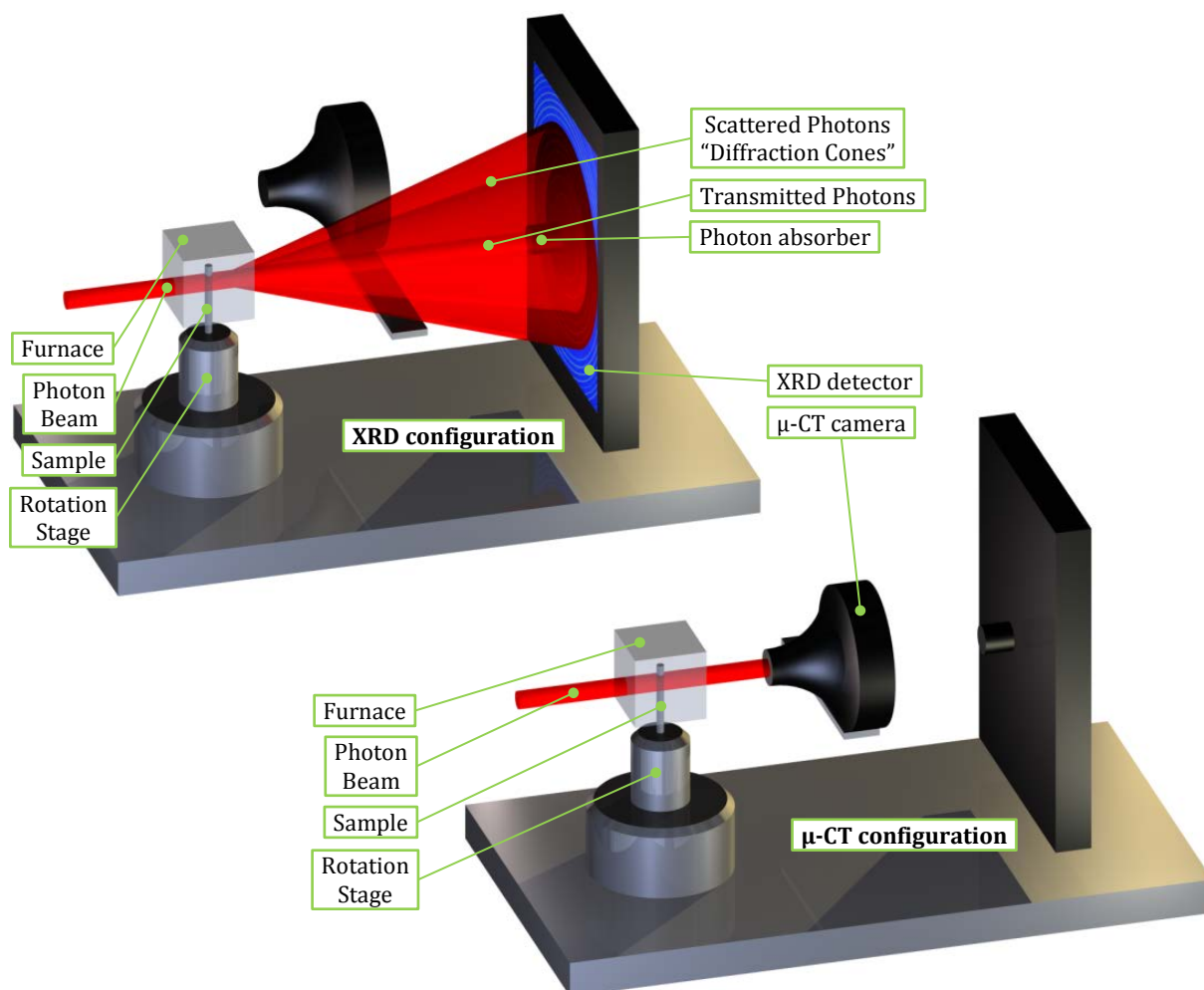


Figure 22 | Experimental set-up for combined *in situ* XRD and μ -CT experiments at ESRF ID15A.

The experimental settings are summed up in Table 3, together with the samples that were studied, the applied process gas, X-ray energy, X-ray bandwidth, μ -CT resolution and XRD instrument-induced broadening. During all *in situ* experiments described here, tomograms and diffractograms were acquired every 5 minutes.

Table 3 | Experimental settings for Bi-2212 and Nb₃Sn experiments.

Sample	Heat treatment	X-ray energy (bandwidth) (keV (eV))	μ -CT resolution (μm)	XRD FWHM (\AA^{-1})
Bi-2212 granulate	-	69 (90)	2	0.010 – 0.011
Bi-2212/Ag wire	-	69 (90)	2	0.010 – 0.011
Bi-2212/Ag wire	<i>ex situ</i> 1 bar O ₂ (888 °C quenched)	69 (90)	-	0.010 – 0.011
Bi-2212/Ag wire	<i>ex situ</i> 1 bar O ₂	69 (90)	-	0.010 – 0.011
Bi-2212/Ag wire	<i>in situ</i> 1 bar air	69 (90)	-	0.010 – 0.011
Bi-2212/Ag wire	<i>in situ</i> 1 bar air	69 (800)	-	0.026 – 0.040
Bi-2212/Ag wire	<i>in situ</i> 1 bar inert gas	69 (800)	-	0.026 – 0.040
Bi-2212/Ag wire	<i>in situ</i> 100 bar air	90 (800)	-	0.026 – 0.028
Bi-2212/Ag single core	<i>in situ</i> 1 bar air	87 (800)	2	0.028 – 0.040
Nb ₃ Sn $\varnothing = 0.8$ mm RRP	<i>in situ</i> 1 bar air	81 (25)	-	0.0034 – 0.0041
Nb ₃ Sn $\varnothing = 0.8$ mm PIT	<i>in situ</i> 1 bar air	81 (25)	-	0.0034 – 0.0041
Nb ₃ Sn $\varnothing = 1.25$ mm PIT	<i>in situ</i> 1 bar air	81 (25)	-	0.0034 – 0.0041

LaB₆ reference powder to characterise instrumental function

The instrument-induced peak broadening was determined using LaB₆ reference powder. The Debye Scherrer diffraction pattern as recorded with the Triaxcel Pixium 4700 detector is shown in Figure 9 in Chapter 2.2. The homogeneous concentric rings show the good random orientation of the LaB₆ crystallites in the powder. An absence of background intensity in the centre spot and a lowered intensity towards the bottom edge of the detector are caused by a photon absorber and its mount.

To determine a proper fitting function, a comparison between the Gaussian and Lorentzian fits was done for several peaks. As an example, Figure 23 illustrates the difference between the two fits. In the subsequent analyses, care has been taken to ensure the consistent use of fitting functions.

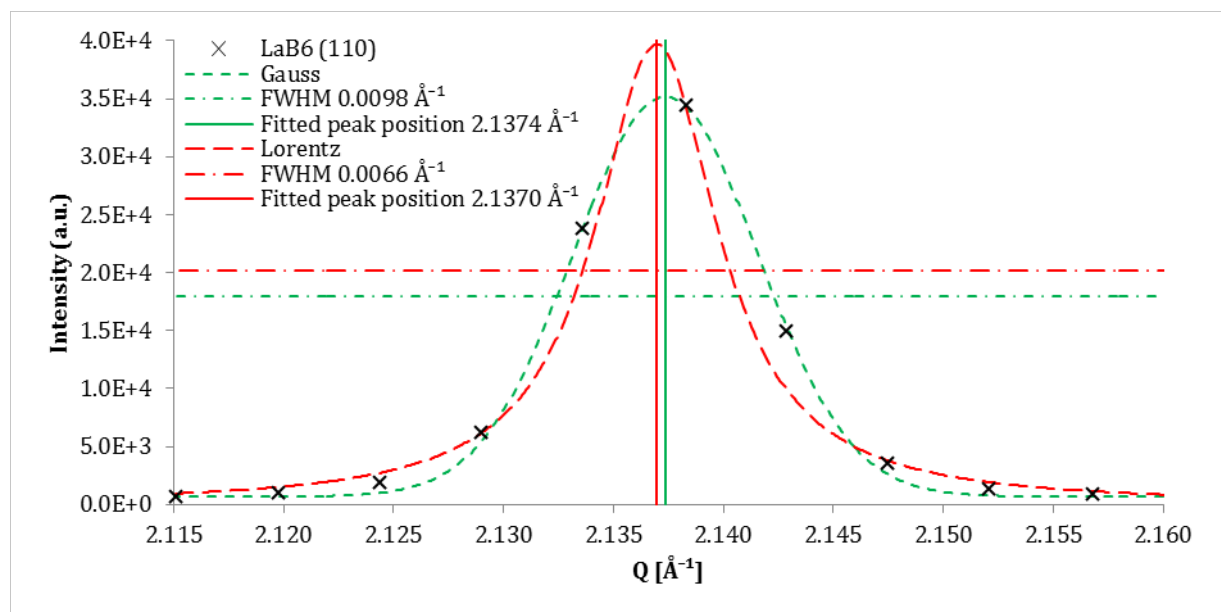


Figure 23 | Gaussian and Lorentzian functions compared in fitting accuracy to the peak LaB₆ (110) of the reference powder at RT.

A comparison of the different values measured for the Bi-2212 experiment with 69 keV energy and medium bandwidth are presented in Table 4 with the reference provided by NIST [31]. The peak positions show a maximum deviation of $d = 0.001 \text{ \AA}$. This accuracy is entirely sufficient for the further analysis.

Table 4 | Comparison of measured (Gaussian peak fitting) and reference [31] LaB₆ diffraction peak positions and intensities.

			Measured	Reference
h	k	l	d-spacing (Å)	d-spacing (Å)
1	0	0	4.157	4.1569
1	1	0	2.940	2.9394
1	1	1	2.400	2.4000
2	0	0	2.079	2.0784
2	1	0	1.859	1.8590
2	1	1	1.697	1.6970
2	2	0	1.470	1.4697

As presented for the Gauss fitted peaks of LaB₆ later in Figure 31, the FWHM is distributed in a range of $Q = 0.0097$ to 0.0107 \AA^{-1} , increasing slightly as a function of Q . The measured FWHM can be assumed to be the instrument-induced peak broadening of the experiment.

4. Analysis of XRD and μ -CT results acquired during the processing of Bi-2212/Ag wires

Several experiments have been performed in order to see the influence of O_2 partial pressure on the evolution of Bi-2212 and further phases as a function of HT duration and temperature. *In situ* XRD and μ -CT analysis has been done with multiple samples during HTs using 1 bar inert gas, 1 bar air and 100 bar air process gas. The Bi-2212 precursor granulate and the *ex situ* processed wires have been analysed as reference samples. XRD measurements have been done to monitor the evolution of phase formation, volume and stability with potential information on crystallite size and texture. μ -CT has been used mainly to monitor void growth and 2nd phase formation.

4.1. Diffraction pattern of Bi-2212 granulate

The precursor Bi-2212 granulate from Nexans that is used to produce the Bi-2212/Ag wires has been characterised as a reference material for the subsequent XRD analysis of Bi-2212/Ag wires. For diffraction measurements the precursor granulate is held in a glass capillary. The 2D pattern of the granulate as it is recorded with the Trixell Pixium 4700 detector is presented in Figure 24. As expected the homogeneous circular intensity distribution of the diffraction rings indicates a random orientation of the Bi-2212 crystallites. The main diffraction rings that will be analysed later are labelled with Miller Indices.

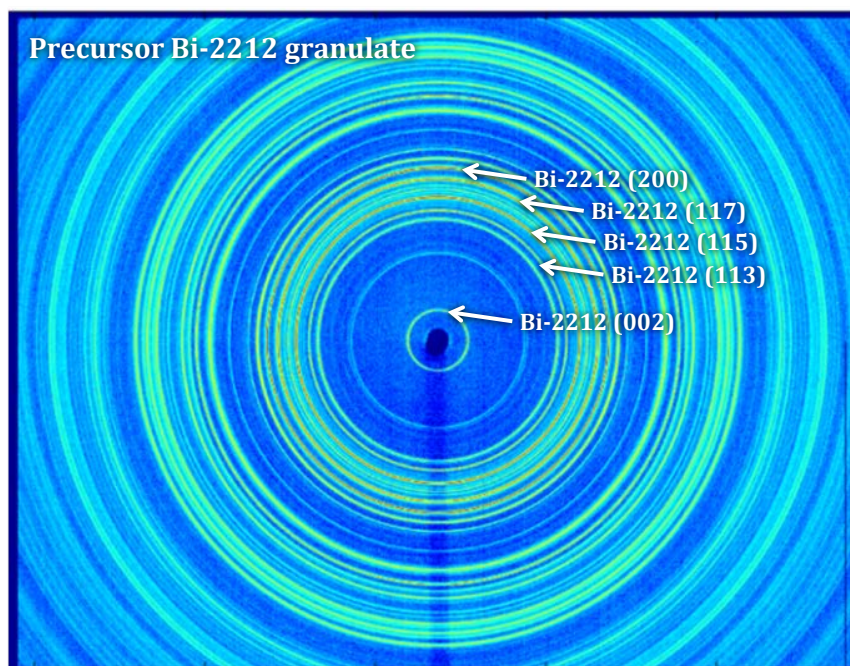


Figure 24 | Diffraction pattern of precursor Bi-2212 granulate held in a glass capillary as recorded with the Trixell Pixium 4700 detector. (Granulate provided by M. Rikel, Nexans)

The circularly integrated diffraction pattern of the Bi-2212 pre-cursor granulate is shown in Figure 25. A good signal to noise ratio and sufficient angular resolution allows an identification of most peaks. But several are superimposed by others and can only be analysed with limits. The most intense and almost free of superposition Bi-2212 (002), (113), (115), (117) and (200)

peaks will be analysed in detail. The peaks indicated with +1 or -1 are modulated peaks according to Matheis et al. [13].

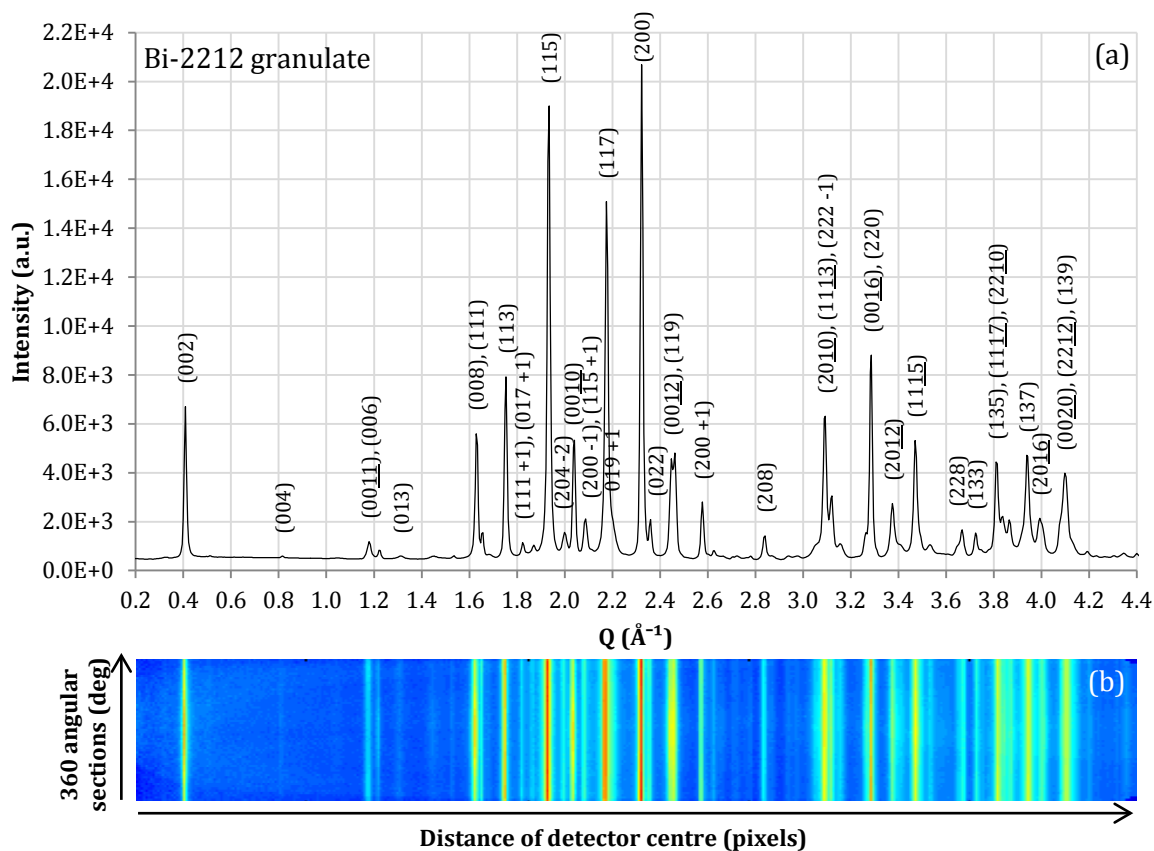


Figure 25 | (a) Circularly integrated diffraction pattern of Bi-2212 granulate held in a glass capillary at RT. (b) Sectorised data as recorded with the Triaxcel Pixium 4700 detector.

Prior to peak position and peak shape analysis the individual diffraction peaks were fitted with Lorentzian functions, which in the case of the Bi-2212 granulate show a better correlation to the measured data than the Gaussian function. In contrast to the Gaussian broadening visible in LaB₆ that is caused by the beam wavelength distribution around its nominal value, the diffraction peaks in this sample can be fitted with higher accuracy taking the Lorentzian function. This could be an indication for multiple crystallite sizes within the Bi-2212 phase (as explained in Chapter 2.2). Figure 26 illustrates an exemplary fit of the Bi-2212 (115) peak with both functions.

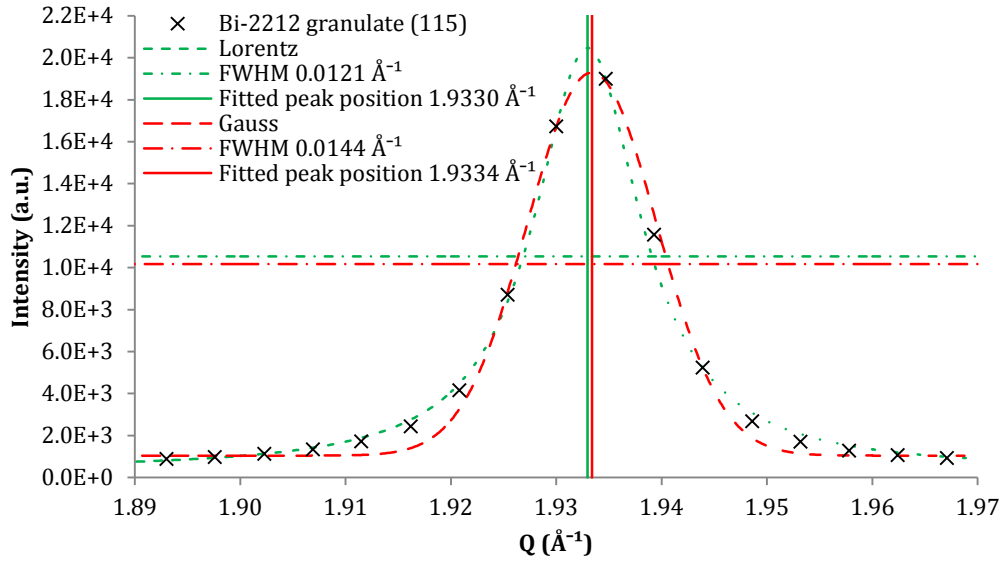


Figure 26 | Bi-2212 (115) diffraction peak of Bi-2212 granulate fitted with Gaussian and Lorentzian functions.

A comparison between the detected peak positions and the values reported by Matheis and Snyder [13] is presented in Table 5. The measured and reported peak positions have a maximum difference of 0.2 %. The relatively small deviation of the peak intensity ratios may be partly explained by peak superposition and uncertainties in the background subtraction.

Table 5 | Comparison of measured (Lorentzian peak fitting) and reference Bi-2212 peak positions and intensities.

			Bi-2212 phase in Bi-2212 granulate (measured at ID15A)			Reported by Matheis and Snyder [13]	
h	k	l	Q (Å ⁻¹)	d-spacing (Å)	Intensity (a.u.)	d-spacing (Å)	Intensity (a.u.)
0	0	2	0.408	15.38	26	15.395	8
0	0	4	0.816	7.703	1	-	-
0	0	6	1.223	5.139	2	5.1446	2
0	0	8	1.631	3.853	22	3.8571	29
1	1	3	1.753	3.585	33	3.5845	34
1	1	5	1.933	3.251	100	3.2506	94
0	0	10	2.039	3.081	19	3.0868	30
1	1	7	2.176	2.887	86	2.8881	66
2	0	0	2.324	2.704	83	2.7031	100
2	0	8	2.839	2.213	5	2.2140	5
2	2	0	3.285	1.913	44	1.9117	40
1	1	15	3.472	1.810	28	1.8114	20
1	3	3	3.725	1.687	5	1.6857	4
1	3	5	3.813	1.648	19	1.6473	16
1	3	7	3.941	1.594	22	1.5936	15

4.2. XRD of “green” Bi-2212/Ag wire (before HT)

The starting material to be processed is the as-drawn Bi-2212/Ag wire that has been analysed in advance to have a reference for further *in situ* experiments. The Debye Scherrer diffraction pattern of the as-received and non-heat-treated Bi-2212/Ag wire (referred in the following as “green” Bi-2212/Ag wire) is shown in Figure 27. Non-random crystallite orientation (i.e.

texture) which is developed during the wire production process is the reason for the intensity inhomogeneity of the Ag diffraction rings. The Bi-2212 rings however are almost homogeneous. That means there is no strong texture of the Bi-2212 powder filaments after the wire draw process.

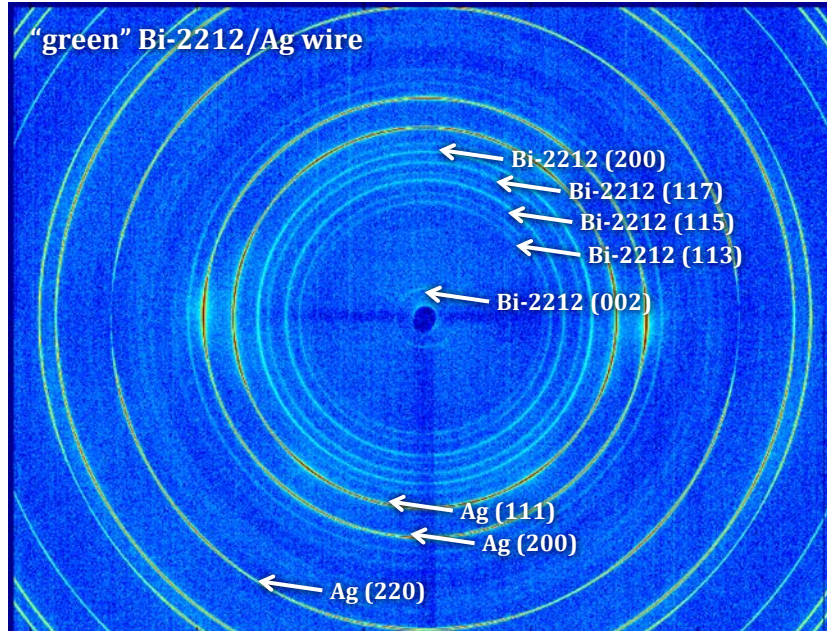


Figure 27 | Diffraction pattern of the $\varnothing = 0.8$ mm “green” Bi-2212/Ag wire as recorded with the Trixell Pixium 4700 detector. (Sample provided by NHMFL-ASC, Tallahassee)

Figure 28 shows the corresponding circular integrated diffraction pattern. The most intense Bi-2212 and Ag peaks are labelled with their Miller Indices. The Bi-2212 peaks in this pattern already show a significant broadening. This indicates the decreased crystallite size as a result of the breaking and/or non-homogeneous stress distribution. Many peaks cannot be identified singularly because of the resulting peak overlaps.

Beside the Ag and Bi-2212 peaks, three further peaks are observed. The width of these peaks is about half of the instrumental peak broadening (as determined from the Ag and LaB_6 peak width). Therefore, it is assumed that these reflections (labelled with “*”) are not from the sample, but from another material that was accidentally in the beam between sample and detector.

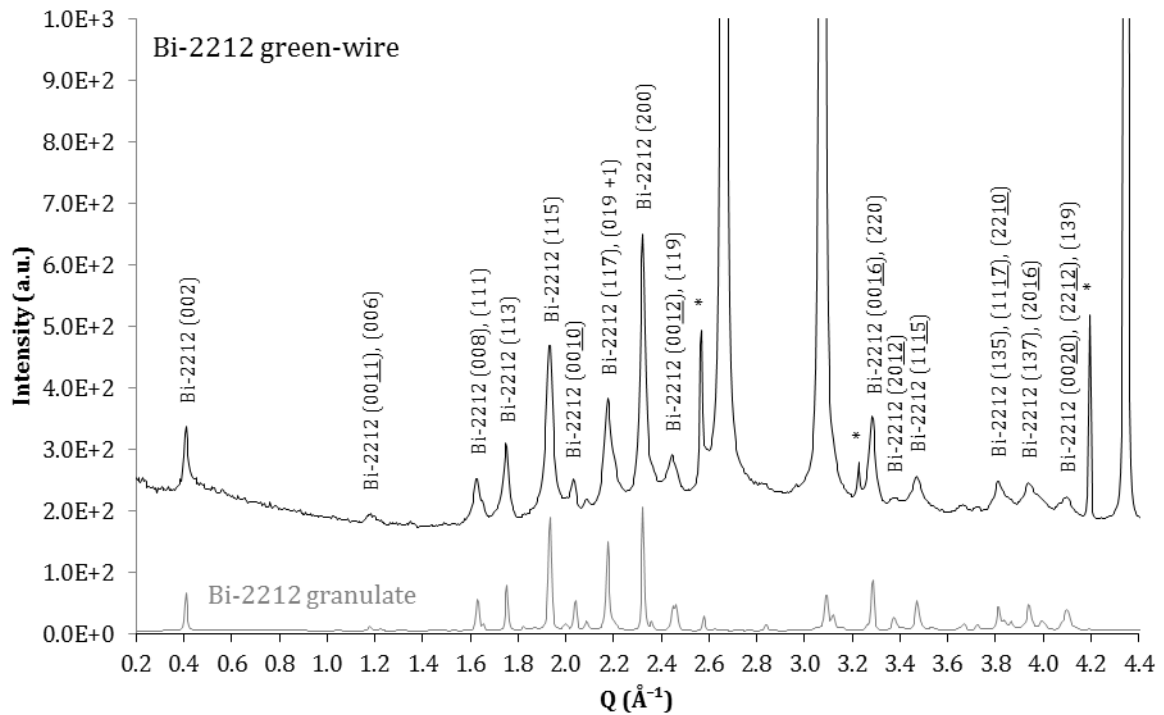


Figure 28 | XRD pattern of the “green” Bi-2212/Ag wire with the identified Bi-2212 and clipped Ag peaks.

4.3. XRD of *ex situ* processed Bi-2212/Ag wire in 1 bar O₂

The processing of Bi-2212/Ag wire is typically performed in pure oxygen and the process lasts several days [12]. Since *in situ* process in pure oxygen was not possible and the process duration needed to be shortened for the available beam time at ESRF, an *ex situ* processed wire sample has been analysed. The XRD pattern of the fully processed Bi-2212/Ag wire after the standard processing in 1 bar O₂ is shown in Figure 29. Intensity inhomogeneities of the Ag diffraction rings are observed as very similar as in the “green” wire. The maximal temperature during the heat cycle remained below the melting point of Ag and the Ag texture was preserved. However, by now the other diffraction rings show inhomogeneities, too. Thus the 1 bar O₂ HT changes the Bi-2212 crystallites orientation in the filaments.

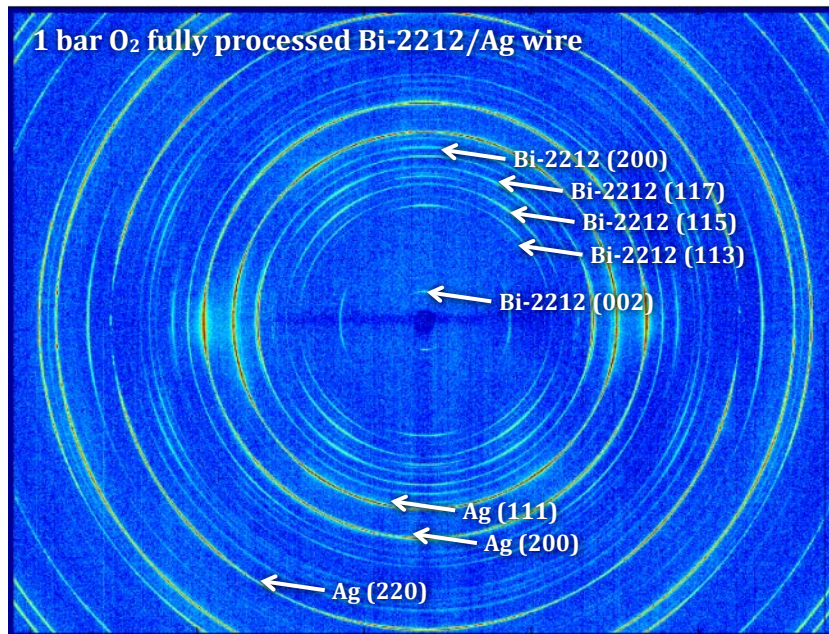


Figure 29 | XRD pattern of the 1 bar O₂ fully processed Bi-2212/Ag wire as recorded with the Trixell Pixium 4700 detector. (Sample provided by NHMFL-ASC, Tallahassee)

The corresponding circularly integrated diffraction pattern is shown in Figure 30. Compared to the “green” wire, the Bi-2212 phase shows significantly less peak broadening. This is most probably due to an increased crystallite size. The Bi-2212 phase is known to melt during the process where after new Bi-2212 crystallites can grow. Most of the Bi-2212 peaks can be identified as in the precursor Bi-2212 granulate. Bi-2201 could not be identified in this XRD pattern.

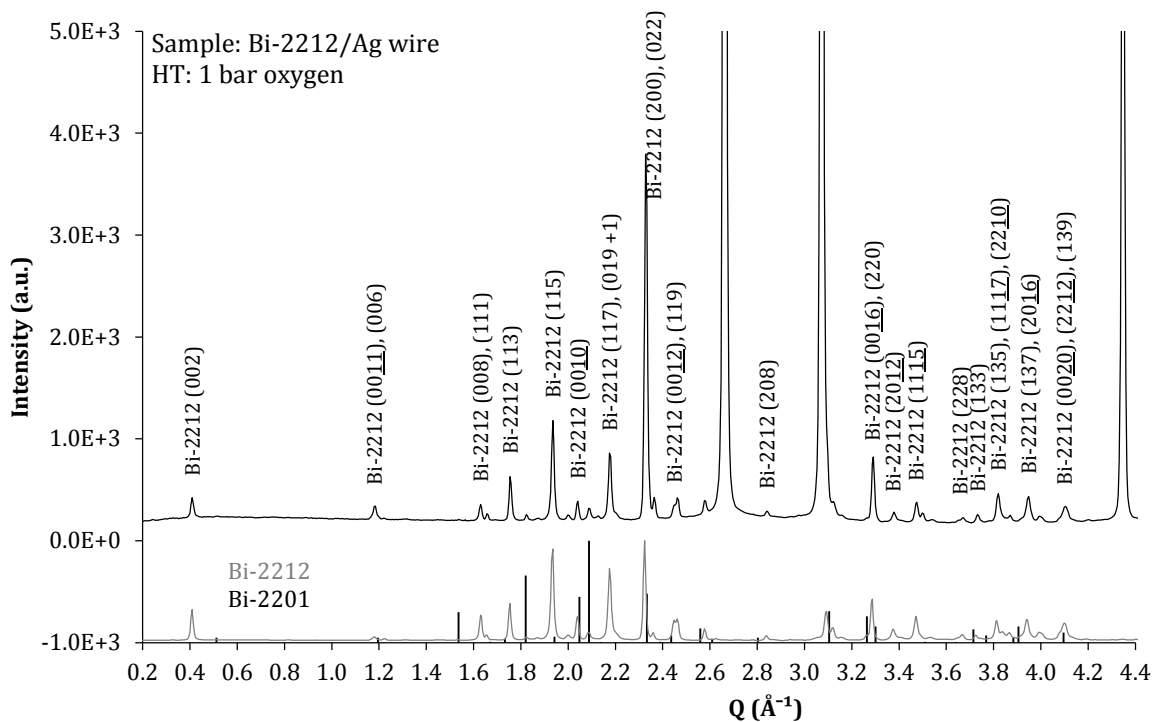


Figure 30 | XRD pattern of the 1 bar O₂ fully processed Bi-2212/Ag wire with the main Bi-2212 peaks identified and Ag peaks clipped.

In Table 6 the position and relative intensity of the main Bi-2212 peaks are compared for granulate, green wire and fully processed wire. Bi-2212 peaks superimposed by Ag peaks cannot be used for comparison. Due to highly broadened peak shapes, peaks close to each other cannot be differentiated clearly and influence the results by peak broadening, shift and asymmetry. All peak positions and integrated intensities have been determined after Lorentzian peak fitting. The peak positions of the Bi-2212 phase in the 1 bar O₂ processed wire sample deviate from the peak positions in precursor granulate not more than 0.3 %.

In the 1 bar O₂ processed wire the Bi-2212 (200) to (113) intensity ratio is four times bigger than observed in the precursor Bi-2212 granulate. Regarding the 2D pattern in Figure 29, the texture is visible at most of the other peaks as well but after 360° circular integration the information on texture disappears partially (see explanation in Chapter 2.2.). For detailed texture analysis a sectorised circular integration would be necessary.

Table 6 | Bi-2212 peak positions and intensities of the Bi-2212/Ag wire after 1 bar O₂ HT, a green Bi-2212/Ag wire and the Bi-2212 granulate. ("n.m." = "not measured" due to peak superposition or low intensity)

h	k	l	Bi-2212 granulate		Bi-2212 "green" wire		Bi-2212 wire after O ₂ HT	
			Q (Å ⁻¹)	Integrated intensity (a.u.)	Q (Å ⁻¹)	Integrated intensity (a.u.)	Q (Å ⁻¹)	Integrated intensity (a.u.)
0	0	2	0.408	26	0.409	17	0.410	5
0	0	8	1.631	22	1.626	n.m.	1.630	4
1	1	3	1.753	33	1.749	32	1.756	12
1	1	5	1.933	100	1.932	76	1.935	28
0	0	10	2.039	19	2.032	n.m.	2.040	3
1	1	7	2.176	86	2.176	n.m.	2.177	19
2	0	0	2.324	83	2.323	100	2.330	100
2	2	0	3.285	44	3.284	28	3.289	18
1	1	15	3.472	28	3.470	n.m.	3.474	6
1	3	3	3.725	5	n.m.	n.m.	3.733	3
1	3	5	3.813	19	3.814	n.m.	3.820	7
1	3	7	3.941	22	3.941	n.m.	3.947	4

Comparison of *ex situ* diffraction peak widths

Below, the diffraction peak widths acquired for the granulate, the "green" wire and the fully processed wire have been analysed in an attempt to extract information about crystallite size and/or strain effects (see Chapter 2.2)

The width (FWHM) of diffraction peaks in the different Bi-2212 samples described above is compared in Figure 31. The instrument induced broadening is estimated from the LaB₆ reference powder peak width. To show the reliability of peak broadening measurements in the "green" wire, the width of its Ag diffraction peaks is presented as well. It can be seen that the Ag peak widths have the same width as the LaB₆ reference powder peaks.

The Bi-2212 peaks of the precursor Bi-2212 granulate and 1 bar O₂ fully processed Bi-2212/Ag wire show an approximately 10 to 50 % increased width respecting to the instrument induced broadening. A comparatively strong variation in the peak width results is observed, which may

partly be explained by fitting uncertainties caused for instance by background subtraction uncertainties and peak superposition. Since the Bi-2212 peak widths of these samples are dominated by instrument induced broadening further analysis of the peak shapes has not been attempted.

The "green" Bi-2212/Ag wire sample shows a clear peak width increase above the instrument induced broadening (80 to 140 % increase of FWHM with respect to LaB₆ reference powder peaks) while the widths of the Ag peaks are clearly determined by instrument induced broadening. Possible reasons for the Bi-2212 peak broadening are a non-uniform strain distribution and the effect of small crystallite size. However the scatter in the FWHM result is too strong in order to clearly distinguish between size and strain effect according to the presented Scherrer formulas. Further semi-quantitative assessment would require a careful deconvolution of the instrument function, which has not been attempted here.

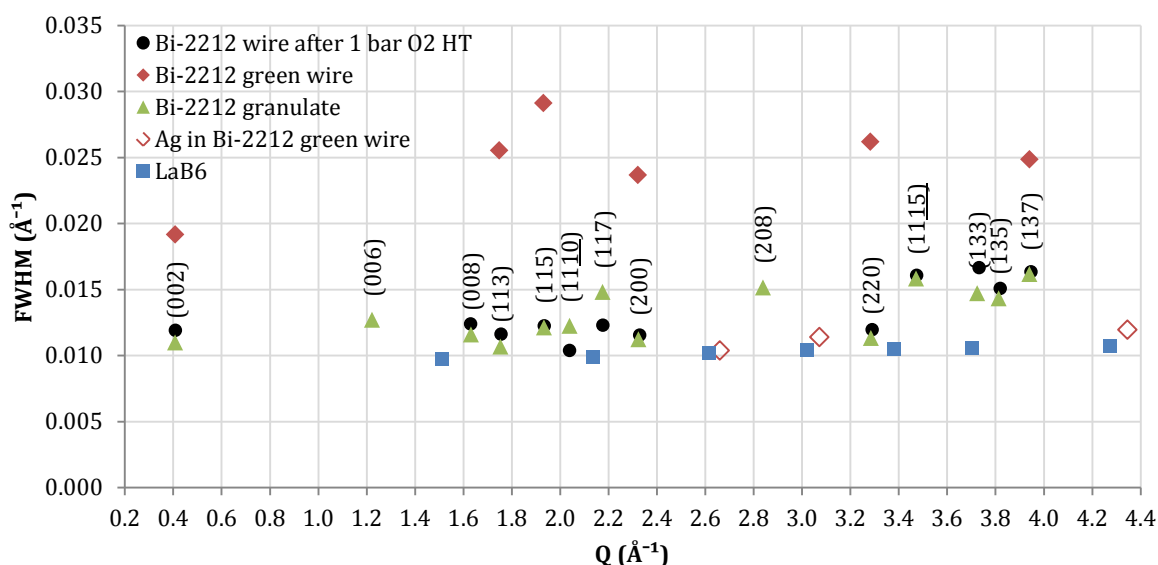


Figure 31 | Width (FWHM) of Bi-2212 diffraction peaks in precursor Bi-2212 granulate (labelled with Miller Indices), "green" Bi-2212/Ag wire (including Ag peaks) and the 1 bar O₂ fully processed Bi-2212/Ag wire. The widths of LaB₆ reference powder peaks are shown as an estimate for the instrumental peak broadening.

With the analysis of the static XRD patterns of precursor Bi-2212 granulate, non-processed "green" Bi-2212/Ag wire and 1 bar O₂ fully processed Bi-2212/Ag wire it could be shown that at both statuses (prior and after the HT) the filaments of the wire contain almost solely Bi-2212 with the same crystal structure as in the precursor Bi-2212 granulate and in the reference by Matheis et al. A development of texture could be observed as well as an increase of crystallite size.

4.4. XRD of *ex situ* processed Bi-2212/Ag wire quenched from 888 °C during in 1 bar O₂ HT

By quenching from 888 °C, the phases present during the melt state of Bi-2212 during the standard 1 bar oxygen HT, could be preserved. A comparison with multiple diffraction patterns (Bi-2212, Bi-2201, 2:3CF = Bi₂Sr₂CaO_{6+x}, (Ca_{0.4}Sr_{0.6})CuO₂ and Cu₂O) was performed but none of

them could be assigned with all of its peaks. The diffraction pattern of the quenched wire and the mentioned reference peaks are presented in Figure 32. Regarding the Bi-2212-Ag phase diagram in Figure 5, at least a Bi free $\text{SrCa}_x\text{CuO}_y$ and a Cu free $\text{Bi}_9\text{Sr}_{11}\text{Ca}_5\text{O}_x$ phase are expected in the liquid state of the filaments.

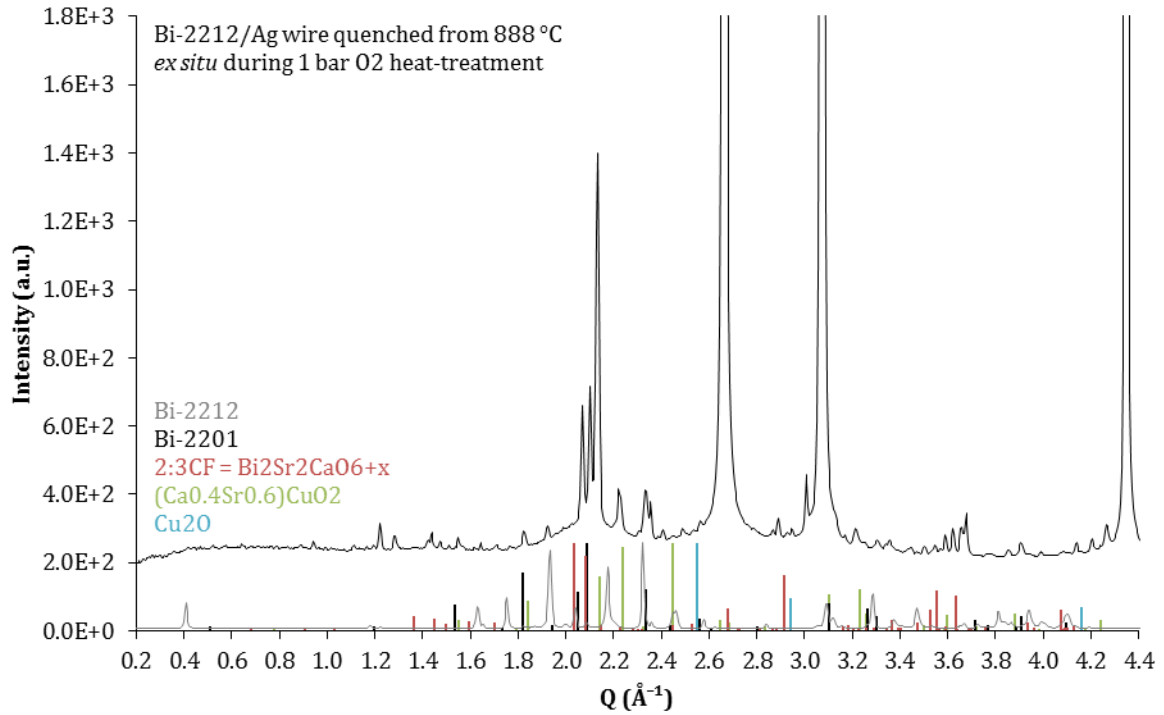


Figure 32 | XRD pattern of the Bi-2212/Ag wire quenched from 888 °C during 1 bar O_2 *ex situ* HT.

4.5. *In situ* processing of multifilament Bi-2212/Ag wire in 1 bar air

In order to study the evolution of Bi-2212 phase amount, melting point, recrystallisation after the partial melt, changes in the crystal structure and the presence of other phases during Bi-2212/Ag wire processing, *in situ* XRD measurements were done at the ID15A beam line at ESRF in an X-ray transparent furnace.

The *in situ* 1 bar air Bi-2212/Ag wire processing has been monitored by XRD measurements with identical experimental settings (e.g. synchrotron beam wavelength distribution, sample to detector distance) as those used for the static diffraction analysis above. Peak area analysis was done with the aid of the Excel-VBA tool that has been developed for this work (see Chapter 2.2). This program can efficiently analyse large XRD data sets acquired during continuous processes. Further peak position, width and shape analysis was done with aid of the Gaussian, Lorentzian and pseudo-Voigt fitting functions aiming the least square of the fitting difference.

An overview of the recorded XRD patterns as a function of HT duration is presented in Figure 33 in the d-spacing range of approximately 2.7 Å to 3.5 Å. This allows a view on the most important Bi-2212 (115), (117), (200) peaks present from the beginning and several other peaks ($Q = 2.047, 2.078, 2.108$ and 2.231 \AA^{-1}) present in the Bi-2212 melt state.

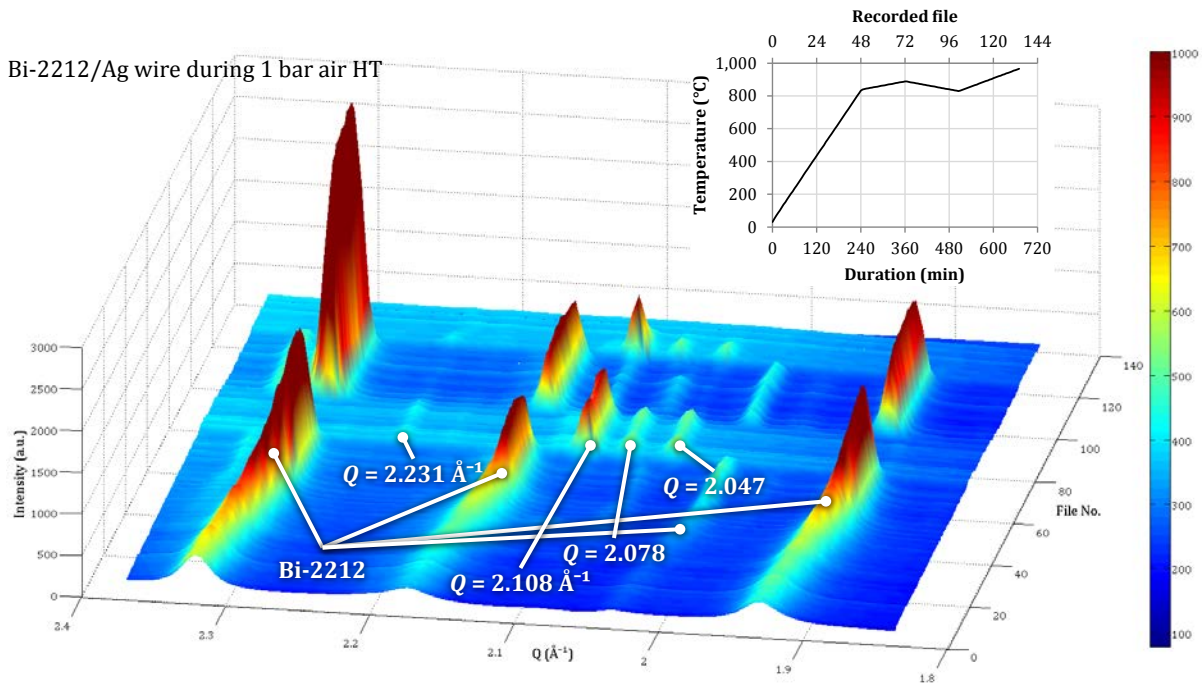


Figure 33 | Summary of diffraction patterns acquired during 1 bar air HT of the $\varnothing = 0.8$ mm Bi-2212/Ag wire. The inset shows the corresponding heat cycle.

Bi-2212 phase evolution

The intensity evolution of the main Bi-2212 peaks is shown in Figure 34 as a function of temperature, separately for the 1st heat-up the following cool-down and the 2nd heat-up period. Initially the intensity of the Bi-2212 diffraction peaks is increasing to approximately the double of its original value which is attributed to crystallisation of Bi-2212 that was strongly crushed during the wire drawing process [10]. During the temperature range of 850 to 880 °C the Bi-2212 phase is disappearing completely indicating the melting of Bi-2212. As shown in Figure 34 the Bi-2212 diffraction peaks reappear during the cool-down period in the temperature range of 865 to 830 °C where it nucleates out of the melt. But intensity ratios differ from the initial state. At 830 °C the Bi-2212 (200) to (113) intensity ratio is increased from 1:1 to 3:1. During the 2nd heat-up the Bi-2212 phase vanishes when the temperature reaches 885 °C. The changes in intensity ratio indicates a texture in the Bi-2212 phase. The Bi-2212/Ag wire sample that was fully processed in 1 bar O₂ shows a similar intensity ratios as observed here.

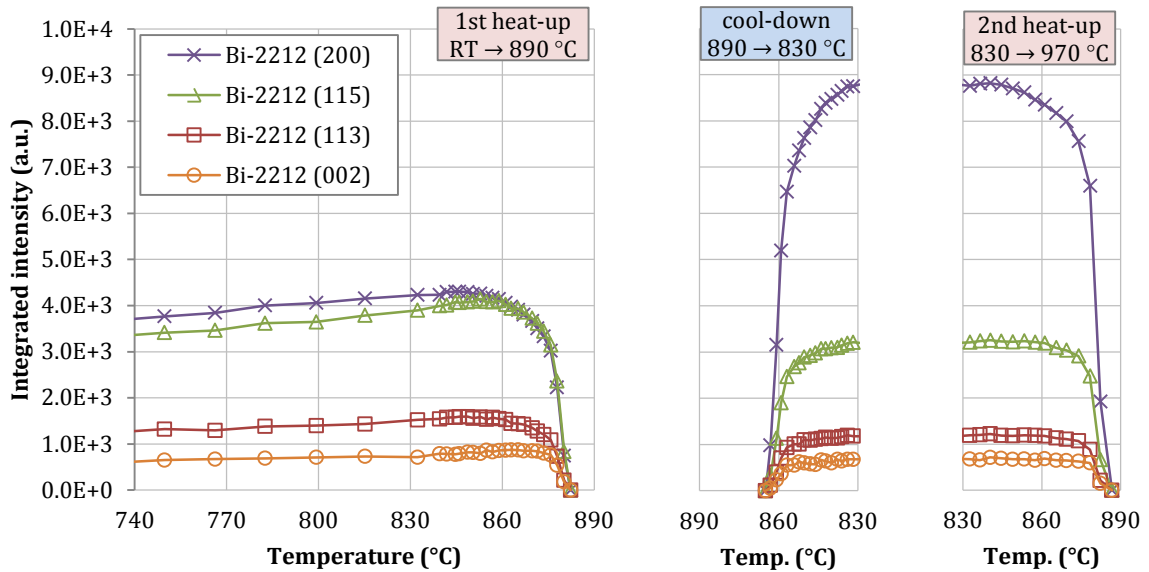


Figure 34 | Integrated intensity of the main Bi-2212 (002), (113), (115), (200) diffraction peaks as a function of temperature. Sample: $\varnothing = 0.8$ mm Bi-2212/Ag multifilament wire. HT: 1 bar air.

Figure 35 presents a detailed view of the varying melt and crystallisation temperature of the Bi-2212 phase. In this plot the intensity of the Bi-2212 (002), (113), (115) and (200) reflections were summed up. There is a slight difference of the temperature of about 4 °C at which Bi-2212 melts during the first and second heat-up. This can be explained by the different heat-up rates of +25 °C/h and +50 °C/h. During cooling with -25 °C/h the Bi-2212 growth is detected at about 17 °C lower temperature as the Bi-2212 melting (undercooling effect).

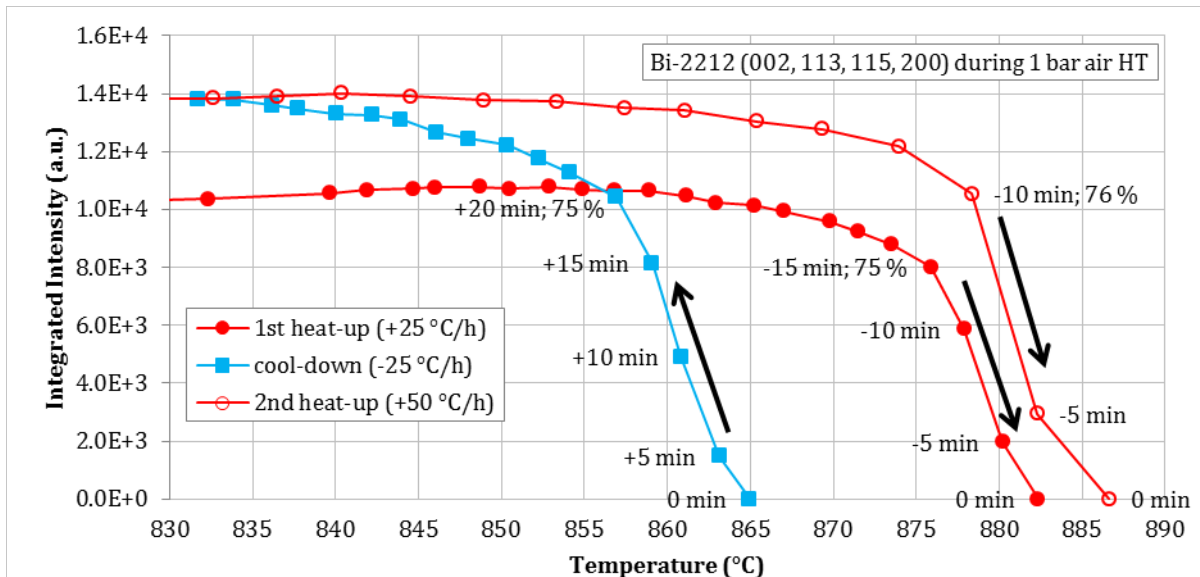


Figure 35 | Melting, nucleation and growth of the Bi-2212 phase. Sample: $\varnothing = 0.8$ mm Bi-2212/Ag wire. HT: 1 bar air.

Phase identification and evolution in the Bi-2212 liquid state

As it can be seen in Figure 33, in the same time as Bi-2212 melts, peaks of further phases are forming above 870 °C. The peaks have been labelled in the XRD pattern shown in Figure 36 that was acquired during the cool-down phase at 870 °C when the peaks have their highest intensity. Several peaks are most likely characteristic of orthorhombic $(\text{Ca}_{0.4}\text{Sr}_{0.6})\text{CuO}_2$ [38]. The further

diffraction pattern with three prominent peaks at $Q = 2.047, 2.078$ and 2.108 \AA^{-1} is very similar to the diffraction pattern of the quenched wire during the 1 bar oxygen HT.

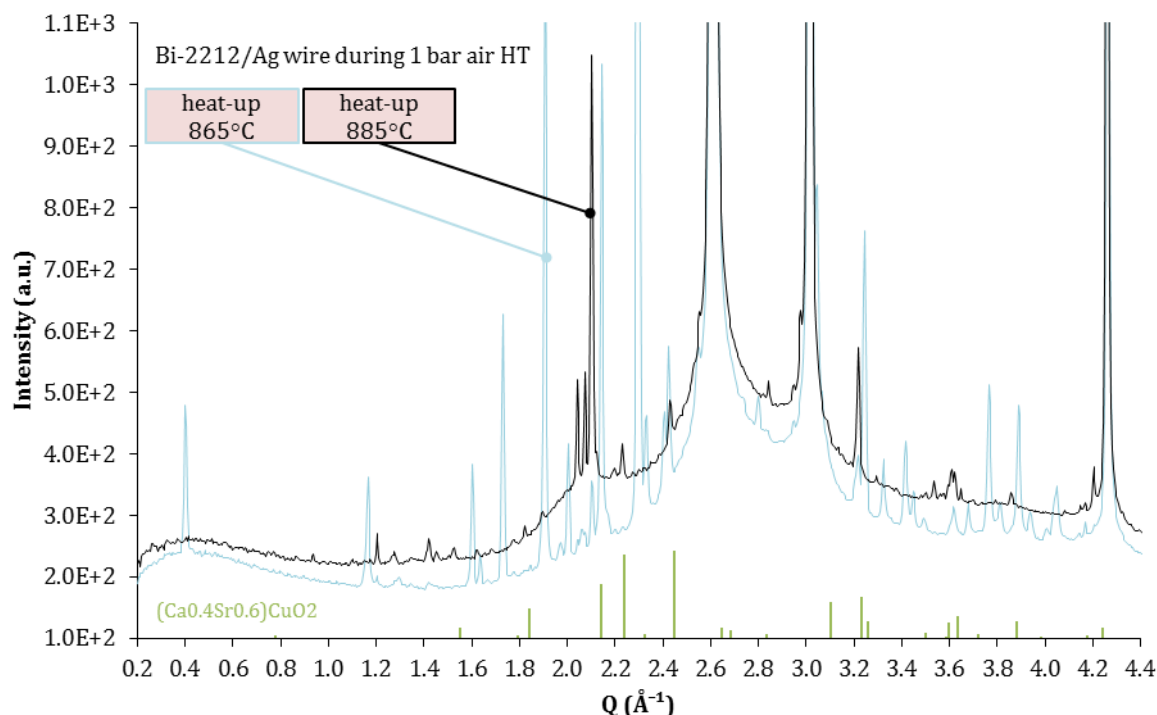


Figure 36 | XRD pattern of Bi-2212/Ag wire compound during 1 bar air HT at 865 and 885 °C during the 1st heat-up period. Reference diffraction pattern of $(\text{Ca}_{0.4}\text{Sr}_{0.6})\text{CuO}_2$ for comparison.

The evolution of the peak intensities of $(\text{Ca}_{0.4}\text{Sr}_{0.6})\text{CuO}_2$ and the peaks at $Q = 2.047, 2.078$ and 2.108 \AA^{-1} as a function of time is presented in Figure 37. $Q = 2.047$ and 2.078 \AA^{-1} and $\text{Ca}_{0.4}\text{Sr}_{0.6}\text{CuO}_2$ (130) peaks were selected to analyse as they are representing the two phases with little peak superposition. As it can be seen in Figure 33, both phases appear at 870 °C during the heat-up period. With a quick phase growth, maximum intensity is reached at 880 °C followed by a drop of about 30 % until the peak temperature of 890 °C. The global maxima is reached during the cool-down period at about 870 °C. Afterwards the peaks decrease in intensity down to 15 % of their maxima at 830 °C. Similarly to the first heat-up the peak intensities increase simultaneously during the second heat-up with a maximum intensity at about 885 °C. Upon further heating both phases vanish around 930 °C.

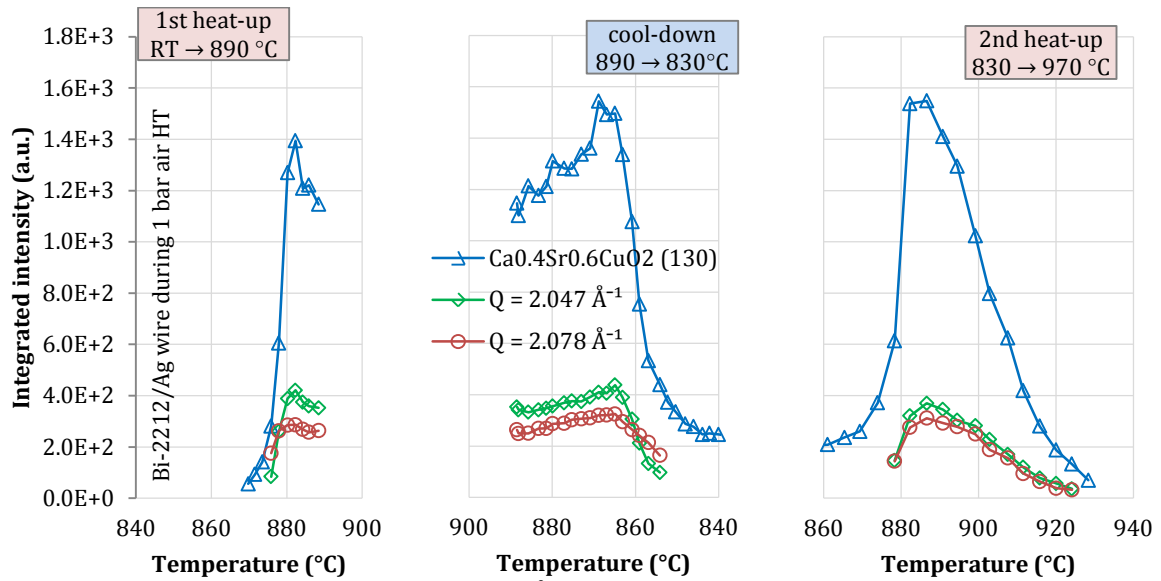


Figure 37 | Integrated intensity of $Q = 2.047$ and 2.078 \AA^{-1} and $(\text{Ca}_{0.4}\text{Sr}_{0.6})\text{CuO}_2$ (130) diffraction peaks as a function of temperature. Sample: $\varnothing = 0.8 \text{ mm}$ Bi-2212/Ag multifilament wire. HT: 1 bar air.

With the observed intensity evolution and composition of $Q = 2.047$ and 2.078 \AA^{-1} and $(\text{Ca}_{0.4}\text{Sr}_{0.6})\text{CuO}_2$ these both phases seem to partially alternate with the desired Bi-2212 phase. When Bi-2212 melts, the other phases appear. Thus both phases seem to be a decay product of the original Bi-2212 phase. But with the crystallisation of the Bi-2212 phase during the cool-down period a partial amount stays in the $Q = 2.047$ and 2.078 \AA^{-1} and $(\text{Ca}_{0.4}\text{Sr}_{0.6})\text{CuO}_2$ crystal structure.

Influence of temperature on peak intensity

As observable for instance at the Ag reflections, the intensities are decreasing slightly with increasing temperature. This is explained by increased thermal lattice motion which causes a reduction of peak intensity [39].

Ag melting temperature

The temperature at the end of the HT exceeding the melting temperature of Silver can be used to check the reliability of the temperature measurement. In the experiment the wire matrix containing pure Ag and an Ag-Mg composite with 0.2 wt.% Mg is melting in the range of 954 and 958 °C. The melting temperature of pure Ag is 961.93 °C and decreases with Mg content [40]. The Ag melting temperature as a function of oxygen partial pressure is described by Baker et al. (951 °C at 0.2 atm $p\text{O}_2$) [41] and by Lang et al. [42] when Bi-2212 is involved (see Figure 38).

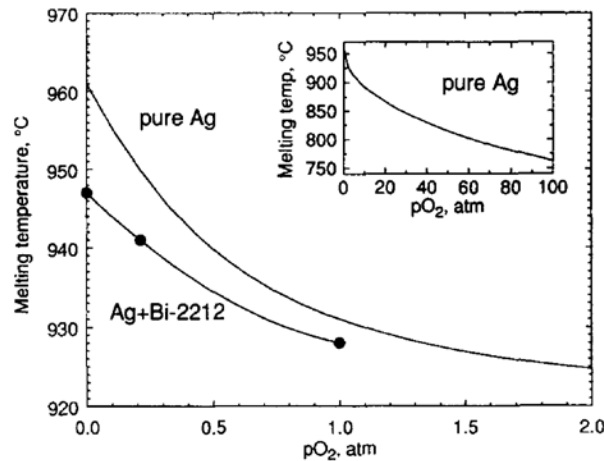


Figure 38 | Melting temperature of silver as a function of the oxygen pressure with and without presence of a Bi-2212 melt. Ag+Bi-2212: Lang et al. [42]; pure Ag line and inset: Baker et al. [41].

Bi-2212 peak width evolution

The Bi-2212 diffraction peak widths have been analysed in an attempt to extract information about crystallite size and anisotropic strain distribution during the HT.

In order to show the influence of the fitting function on the d-spacing and peak width results, peaks have been fitted with Lorentzian, Gaussian and pseudo-Voigt functions. First the influence of fitting function on FWHM and d-spacing is presented as an example on the Bi-2212 (113) peak in Figure 39 as a function of temperature.

The determined d-spacing evolution as a function of temperature are nearly independent of the applied fitting method. A linear slope of $1.33 \times 10^{-5} \text{ K}^{-1}$ for temperature induced expansion was determined. Shin et al. [43] are reporting $1.51 \times 10^{-5} \text{ K}^{-1}$ for the Bi-2212 phase in a Bi-2212/Ag wire compound and Tenbrink et al. [44] 1.1 to $1.2 \times 10^{-5} \text{ K}^{-1}$ for pure Bi-2212 and 1.8 to $2.1 \times 10^{-5} \text{ K}^{-1}$ for the Bi-2212 phase in a Bi-2212/Ag wire compound.

In contrast the FWHM results are significantly influenced by the fitting method. As presented in Figure 39, up to 700 °C the Lorentzian fit shows a higher broadening as the Gaussian fit. At higher temperature the widths coincidence. Nevertheless, the trend of decreasing peak width with temperature is similar for all fitting functions.

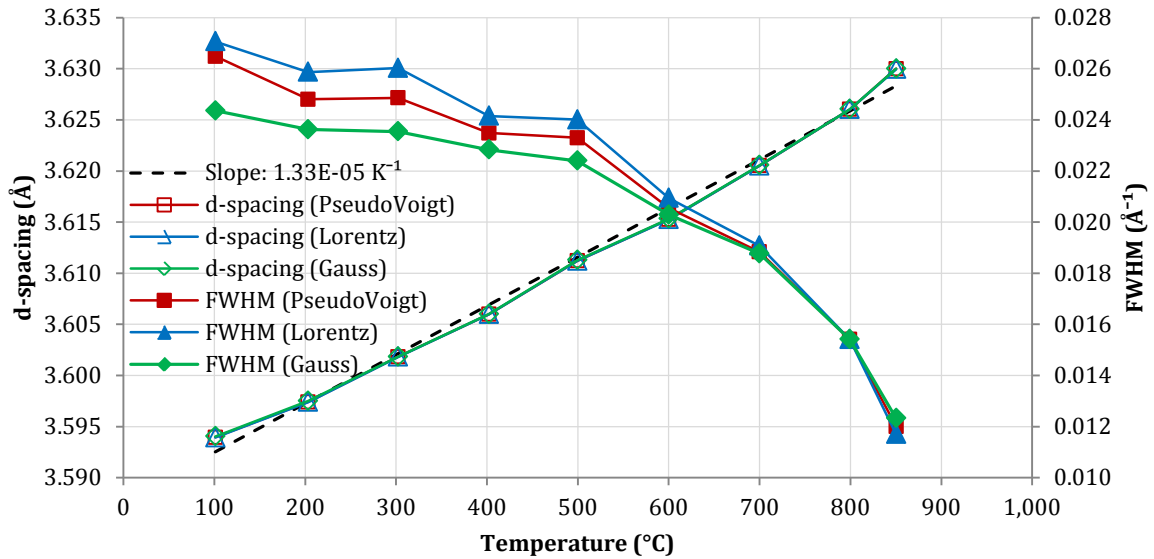


Figure 39 | Evolution of d-spacing and FWHM of Bi-2212 (113) peak. Comparison of Gaussian, Lorentzian and pseudo-Voigt fitting function. Sample: $\varnothing = 0.8$ mm Bi-2212/Ag multifilament wire. HT: 1 bar air.

The Bi-2212 (115) peak width and shape evolution as a function of temperature and duration is shown in Figure 40. The FWHM decreases with increasing temperature from its initial value of 0.0265 \AA^{-1} at $100 \text{ }^\circ\text{C}$ to 0.0120 \AA^{-1} at $850 \text{ }^\circ\text{C}$. The peak width attained right before the Bi-2212 melting is almost similar to the instrument induced broadening determined by the LaB_6 reference powder. When Bi-2212 is forming from the melt, the peak width stays similarly narrow until the lowest recorded temperature of $830 \text{ }^\circ\text{C}$.

As seen from the linear combination variable η of the pseudo-Voigt function, the diffraction peaks acquired at low temperature have a higher similarity to the Lorentzian distribution which suggests that the peaks are a superposition of various peaks for small and large crystallites (see Chapter 2.2). Reaching high temperatures the shape gets more and more Gaussian like. The Gaussian shape implies smaller amount of crystallites in the Bi-2212 phase.

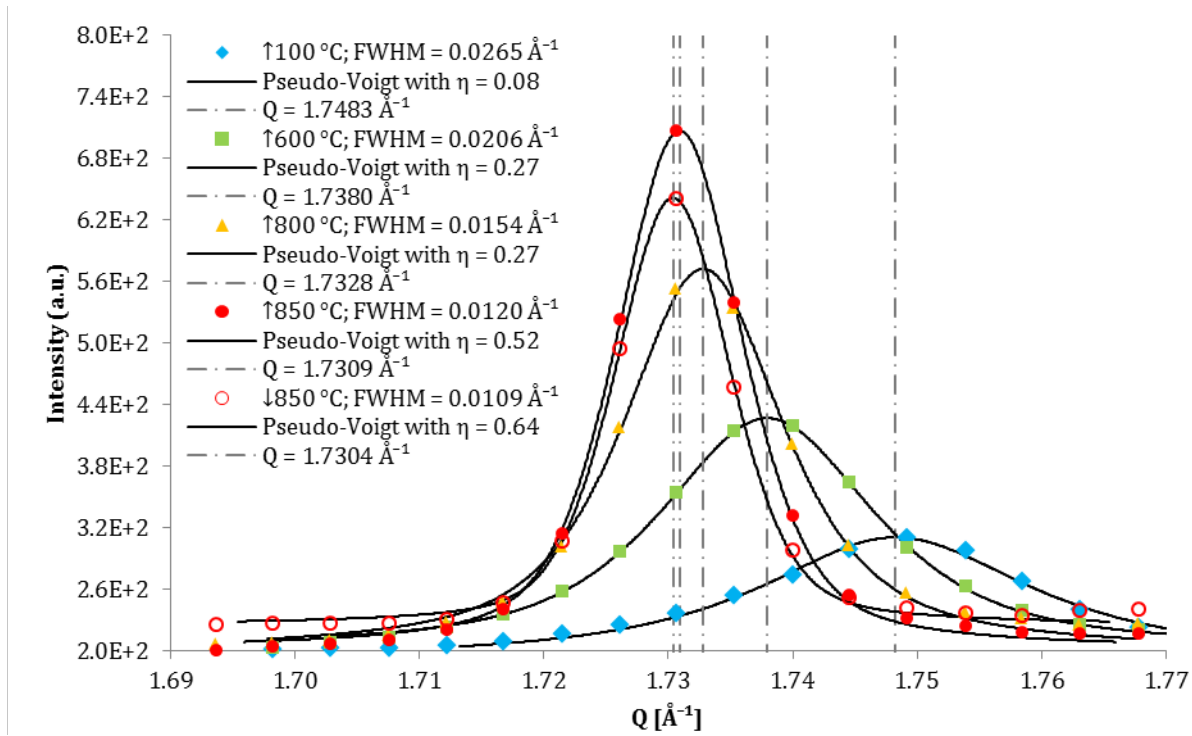


Figure 40 | Evolution of FWHM, η and Q of Bi-2212 (113) peak in the Bi-2212/Ag wire compound. Sample: $\varnothing = 0.8$ mm Bi-2212/Ag multifilament wire. HT: 1 bar air.

In Figure 41 the widths of selected Bi-2212 diffraction peaks are presented as a function of peak position and temperature. While at room temperature the peaks are broadened up to four times the instrument induced broadening, near the melting temperature of Bi-2212 the widths are hardly larger than the instrument induced peak broadening itself. Unfortunately it cannot be clearly distinguished between size and strain effects according to the Scherrer formulas [23]. A high variation of peak broadening avoids an accurate fit of the two functions to the measured data. The peaks were fitted with the pseudo-Voigt function (see Equation 5), but a remaining influence of peak superposition and/or background scattering is possible.

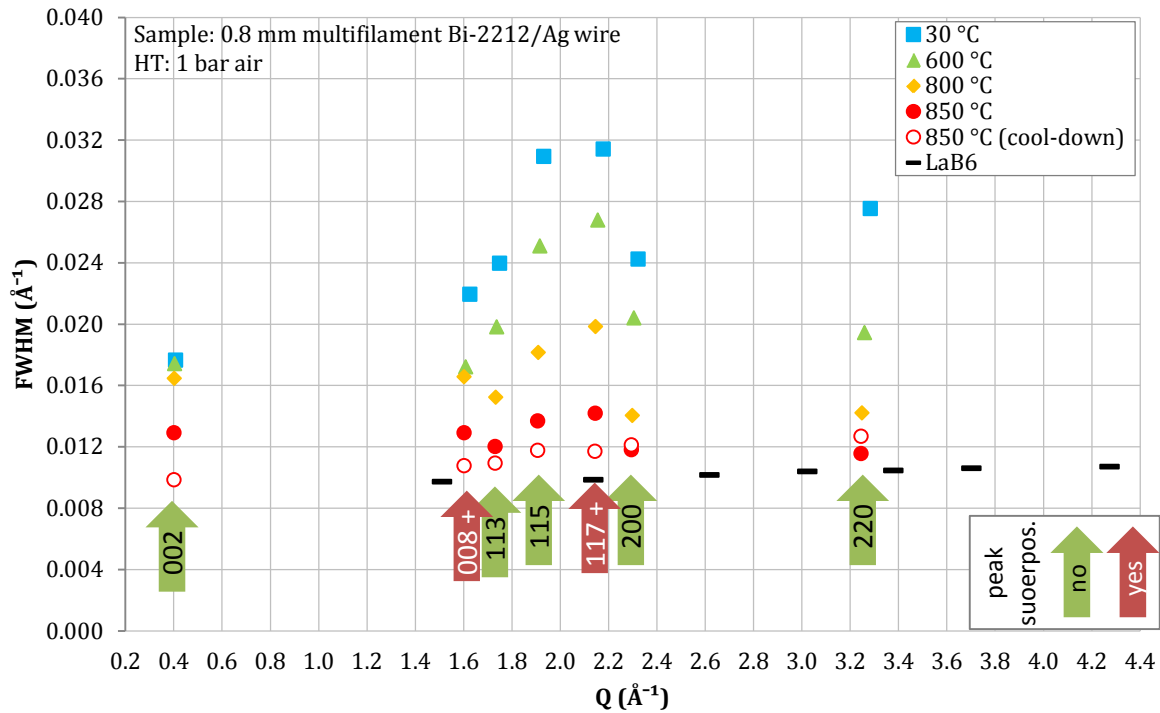


Figure 41 | Temperature dependence of Bi-2212 peak broadening and peak position in the Bi-2212/Ag wire compound during 1 bar air HT. LaB₆ reference powder shows only instrument induced peak broadening.

4.6. Influence of the oxygen partial pressure on the phase evolution of a Bi-2212/Ag wire during the processing

In order to see the influence of the oxygen partial pressure on the phase evolution of Bi-2212 and possibly other phases, two HTs were performed with identical temperature cycles and XRD settings during the MA-1252 experiment at ESRF ID15A, but with different process gases. The applied heat cycles with 1 bar air and 1 bar N₂ are similar to the experiment described above (see Figure 33) but have an additional isothermal plateau at 830 °C lasting 60 min.

In this experiment the synchrotron beam bandwidth was too large for a detailed peak width analysis (see instrument induced broadening shown in Figure 11). Nevertheless the intensity evolution is not affected by the relatively large instrumental peak broadening. Two plots of the HT in 1 bar air (see Figure 42) and 1 bar N₂ (Figure 43) show the evolution of all recorded diffraction patterns in a range of $Q = 1.8$ to 2.4 \AA^{-1} highlighting three main peaks of Bi-2212 and a view on characteristic peaks of further phases forming. A detailed presentation of the evolution of selected peak intensities is shown in Figure 44 as a function of HT duration.

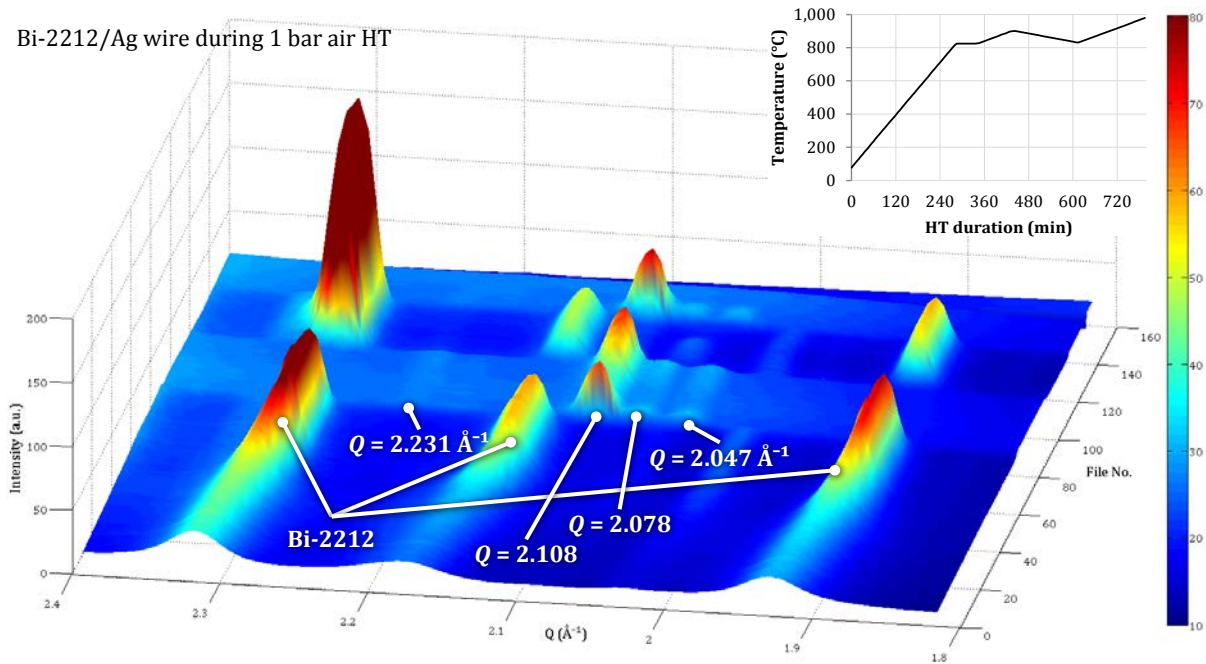


Figure 42 | Summary of diffraction patterns acquired during 1 bar air HT of the $\varnothing = 0.8$ mm Bi-2212/Ag wire. The inset shows the corresponding heat cycle.

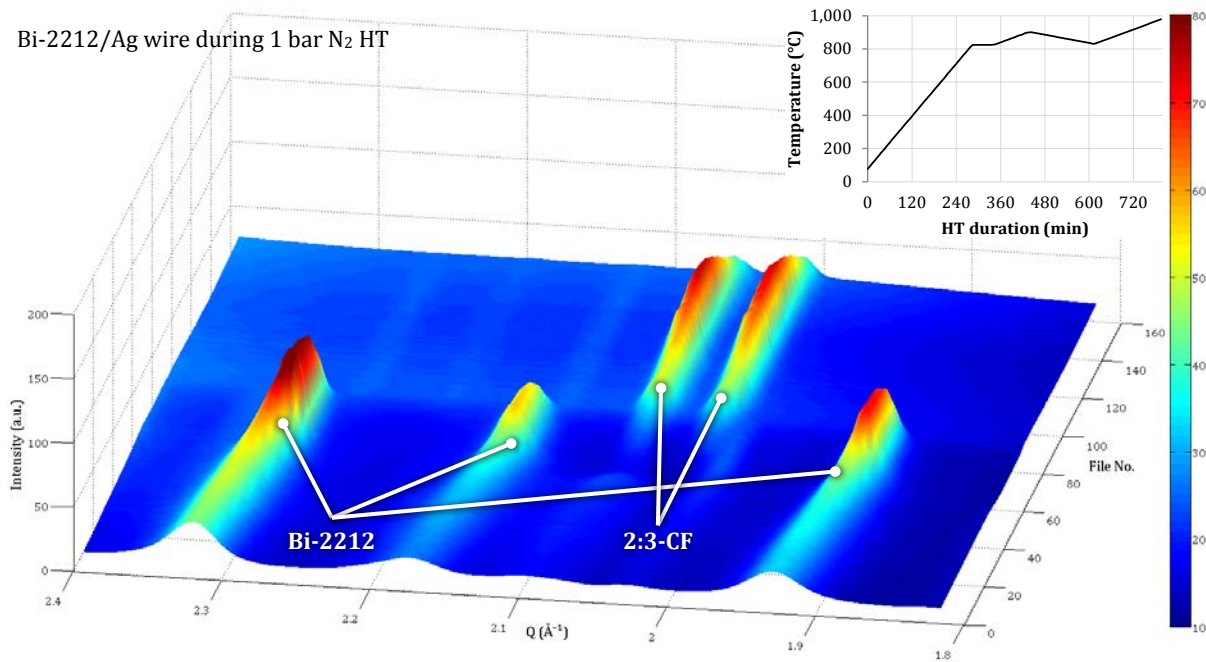


Figure 43 | Summary of diffraction patterns acquired during 1 bar N₂ HT of the $\varnothing = 0.8$ mm Bi-2212/Ag wire. The inset shows the corresponding heat cycle.

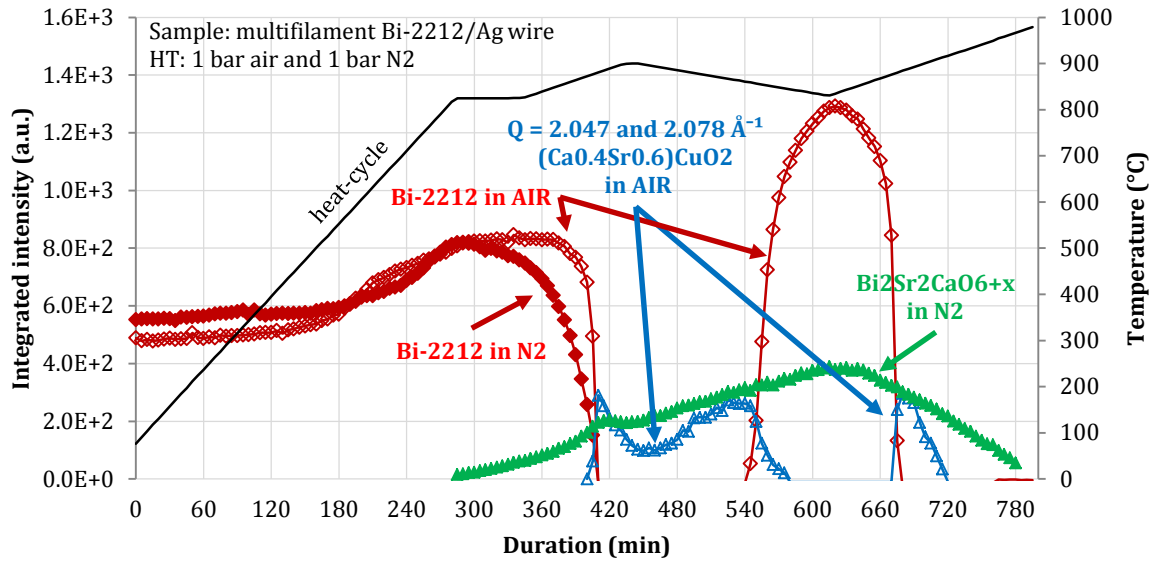


Figure 44 | Integrated intensity of selected Bi-2212, $\text{Bi}_2\text{Sr}_2\text{CaO}_{6+x}$, $(\text{Ca}_{0.4}\text{Sr}_{0.6})\text{CuO}_2$ and $Q = 2.047$ and 2.078 \AA^{-1} diffraction peaks as a function of HT duration. Sample: $\varnothing = 0.8 \text{ mm}$ Bi-2212/Ag multifilament wire. HT: 1 bar air and 1 bar N_2 .

Bi-2212 phase evolution

During the HT in air the diffraction intensity of the Bi-2212 phase remains almost constant during the isothermal $830 \text{ }^\circ\text{C}$ period, where the N_2 HT already initiates a decomposition of the Bi-2212 phase. In both HTs the Bi-2212 phase is completely vanished above $880 \text{ }^\circ\text{C}$ during the 1st heat-up period.

An important result is that only during the 1 bar air HT the Bi-2212 reappears in the cool-down period as described more detailed in Chapter 4.5. During the HT in 1 bar N_2 the Bi-2212 phase does not form during cool-down.

$\text{Bi}_2\text{Sr}_2\text{CaO}_{6+x}$, $(\text{Ca}_{0.4}\text{Sr}_{0.6})\text{CuO}_2$ and $Q = 2.047$ and 2.078 \AA^{-1} phase evolution

As shown in Figure 44, the appearance of other phases occurs simultaneously when Bi-2212 vanishes. During the HT in 1 bar air these phases are $(\text{Ca}_{0.4}\text{Sr}_{0.6})\text{CuO}_2$ and at least one more phase with prominent diffractions peaks at $Q = 2.047$, 2.078 and 2.108 \AA^{-1} . These which were already observed in the previous high resolution *in situ* analysis of the 1 bar air HT (see in Figure 33 and more detailed in Figure 37). Applying N_2 as process gas, the reference diffraction pattern of $\text{Bi}_2\text{Sr}_2\text{CaO}_{6+x}$ accords to the observed peaks (see Figure 45).

Until a temperature of approximately $825 \text{ }^\circ\text{C}$ the diffraction pattern of the Bi-2212/Ag wire contains only peaks of the Bi-2212 and Ag phase. Above, the hexagonal $\text{Bi}_2\text{Sr}_2\text{CaO}_{6+x}$ phase can be detected as presented in Figure 45.

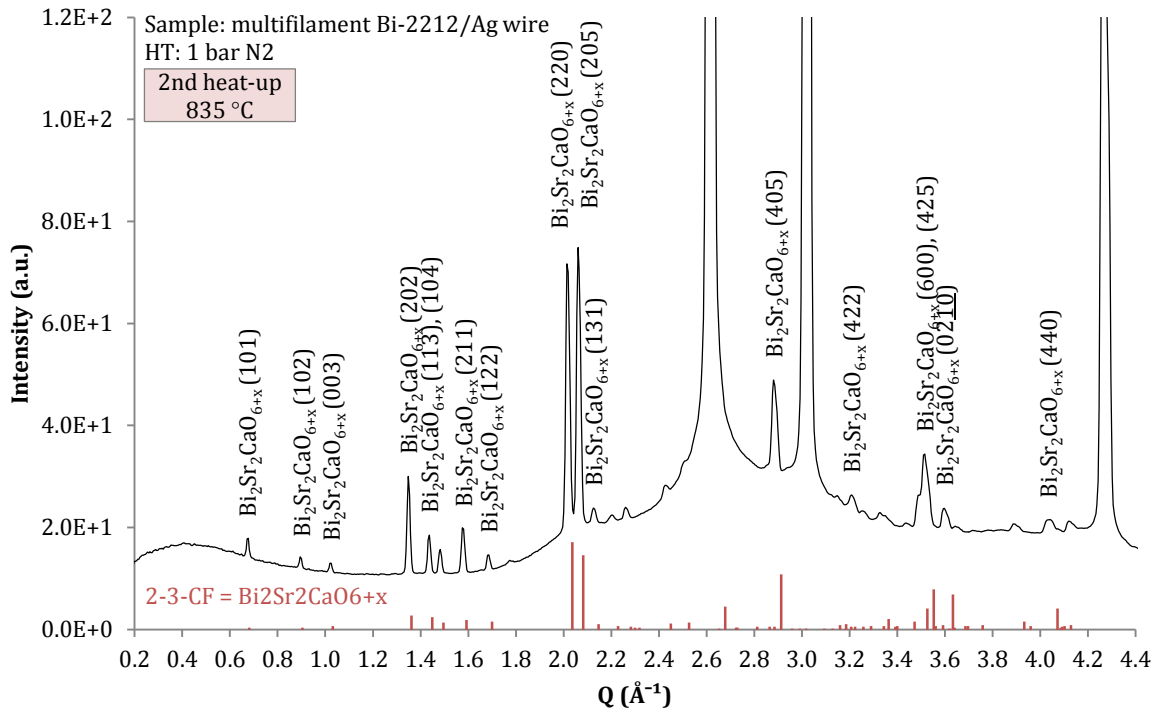


Figure 45 | XRD pattern of the Bi-2212/Ag wire at 835 °C (2nd heat-up) during 1 bar N₂ HT with main Bi₂Sr₂CaO_{6+x} peaks labelled.

Three of the most intense Bi₂Sr₂CaO_{6+x} peaks have been tracked through the 1 bar N₂ HT. The peak (220) at $Q = 2.017 \text{ \AA}^{-1}$ is initially superimposed by Bi-2212 (117) but further shows a very similar evolution as the other peaks of the phase. In comparison to the phase evolution of Bi-2212 it is clearly visible, that Bi₂Sr₂CaO_{6+x} starts to form just in the same range of temperature as Bi-2212 decreases (830 to 880 °C). The maximum intensity of Bi₂Sr₂CaO_{6+x} is reached at the end of the cool-down period at 830 °C. During the 2nd heat-up period, the phase vanishes again with a constant slope ending at the maximal temperature of 970 °C where the recording stops. A complete disappearance is expected at slightly higher temperature.

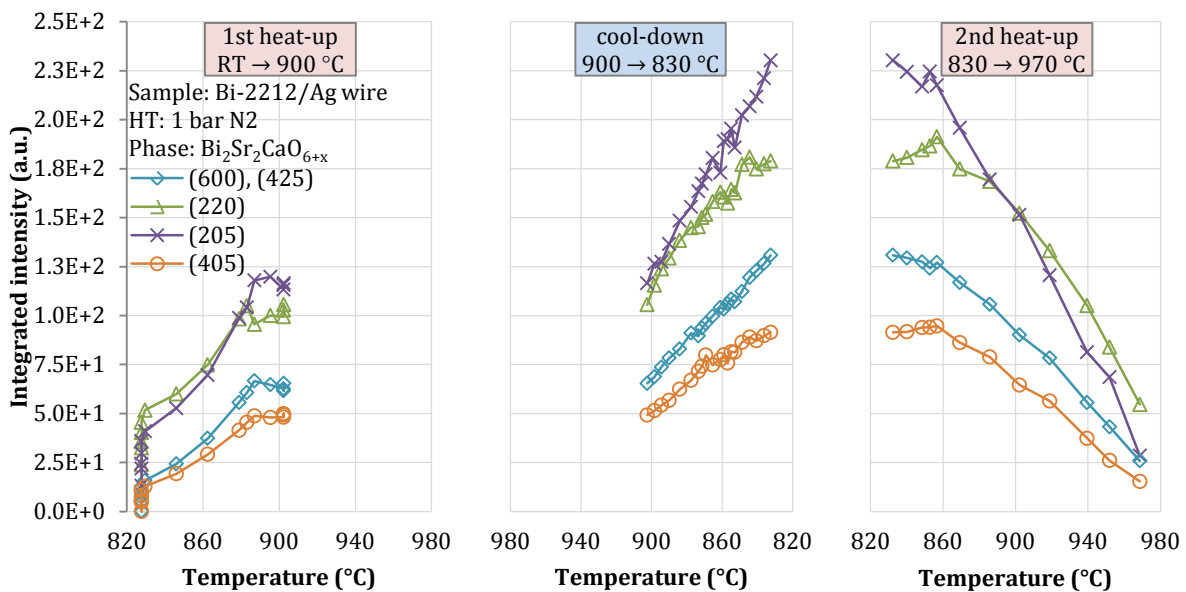


Figure 46 | Integrated intensity of selected Bi₂Sr₂CaO_{6+x} diffraction peaks as a function of temperature. Sample: $\varnothing = 0.8$ mm Bi-2212/Ag multifilament wire. HT: 1 bar N₂.

Ag phase evolution

Forming the matrix of the wire, the Ag phase is present during the complete HT with its integrated intensities decreasing almost linear as a function of temperature. The decrease is caused by the thermal motion effect [39], as described in Chapter 4.5. An analysis of the reflection Ag (111) shows that its peak width stays as low as the instrument induced broadening during the whole HT. Furthermore the phase evolution is very similar to the initial 1 bar air heat-treatment analysed above in detail.

4.7. *In situ* processing of multifilament Bi-2212/Ag wire in 100 bar air

In order to do a feasibility test of *in situ* XRD measurements at high pressure, a 100 bar air HT up to 900 °C was done with a similar $\varnothing = 0.8$ mm multifilament Bi-2212/Ag wire sample as used in the experiments described above. While the instruments were working well and the pressure could be maintained with high precision (± 2 bar), the sample was damaged during the experiment and only the first results obtained during the heat-up period up to about 890 °C are considered to be reliable.

An overview of the diffraction pattern acquired during the 100 bar air HT is presented in Figure 47 in the range of $Q = 1.7$ to 2.4 \AA^{-1} . Three peak of the Bi-2212 phase, two peaks that are assigned to “P-HT100-a” and one peak that is assigned to “P-HT100-b” are highlighted.

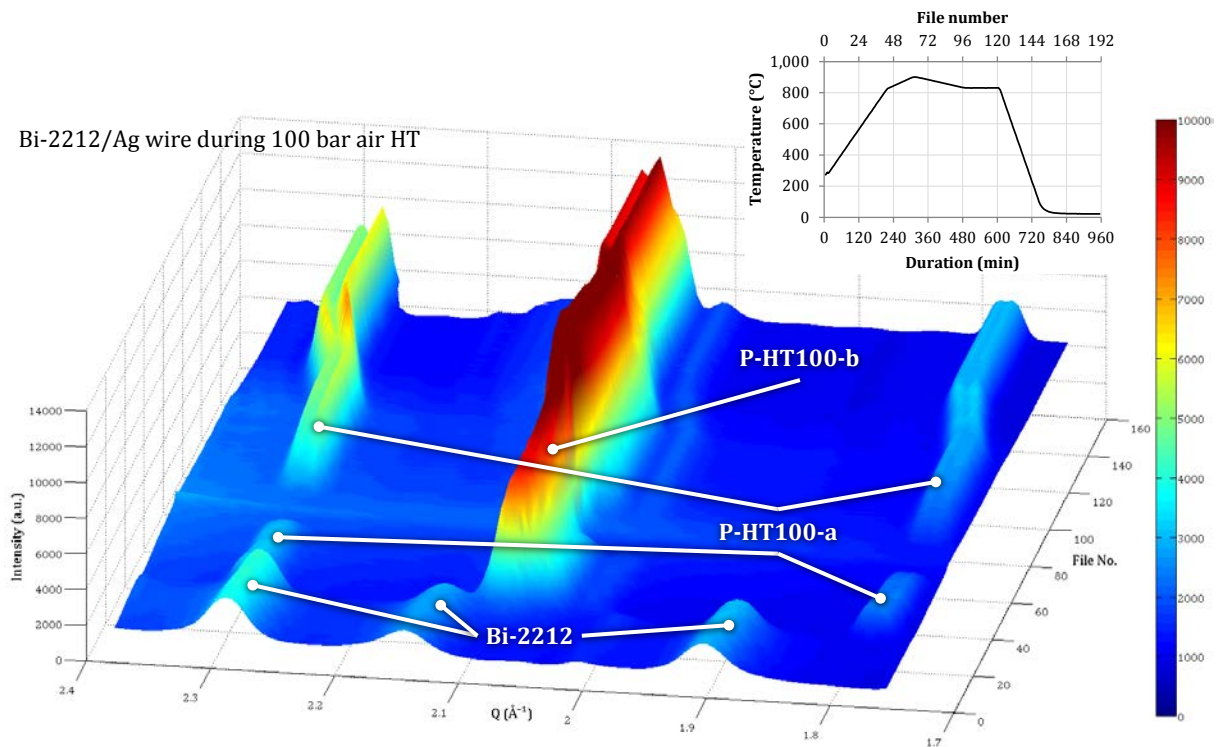


Figure 47 | Summary of diffraction patterns acquired during the 1 bar air HT of the $\varnothing = 0.8$ mm Bi-2212/Ag wire. The inset shows the corresponding heat cycle.

Ag phase evolution

Figure 48 shows the evolution of the integrated intensities of three Ag diffraction peak areas during the HT. The initial decrease of Ag peak area can at least partly be explained by increasing thermal lattice movement with increasing temperature [44]. The following fast drop in intensity during a nearly constant temperature between 880 °C and 900 °C is probably caused by the burst of the silver matrix, which can be seen in the sample photo in Figure 49. By lowering the temperature at the end of the HT the Ag intensity increases again slightly due to the temperature dependence explained above.

In the experiment the wire matrix containing pure Ag and an Ag-Mg composite with 0.2 wt.% Mg is melting in the range of 954 and 958 °C. The melting temperature of pure Ag is 961.93 °C and decreases with the amount of Mg alloy [40]. Further decrease reasons are described by Baker et al. [41] with increasing oxygen partial pressure (~ 870 °C at 21 atm p_{O_2}) and by Lang et al. [42] when Bi-2212 is involved in the melt.

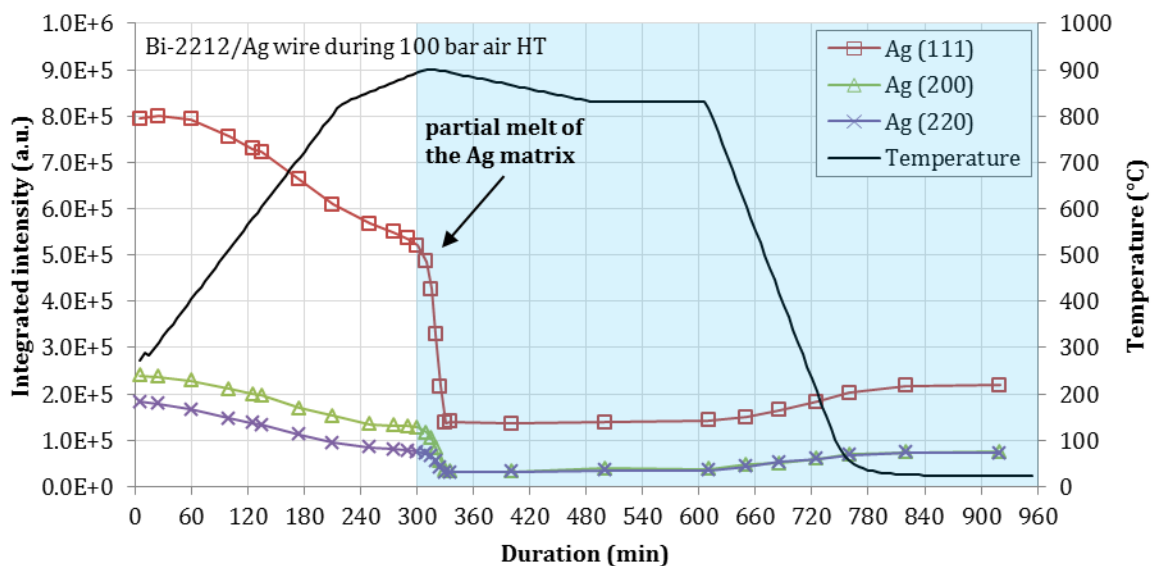


Figure 48 | Integrated intensity of Ag (111), Ag (200) and Ag (220) diffraction peaks as a function HT. Sample: $\varnothing = 0.8$ mm Bi-2212/Ag multifilament wire. HT: 100 bar air.

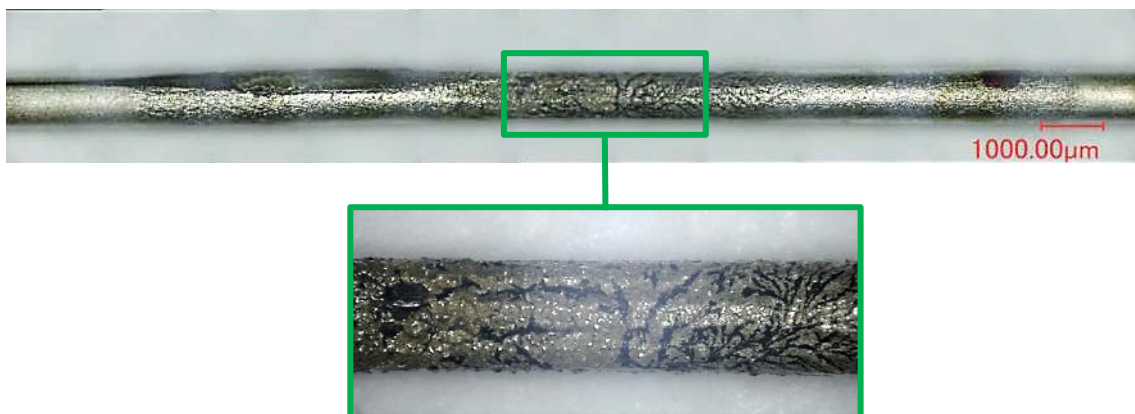


Figure 49 | Leakage of Bi-2212/Ag wire after the 100 bar air HT. (Courtesy Norberto Jimenez Mena, CERN)

Bi-2212 phase evolution

The evolution of the integrated intensity of selected Bi-2212 peaks is shown in Figure 50 as a function of temperature. Initially the intensity stays almost constant. Between 580 °C and 660 °C the Bi-2212 phase vanishes completely which is about 200 °C lower as observed during HT in 1 bar air and does not reappear during the remaining HT. The vanish of the Bi-2212 peaks is at least 200 °C below the anomalous behaviour of Ag and is thus assumed to be a reliable result.

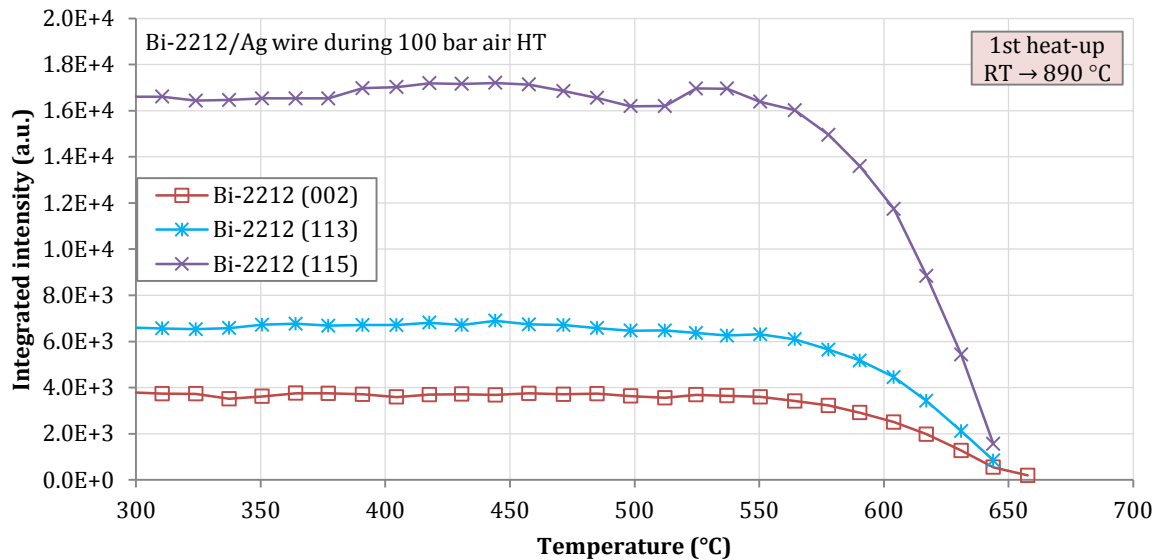


Figure 50 | Integrated intensity of Bi-2212 (002), (113), (115) diffraction peaks as a function temperature. Sample: \emptyset = 0.8 mm Bi-2212/Ag multifilament wire. HT: 100 bar air.

“P-HT100-a” and “P-HT100-b” phase evolution

Beside the clearly identifiable diffraction peaks of Bi-2212 and Ag, several other peaks are visible after the Bi-2212 phase just disappeared. A clear identification however has not been fulfilled until now. Figure 51 shows the XRD pattern of the Bi-2212/Ag wire at 510 °C and 780 °C during the heat-up both below Ag anomaly. The main identified peaks in the pattern at 780 °C are labelled with their position.

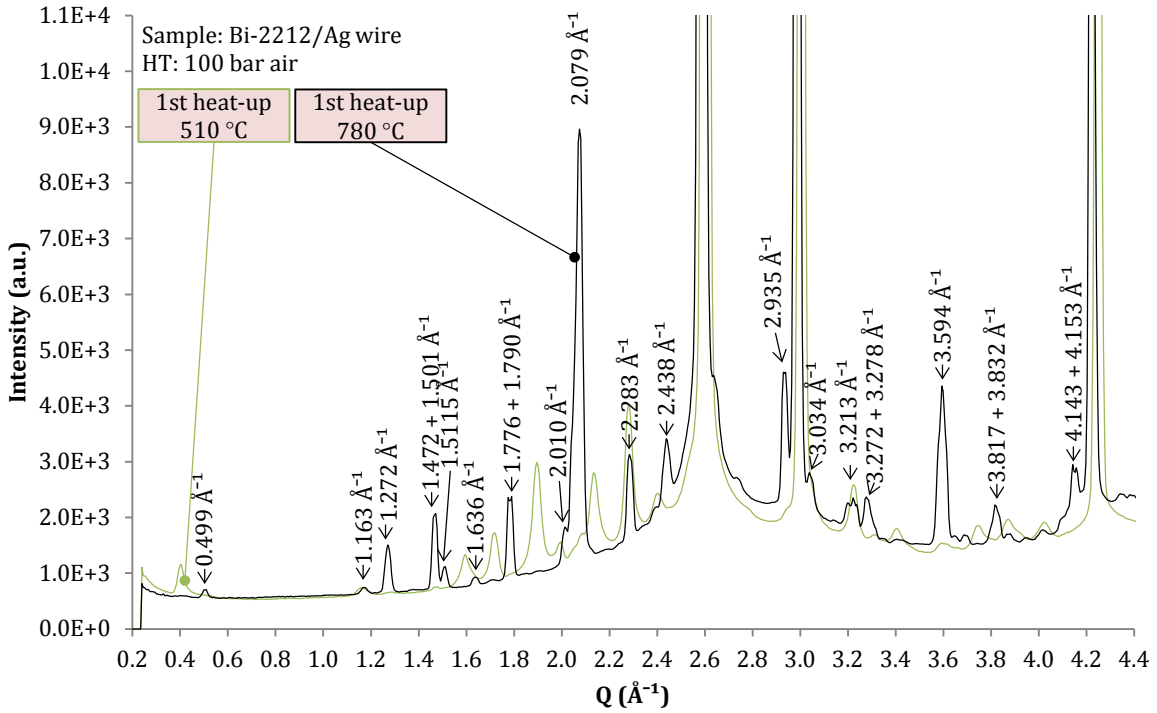


Figure 51 | XRD pattern of the Bi-2212/Ag wire at 510 °C and 780 °C. HT: 100 bar air.

The intensity evolution of five significant peaks is presented in Figure 52 as a function of temperature during heat-up and cool-down. All peaks rise constantly in the range of 550 to 650 °C where Bi-2212 vanishes. The following trend can be categorized to two different groups of peaks. The peaks at $Q = 0.499, 1.775, 1.790$ and 2.286 \AA^{-1} (to be referred as “P-HT100-a”) vanish again at $\sim 895 \text{ °C}$. But the other peaks at $Q = 1.271$ and 3.596 \AA^{-1} (to be referred as “P-HT100-b”) stay with almost constant intensity until the end of the HT. The variance of phase P-HT100-a above 850 °C may be explained by the drop of absorption caused by the filament surrounding Ag matrix that presumably melts.

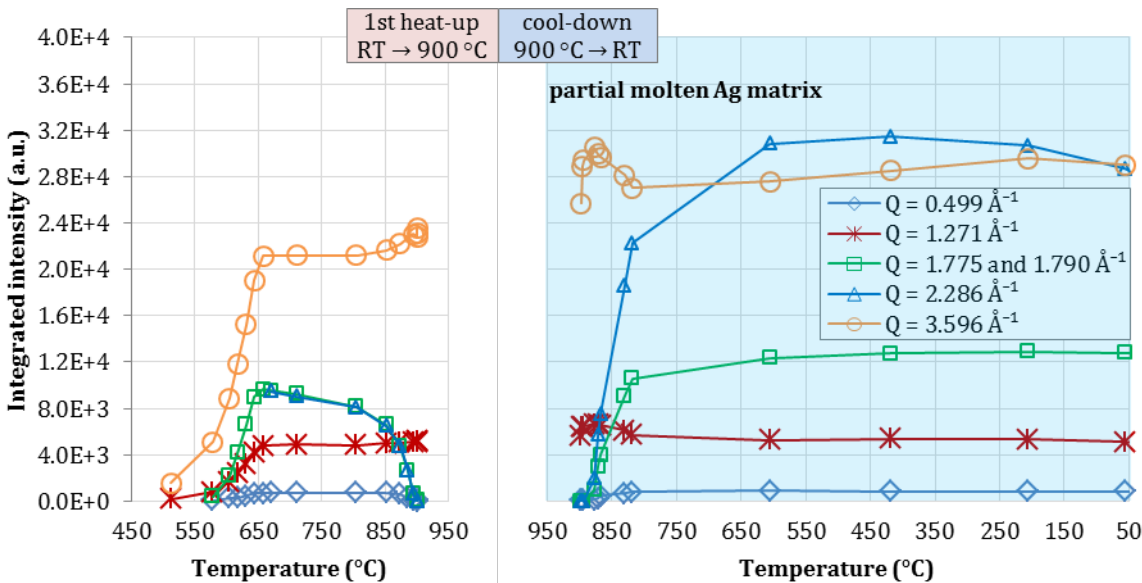


Figure 52 | Integrated intensity of diffraction peak at $Q = 0.499, 1.271, 1.775, 1.790, 2.286$ and 3.596 \AA^{-1} as a function temperature. Sample: $\varnothing = 0.8 \text{ mm}$ Bi-2212/Ag multifilament wire. HT: 100 bar air.

In Table 7 the peak position of phase P-HT100-a and P-HT100-b are summarised.

Table 7 | Peak position of selected P-HT100-a and P-HT100-b phase reflections.

Q (\AA^{-1})	0.499	1.163	1.272	1.472	1.501	1.512	1.636	1.776	1.790	2.010	2.079	2.283	2.438	2.935	3.034	3.213	3.272	3.278	3.594	3.817	3.832	4.143	4.153	
P-HT100-a	+	+				+	+	+	+	+	+	+		+	+	+			+					
P-HT100-b			+	+	+						+		+	+		+	+	+	+	+	+	+	+	+

The phases P-HT100-a and P-HT100-b could not yet be identified. Nonetheless the peaks of P-HT100-a and P-HT100-b show similarities with the phases $\text{Bi}_2\text{Sr}_2\text{CaO}_{6+x}$ and $\text{Ca}_{0.4}\text{Sr}_{0.6}\text{CuO}_2$ that were observed in the other experiments. But some peaks like those at $Q = 1.78$ and 2.28 \AA^{-1} do not fit to the references. Due to the very high indirect connection to the diffraction intensity of the Bi-2212 phase it is assumed that P-HT100-a and P-HT100-b are a reconfiguration of the Bi-2212 atoms.

4.8. *In situ* processing of single core Bi-2212/Ag wire in 1 bar air

The phase and microstructure evolution of a Bi-2212/Ag single core wire has been monitored by combined XRD and μ -CT during an *in situ* HT in 1 bar air. In the single core wire with an outer diameter of ~ 1 mm structure can be observed in more detail as it is possible in multifilament wires. The summary of recorded XRD patterns in the range of 1.8 to 2.4 \AA^{-1} is presented in Figure 53.

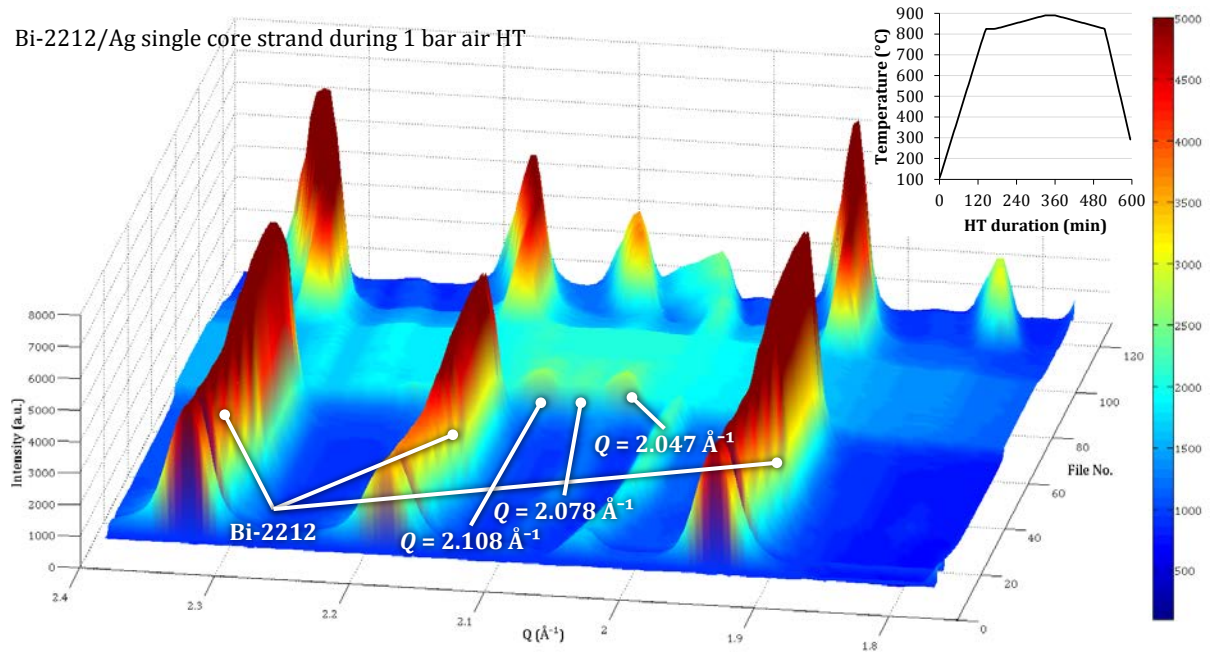


Figure 53 | Summary of diffraction patterns acquired during 1 bar air HT of the single core Bi-2212/Ag wire. The insertion shows the corresponding heat cycle.

4.8.1. XRD peak area evolution analyses

Prior to the analysis of diffraction peak intensities the diffraction patterns are normalised to the photon flux, which is measured by a photo sensitive diode placed in front of the sample in advance to each XRD recording. In the present experiment this normalisation seems to have failed, as the evolution of integrated intensities of the entire diffraction patterns suggest, which is shown in Figure 54. The constant slight drop of intensity with time is due to usual synchrotron beam intensity loss. The synchrotron refill, which takes place a few times per day, has presumably caused the jump of intensity after about 270 min. A drop of intensity after about 100 min HT duration is most probably due to the simultaneous drop of Ag diffraction peak intensity (see Figure 55) that is presumably caused by partial Ag melting. To see the influence of diffraction pattern normalisation, Figure 55 and Figure 56 are presented as a comparison of results with and without normalisation. In Figure 56 the diffraction patterns have been normalised to the integrated intensity of each entire diffraction pattern, assuming that the intensity fluctuations shown in Figure 54 would be only caused by the beam flux variance. This normalisation has to be considered as a rough approximation.

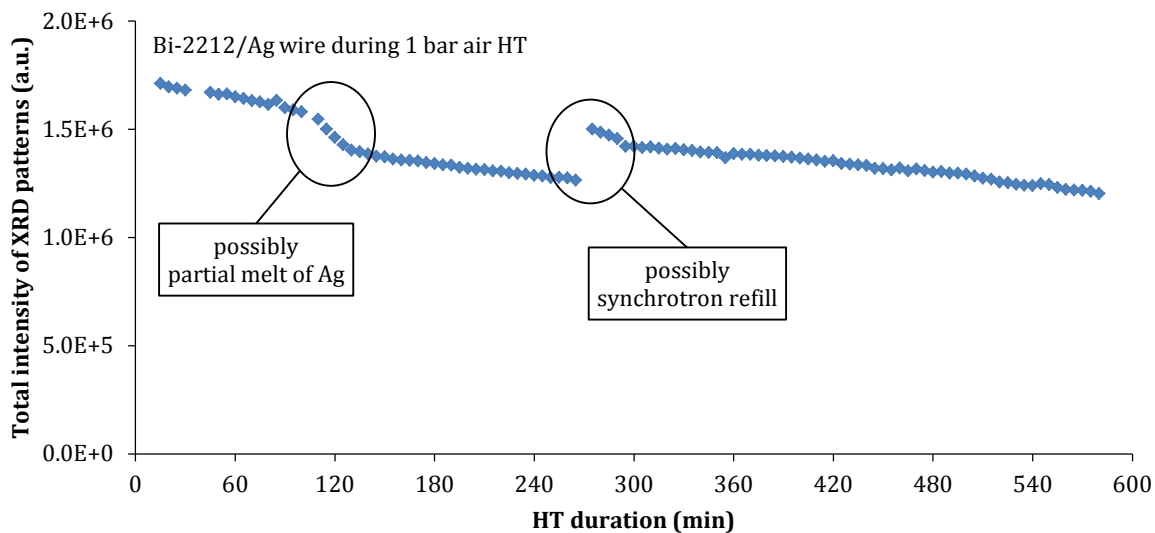


Figure 54 | Evolution of integrated intensity of diffraction patterns (diffraction peaks and background) during the HT of the 1 mm single core Bi-2212/Ag wire.

The Bi-2212 phase behaves similarly as during the 1 bar air HT of the multifilament Bi-2212/Ag wire. An initial increase is followed by melting of the phase at high temperatures and a reforming of the Bi-2212 phase during the cool-down period. While the Bi-2212 phase is molten, further peaks appear e.g. at $Q = 2.047, 2.078$ and 2.108 \AA^{-1} . They are likely to be from the same phase as it was identified during the 1 bar air and 1 bar oxygen HT of the multifilament wire described above. These peaks vanish again during the cool-down before Bi-2212 crystallises again. Bi-2201 is detected during the cool-down period.

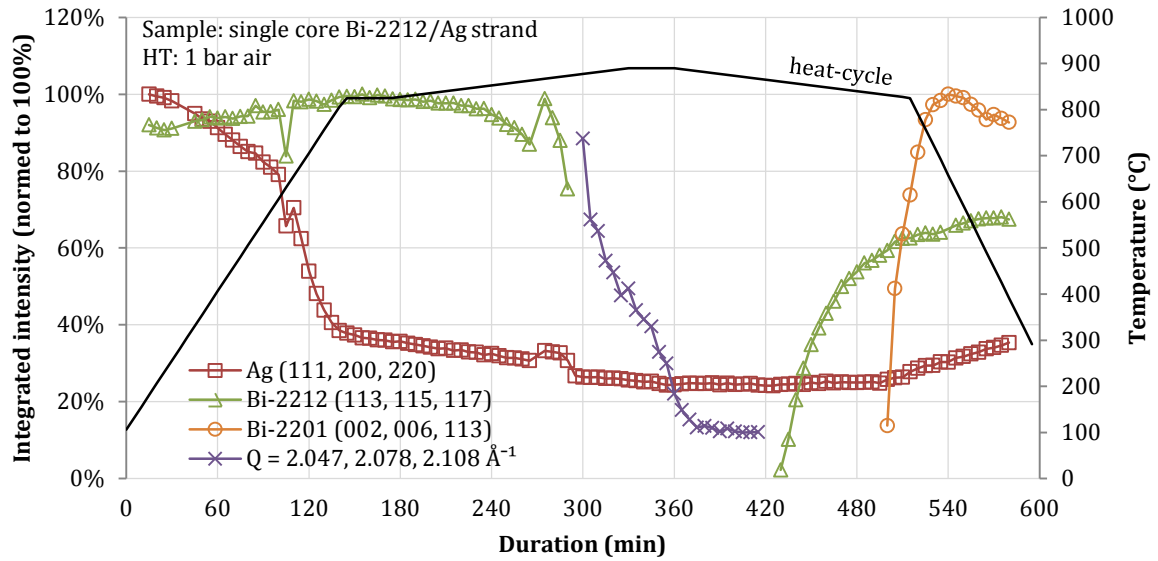


Figure 55 | Bi-2212, Bi-2201, Ag and P4 phase evolution as a function of HT duration. Sample: $\varnothing = 1$ mm single core Bi-2212/Ag wire. HT: 1 bar air. (not normalised)

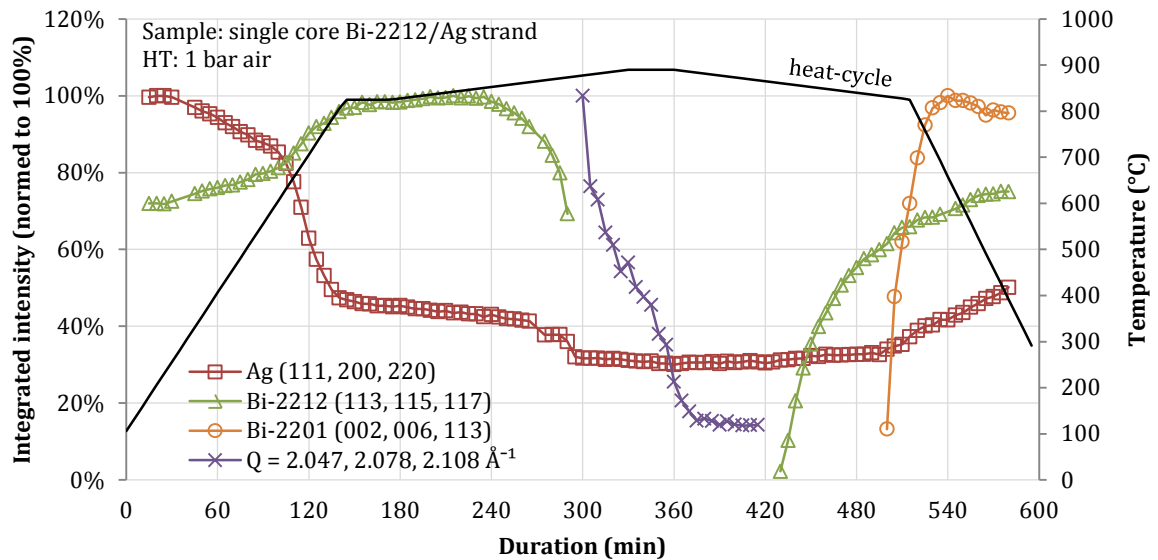


Figure 56 | Bi-2212, Bi-2201, Ag and P4 phase evolution as a function of HT duration. Sample: $\varnothing = 1$ mm single core Bi-2212/Ag wire. HT: 1 bar air. (normalised to XRD patterns total intensity)

Bi-2212 phase evolution

The Bi-2212 phase behaves similar as observed in the Bi-2212/Ag multifilament wire experiment, with an initial increase of Bi-2212 intensity to approximately 140 % at 850 °C. Afterwards all Bi-2212 reflections decrease and vanish completely above 875 °C, indicating that Bi-2212 is molten. During the cool-down period, Bi-2212 reforms in the range of 860 to 830 °C visible in Figure 57 and Figure 59.

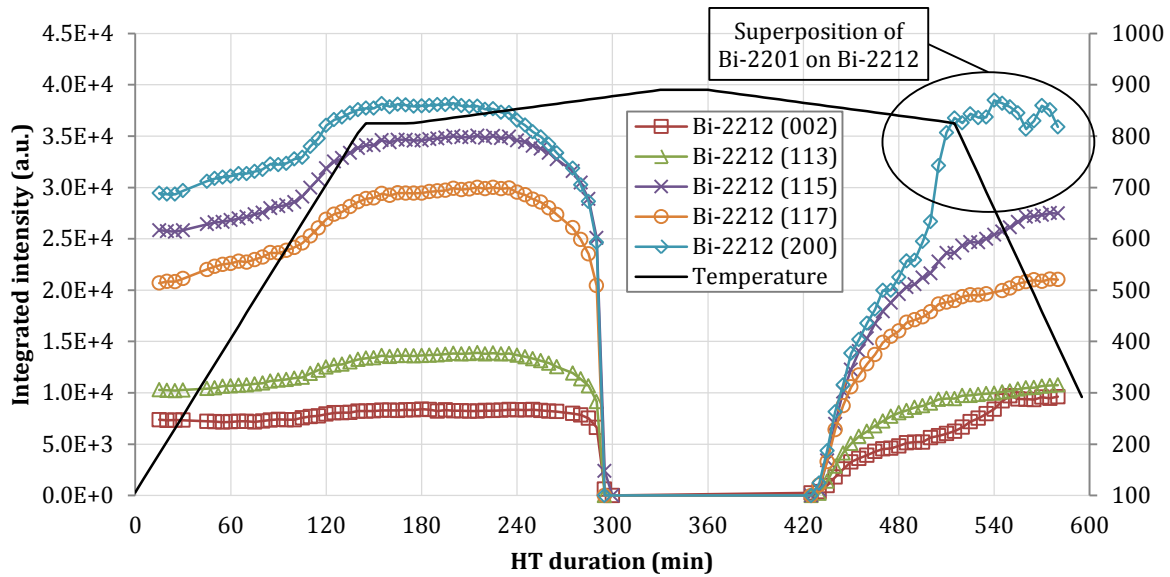


Figure 57 | Integrated intensity evolution of Bi-2212 (002), (113), (115), (117) and (200) peaks as a function of HT duration. Sample: $\varnothing = 1$ mm single core Bi-2212/Ag wire. HT: 1 bar air.

Unlike in the multifilament experiments described above, Bi-2212 intensities remain lower than they were before melting. This behaviour is unclear but may be an experimental artefact. Nevertheless, the temperature ranges where Bi-2212 melts and resolidifies are expected to be reliable.

Phase identification and evolution of phases during the Bi-2212 melt state

During the molten state of Bi-2212 above 875 °C, three significant peaks appear at $Q = 2.047$, 2.078 and 2.108 \AA^{-1} with a high and broad background in the range of $Q = 1.8$ to 2.4 \AA^{-1} surrounding them (see Figure 58). The intensity of the three peaks could not be separated clearly, thus they could only be measured as a sum of all three. The peak positions are very similar to the most intense peaks appearing during the air HT of multifilament samples when Bi-2212 is molten. The initial sudden intensity rise is followed by constantly decreasing intensity with increasing temperature up to 890 °C and the following isothermal period. During the cool-down period, the intensity slightly decreases further. Below 865 °C the peaks vanish and only the high background remains. The background intensity in the range of $Q = 1.8$ to 2.4 \AA^{-1} vanishes continuously with the formation of Bi-2212 peaks. The high background is an indication of either a liquid or a phase with short range order, but lack of long range order. This could not be clarified yet.

The Bi-2212 peak intensity ratios before and after melting remain similar, indicating that there are no strong texture changes as compared to the as-drawn state. This is in contrast to the multifilament HT, where the texture in the wire filaments change strongly as seen by changes in the peak intensity ratios.

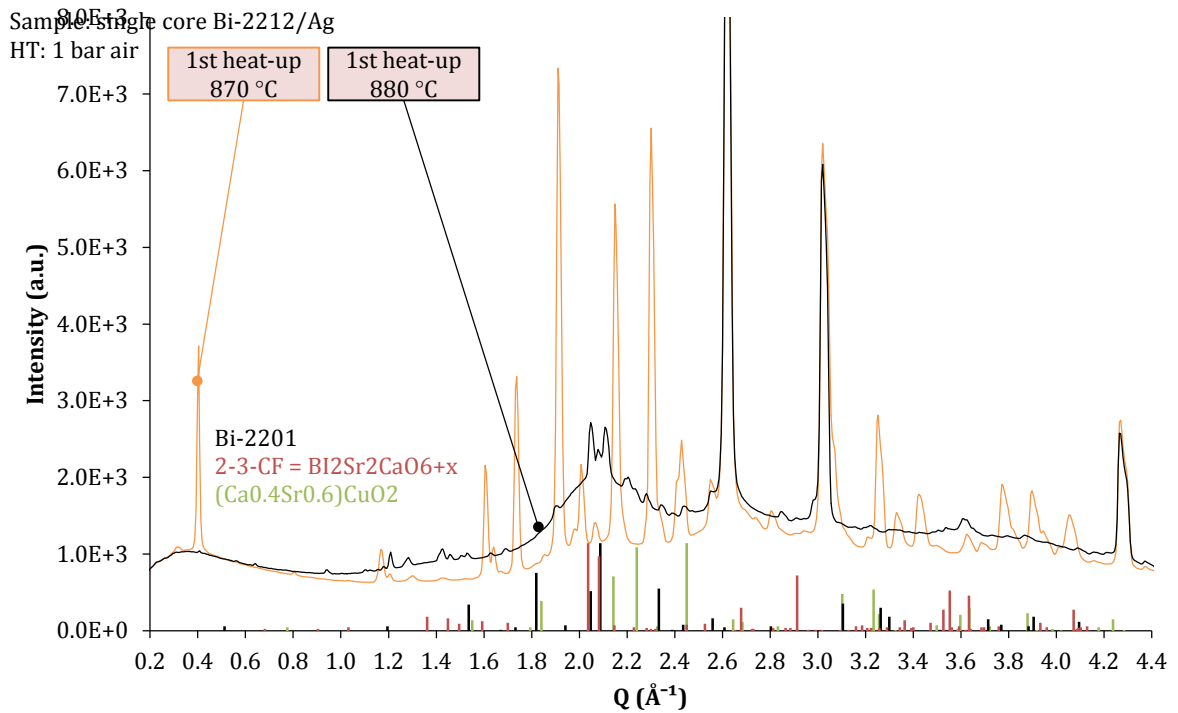


Figure 58 | XRD pattern of the Bi-2212/Ag single core wire during 1 bar air HT at 870 °C and 880 °C during the heat-up period.

Bi-2201 phase evolution

During the cool-down period further peaks appear that seem to characterise a new phase. In Figure 59 a comparison of the XRD patterns during heat-up at 870 °C and during cool-down at 590 °C is presented. In addition the diffraction peaks of Bi-2201 from PDF reference #46-0041 are inset. The peaks of Bi-2201 seem to explain the peaks that are present additionally to Bi-2212. Figure 60 presents the formation (at approximately 830 °C) of four characteristic Bi-2201 peaks as a function of temperature. The formation of the peak at $Q = 2.065 \text{ \AA}^{-1}$ at already 860 °C might result of a superimposition with another phase.

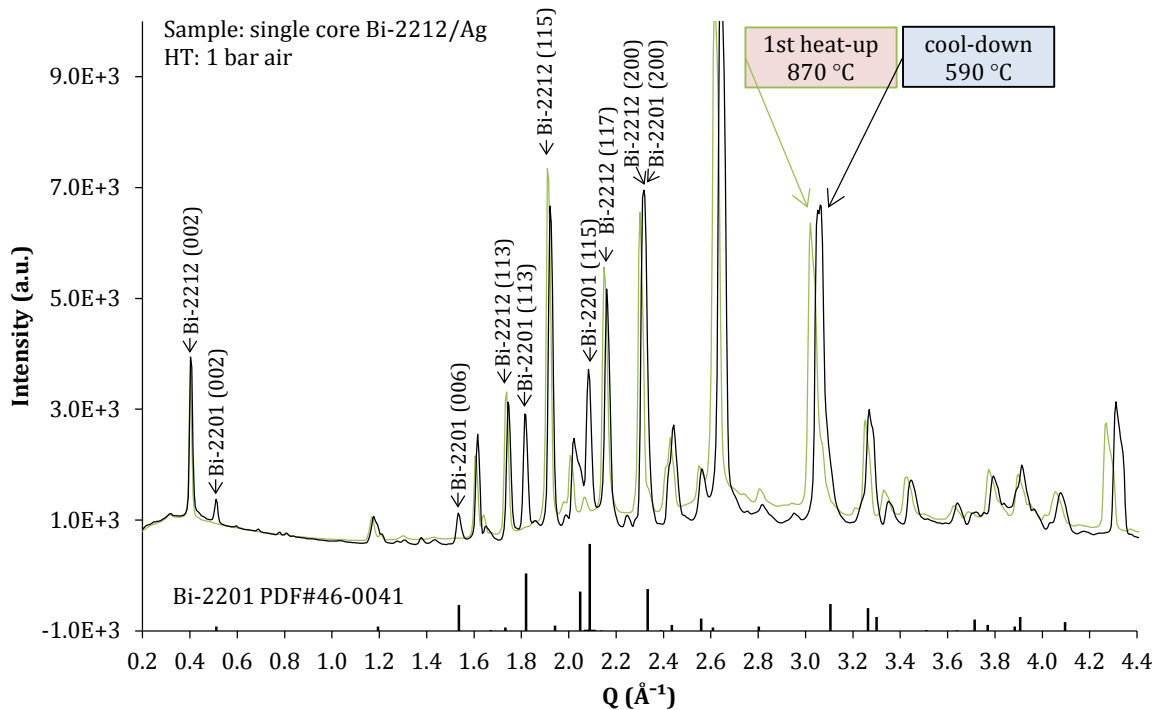


Figure 59 | XRD pattern of the Bi-2212/Ag single core wire during 1 bar air HT at 870 °C during the heat-up and 590 °C during the cool-down period.

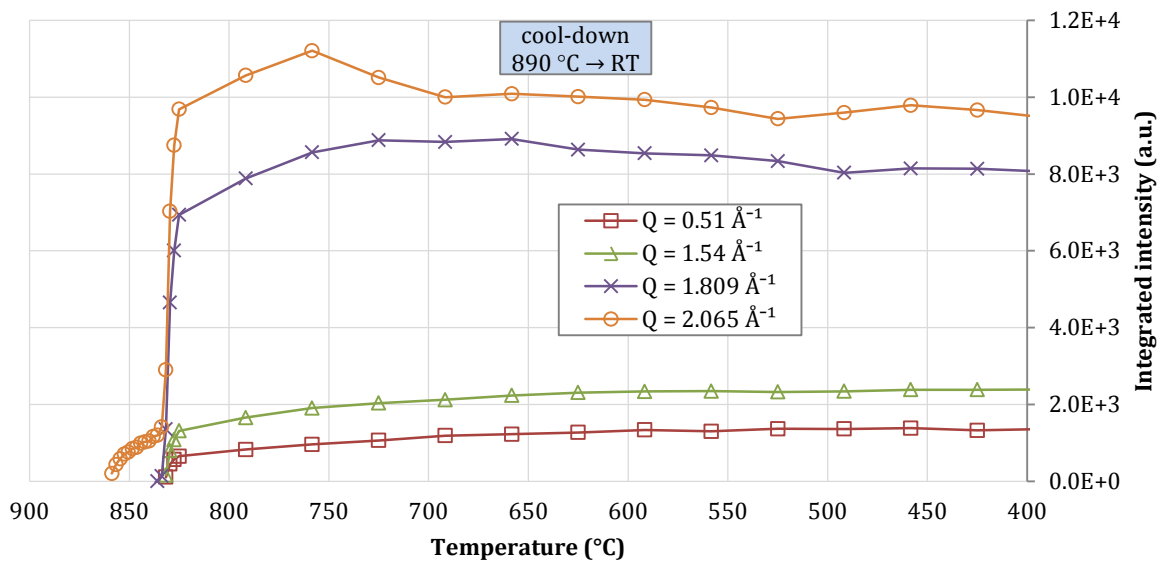


Figure 60 | Integrated intensity evolution of selected Bi-2201 peaks as a function of temperature. Sample: $\varnothing = 1$ mm single core Bi-2212/Ag wire. HT: 1 bar air.

4.8.2. Tomographic analysis of the Bi-2212 core

Simultaneously to the XRD recordings, the experiment allowed to record 3-dimensional absorption tomography images. The tomograms were taken just a minute after the diffraction images. In Figure 61 the most significant tomographic cross sections of the Bi-2212/Ag single core wire during the 1 bar air HT are presented. The core of the wire has a diameter of 0.65 mm.

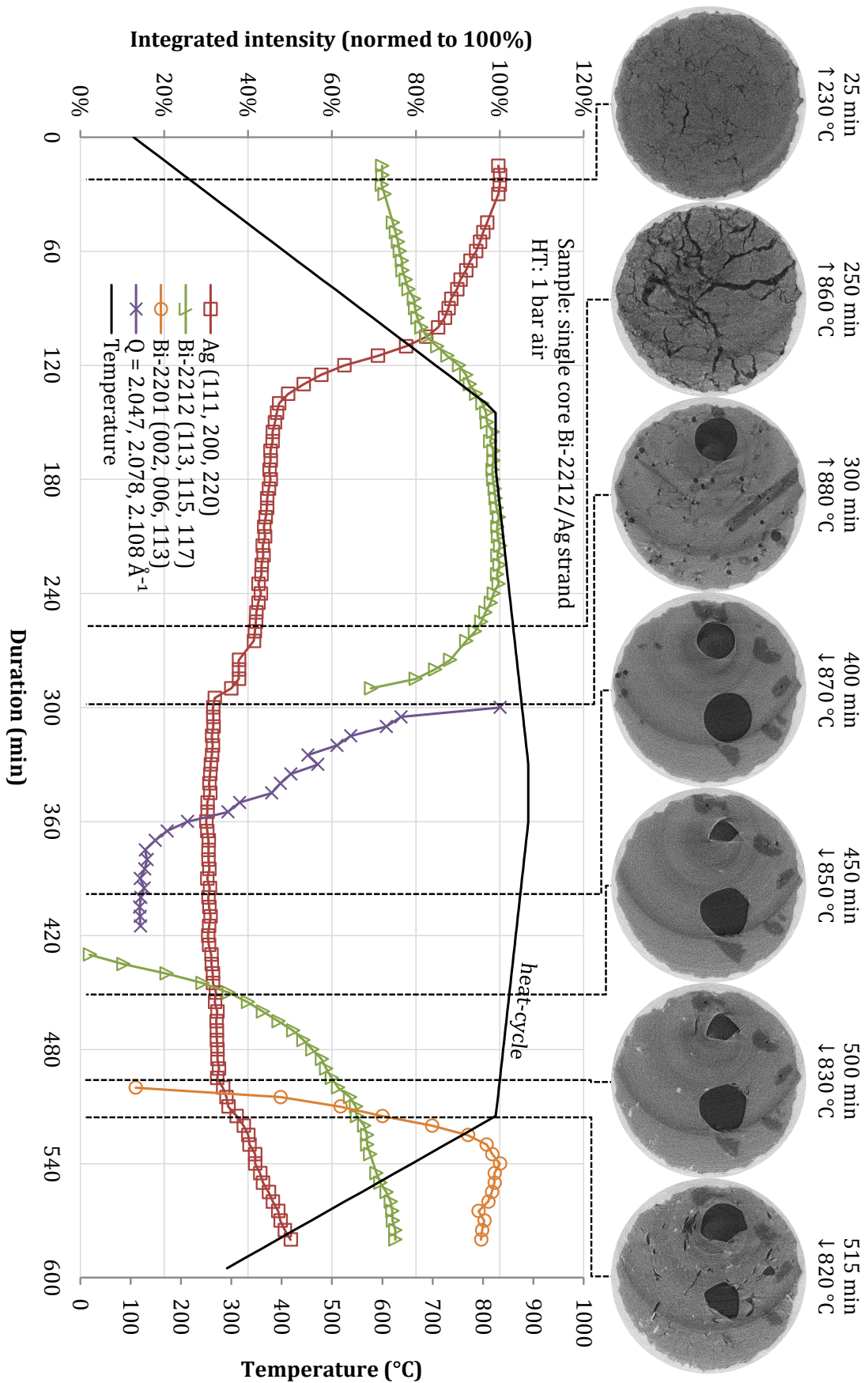
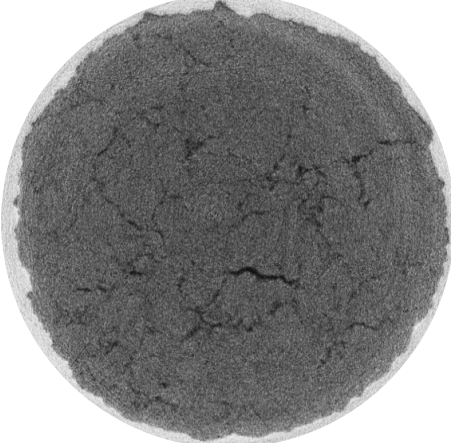
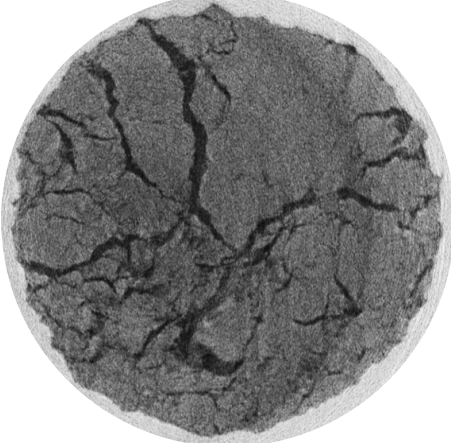
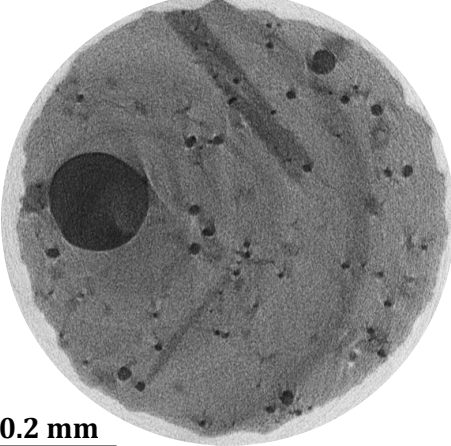
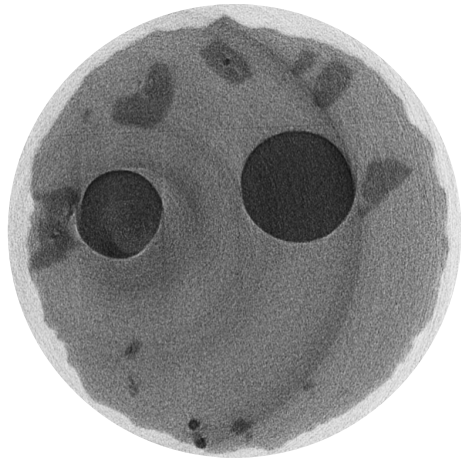


Figure 61 | Selected tomographic cross sections of the $\varnothing = 1$ mm single core Bi-2212/Ag wire acquired during the 1 bar air HT. The related lines indicate the duration and corresponding peak intensities in the diffraction patterns.

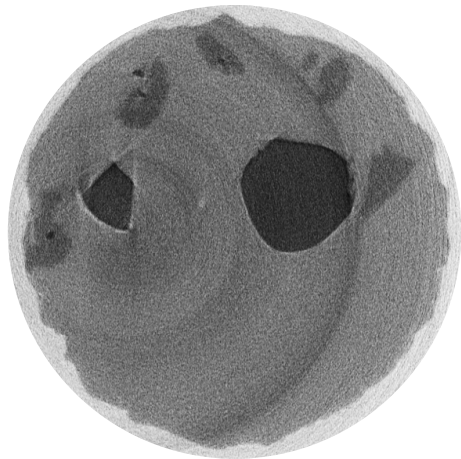
Below the individual tomograms are described. Dark areas indicate very weakly absorbing sample volume (void space). The bright area represents Ag, which is the most absorbing material is the sample (see Figure 17, attenuation coefficients). Bi-2212 and Bi-2201 cannot be distinguished from the absorption contrast.

Tomographic cross section	Description
	<p>↑ 230 °C, 25 min</p> <p>At 230 °C the Bi-2212 powder filling still shows the as-received state with a particle size smaller than the spatial resolution of the μ-CT experiment. Thus, the particles are not distinguishable from the intermediate voids space. Some large pores can be distinguished from the powder.</p>
	<p>↑ 860 °C, 250 min</p> <p>At 860 °C where the diffraction intensity of the Bi-2212 phase is at its highest point. Here the Bi-2212 phase shows a slightly lighter grey value that implies a higher density. The large elongated voids have grown significantly.</p>
	<p>↑ 880 °C, 300 min</p> <p>At 880 °C right after Bi-2212 is molten a large ($\varnothing \approx 0.1$ mm) and multiple small ($\varnothing \approx 0.01$ mm) spherical voids are visible in this cross section. Additionally a longish phase is visible with less absorption that might be a single crystal grown out of the liquid phase. This may be associated with the phase observed in the diffraction pattern measurements at $Q = 2.047, 2.078$ and 2.108 \AA^{-1}.</p>

0.2 mm

**↓ 870 °C, 400 min**

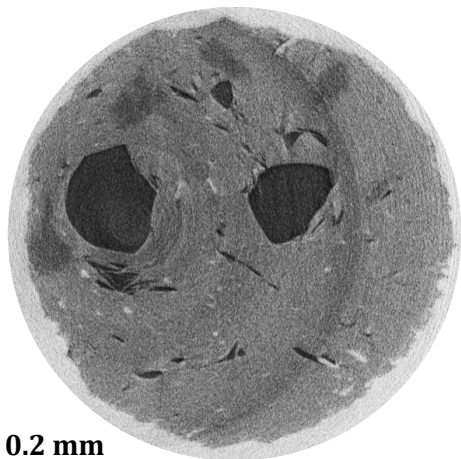
After an hour of melt-state of Bi-2212, at 870 °C the small voids are vanished but more large voids are visible now. From the absorption contrast it can be seen that apart from voids at least two phases are present inside the Ag sheath.

**↓ 850 °C, 450 min**

The tomographic cross section acquired at 850 °C during the cool-down phase shows still at least two phases. The initially spherical voids are now slightly deformed.

**↓ 830 °C, 500 min**

Beginning at 830 °C multiple small ($\varnothing \approx 0.01$ mm) highly absorbing particles appear in random distribution. According to their grey value, they are presumably associated with Ag that precipitates out of the melt.

**↓ 820 °C, 515 min**

With further cooling, as presented in the tomogram acquired at 820 °C, small ($\varnothing \approx 0.01$ mm) irregularly and longish shaped voids appear in the Bi-2212 phase. Which might be formed as a result of different contraction coefficients of the different phases.

0.2 mm

A summary of grey value histograms obtained from the tomograms is presented in Figure 62. Four distinct peaks can be distinguished, which are attributed to Ag, Bi-2212, another phase which is less absorbing than Bi-2212, and void space.

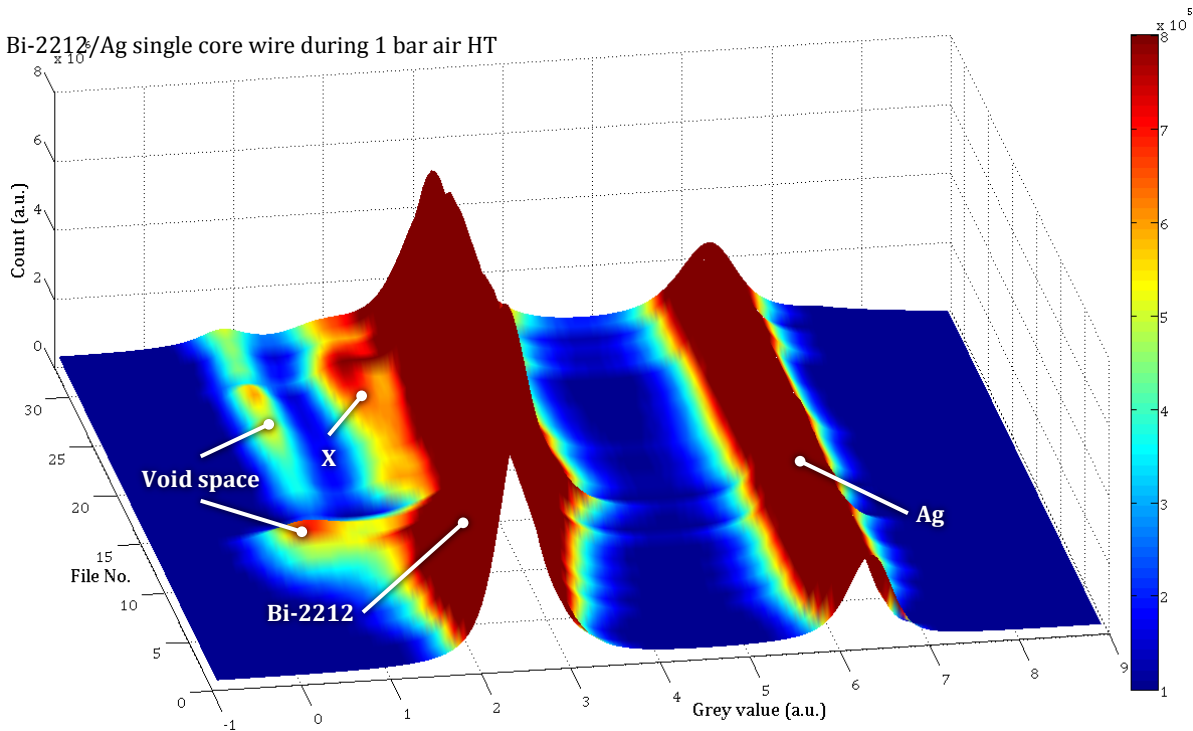


Figure 62 | Summary of grey value counts acquired with μ -CT during 1 bar air HT of the Bi-2212/Ag single core wire. The inset shows the corresponding heat cycle.

In Figure 63 the evolution of these four peak maxima that was fitted with the Gaussian function is shown as a function of HT duration. It shows, that the grey values that were identified to belong to Ag stay almost constant during the HT only slightly influenced by a lowered density at high temperature due to thermal expansion.

The lowest grey value represents the voids during the HT. They are first distinguishable during the melt of Bi-2212 when large spherical voids are forming.

The grey value of Bi-2212 is initially a superposition of the Bi-2212 powder and the void space between the particles smaller than the spatial resolution of the μ -CT. Above 830 °C the Bi-2212 density increases and simultaneously voids are distinguishable in the tomograms.

Initiating the melt of Bi-2212 a further phase appears with a lower grey value. This might be due to a lower density or another atomic composition than Bi-2212.

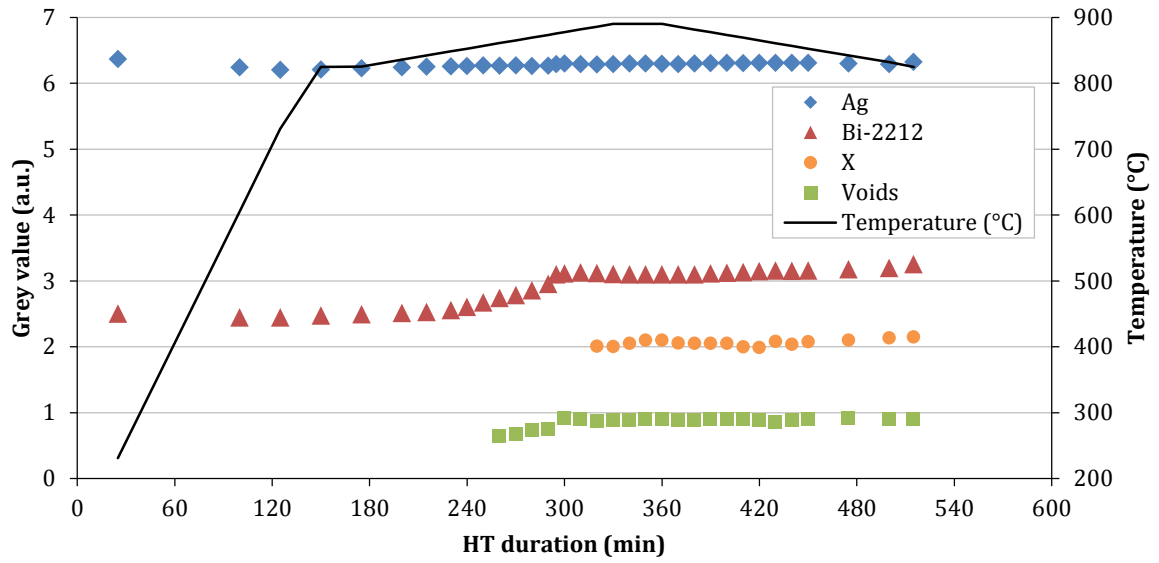


Figure 63 | Evolution of Bi-2212 and Ag grey value acquired with μ -CT during 1 bar air HT of the Bi-2212/Ag single core wire.

5. Influence of process route and filament size on the Nb₃Sn growth in multifilament wires

The processing of PIT and RRP type Nb₃Sn/Cu wires was studied *in situ* at ESRF beam line ID15 by high energy X-ray diffraction. The RRP wire results had been analysed and reported previously [45]. Particular care was taken to minimise instrumental peak broadening (see LaB₆ (210) peak in Figure 11).

With main focus on the superconduction Nb₃Sn phase, the evolution of intensity, position and width of the Nb₃Sn diffraction peaks are presented in the following chapters to get information on Nb₃Sn phase growth, Sn content and grain size. Identical instrumental setting for all XRD recordings allow a direct comparison of the results. Absolute peak intensities of the different wire samples are influenced by diffraction volume and X-ray attenuation in the sample with changing material composition and wire geometry. Therefore Nb₃Sn diffraction peak intensities have been normalised to the maximum peak area.

For the RRP wire it was possible to estimate the crystallite size and Sn content evolution during the processing. About 20 diffractograms have been analysed in the reference work after deconvolution from the instrument function. The RRP wire had been selected because it contains a very homogeneous Nb₃Sn grain size and Sn content distribution, unlike the PIT wire, which contains grains with strongly different size and Sn content (see Figure 7).

With the semi-automatic peak fitting and tracking method, that was developed during this thesis, more patterns could be analysed, and the RRP wire results could be compared with the PIT wire results (see Figure 64 and Figure 65). A deconvolution of the instrument function has not been attempted here. A comparison of the three wires (PIT $\varnothing = 0.80$ mm, PIT $\varnothing = 1.25$ mm and RRP $\varnothing = 0.80$ mm) is presented below to see the influence of process route and filament diameter on the Nb₃Sn formation kinetics and Sn uptake.

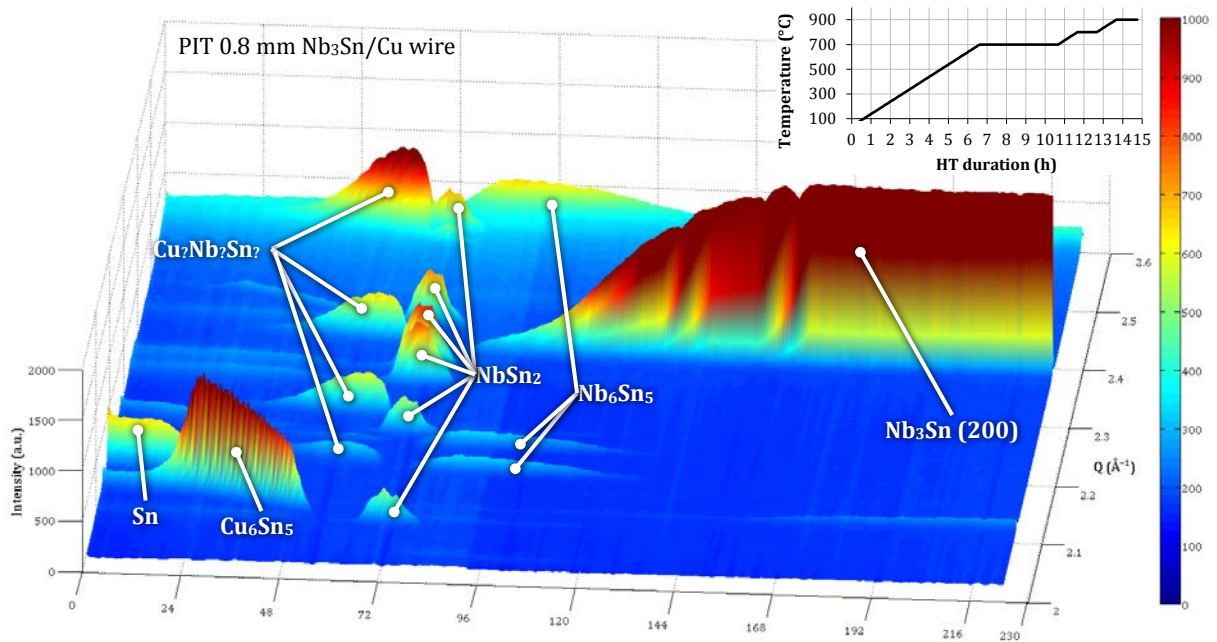


Figure 64 | Summary of diffraction patterns acquired during 1 bar air HT of the $\varnothing = 0.8$ mm PIT Nb₃Sn/Cu wire. The inset shows the corresponding heat cycle.

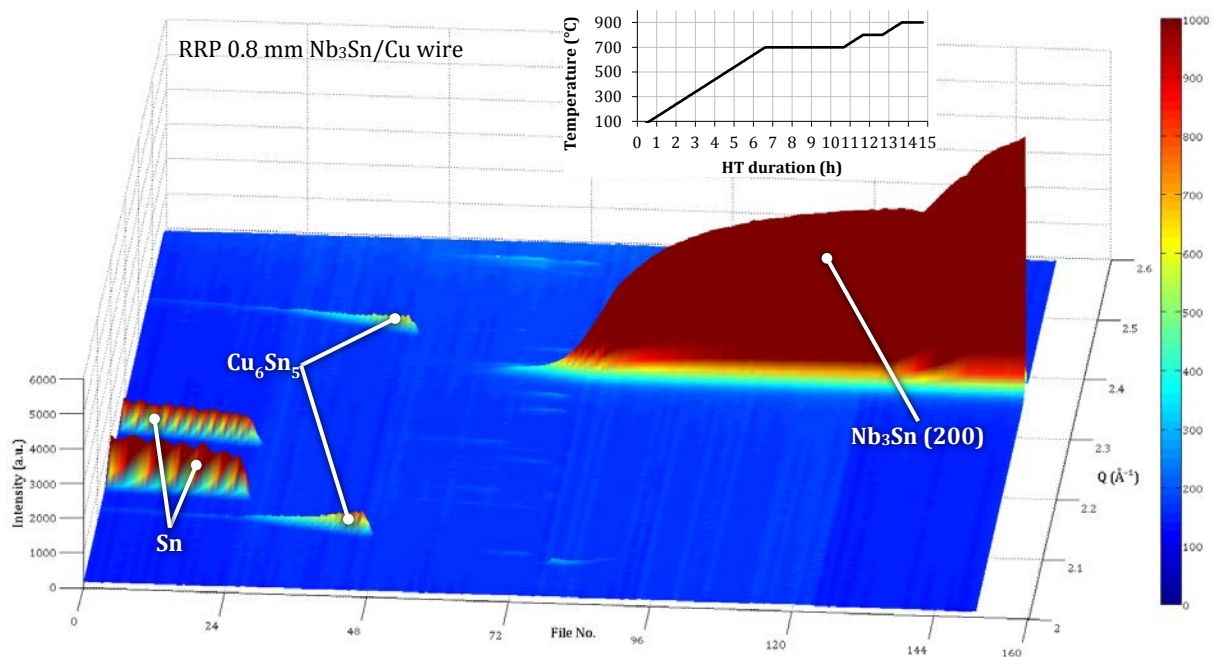


Figure 65 | Summary of diffraction patterns acquired during 1 bar air HT of the $\varnothing = 0.8$ mm RRP Nb₃Sn/Cu wire. The inset shows the corresponding heat cycle.

It is obvious from the comparison of PIT and RRP diffraction patterns that less NbSn₂ and Nb₆Sn is formed during the processing of the RRP wire [20].

Choice of diffraction peaks to analyse

To analyse the peak intensity of the Nb₃Sn and Nb phase the diffraction patterns were first analysed for peak superposition that might influence the results. The diffraction pattern of the PIT $\varnothing = 0.8$ mm sample at 900 °C during HT is presented in Figure 66 to show the available

peaks in the recorded range of $Q = 1.8$ to 5.1 \AA^{-1} . For intensity analyses of the Nb_3Sn phase the reflections (200), (210), (320) and (321) were chosen as presented in the diffraction pattern of the PIT $\varnothing = 0.8 \text{ mm}$ sample at $900 \text{ }^\circ\text{C}$ after full HT of 15 h in Figure 66. The peaks of the selected reflections show none or only simple peak superposition where the peaks are distinguishable with a double peak fit.

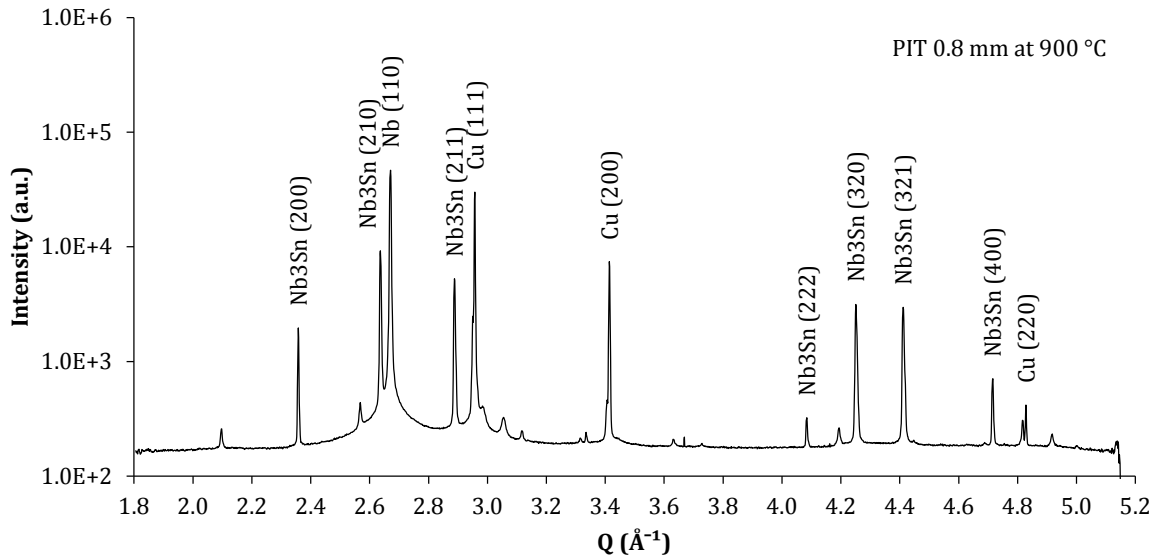


Figure 66 | X-ray diffraction pattern of the Nb_3Sn PIT $\varnothing = 0.8 \text{ mm}$ wire acquired during the HT at $900 \text{ }^\circ\text{C}$. Intensity in logarithmic scale is shown as a function of Q .

More detailed peak position and peak shape analysis was done with the reflections Nb_3Sn (200) and Nb_3Sn (320). These two peaks have been chosen because they are distributed far from each other in the diffraction pattern. They cross the cubic Nb_3Sn unit cell in two directions: parallel to the unit cell boundaries (200) and almost diagonally (320).

5.1. Evolution of the Nb_3Sn and Nb diffraction peak areas

The growth of the Nb_3Sn phase is revealed by the increase of diffraction peak areas. The evolution of the Nb_3Sn diffraction peak areas as a function of HT temperature and duration is compared in Figure 67 for the three wires. It is assumed that during the *in situ* HT up to $900 \text{ }^\circ\text{C}$ the maximum possible amount of Nb_3Sn is reached in the wires, thus peak areas are normalised to their maxima in order to compare the Nb_3Sn growth kinetics in the different wires, which have different composition and geometry.

In both PIT wires ($\varnothing = 0.80 \text{ mm}$ and $\varnothing = 1.25 \text{ mm}$) the Nb_3Sn phase is first detected during the $700 \text{ }^\circ\text{C}$ isothermal period. The delay of about one hour for observing an initial peak intensity in the $\varnothing = 1.25 \text{ mm}$ PIT wire might result from the smaller peak intensity to background scatter ratio that is caused by the higher X-ray attenuation due to larger wire diameter. The PIT $\varnothing = 0.8 \text{ mm}$ wire shows an almost constant increase of its intensity up to a temperature of $800 \text{ }^\circ\text{C}$. With further increasing temperature up to $900 \text{ }^\circ\text{C}$ the Nb_3Sn diffraction intensity in the PIT $\varnothing = 0.8 \text{ mm}$ wire reaches a maximum. A longer lasting record of the PIT 1.25 wire including the cool-

down period shows that Nb₃Sn diffraction peak intensity in the PIT 1.25 wire has not reached its maximal at this time.

In the RRP $\varnothing = 0.8$ mm wire the Nb₃Sn phase already starts to grow during the initial heat-ramp (100°C/h for all samples) at approximately 600 °C. After a strong initial increase of diffraction intensity while reaching the 700 °C isothermal period, the phase formation slows down. Reaching a temperature of 900 °C the amount of Nb₃Sn decreases again.

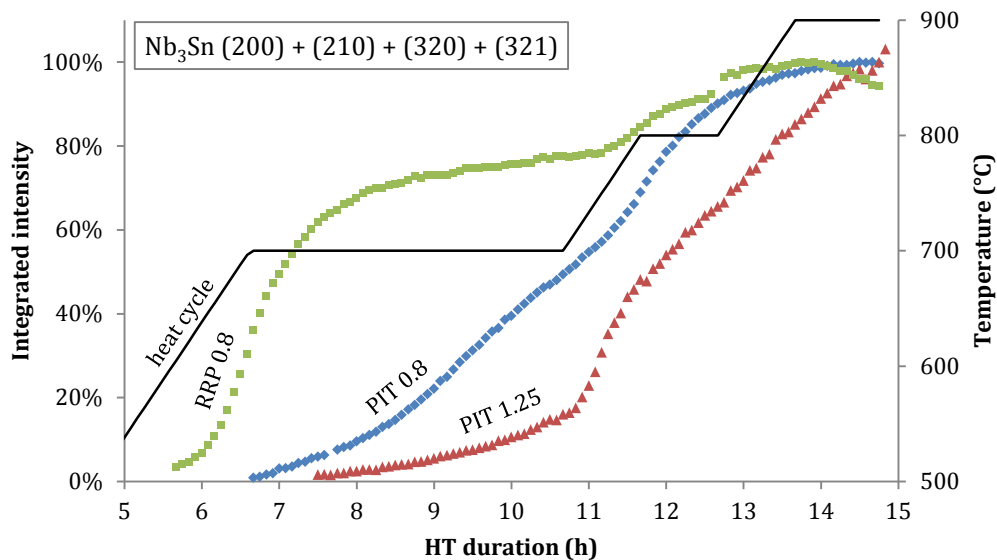


Figure 67 | Nb₃Sn phase evolution by summing up the intensities of the peaks Nb₃Sn(200), (210), (320) and (321). The maximum value of each wire (PIT $\varnothing = 0.8$ mm, PIT $\varnothing = 1.25$ mm and RRP $\varnothing = 0.8$ mm) is set to 100 % for better comparability.

A comparison of the Nb₃Sn and Nb phase intensity evolution shows a good analogy of increasing Nb₃Sn and simultaneous decrease of Nb due to solid state diffusion of Sn into Nb. The decrease of the pure Nb phase is shown in Figure 68 as a function of temperature and HT duration. But the data has to be read with care because only a single peak has been recorded and Nb has a strong texture due to wire drawing that influence the intensity ratios between the reflections. Below 700 °C the Nb (110) peak shows a strong broadening (FWHM $\approx 0.02 - 0.03 \text{ \AA}^{-1}$) and asymmetry that might result from crystallite size and anisotropic strain caused by the wire drawing previous to the HT.

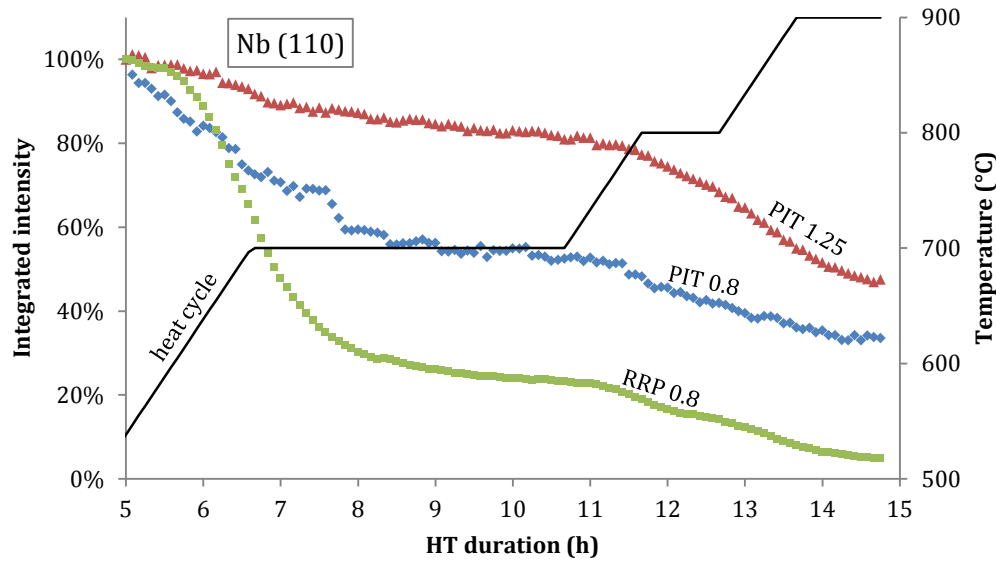


Figure 68 | Integrated intensity evolution of the Nb (110) peak in PIT $\varnothing = 0.8$ mm, PIT $\varnothing = 1.25$ mm and RRP $\varnothing = 0.8$ mm wire samples. Intensities are set to 100 % at 5 h HT duration.

5.2. Nb₃Sn lattice parameter evolution

Nb₃Sn is stable with a Sn content in the range from 18-25 at.% [46]. Since the Nb₃Sn lattice parameter increases with increasing Sn content from about 5.282 to 5.290 Å at RT [47], the Nb₃Sn lattice parameter evolution during the HT is influenced by thermal expansion, as well as by the Sn content.

To analyse the Sn uptake in the Nb₃Sn phase during the HT, the d-spacing of the Nb₃Sn peaks is monitored. Especially during the isothermal periods of 700, 800 and 900 °C a lattice parameter growth can be observed without influence of thermal expansion. To be able to compare the changes during the temperature ramps, a theoretical thermal expansion of Nb₃Sn with static Sn content of 25 at.% has been calculated [48].

Prior to the peak position and peak width analysis an observation of Nb₃Sn peaks shape asymmetry is to be mentioned. While in the diffraction patterns of the RRP wires the peaks are nearly symmetric, the diffraction patterns of the PIT wires show a comparatively strong asymmetry. As an example, the Nb₃Sn (320) peak of the $\varnothing = 0.8$ mm PIT wire acquired at the end of the 900 °C isothermal is shown in Figure 69. The peak asymmetry can influence the d-spacing measurement, causing a maximal lattice parameter uncertainty of about 0.001 Å. The fitting uncertainty, remains for all peaks between 5 % < R_p < 10 %.

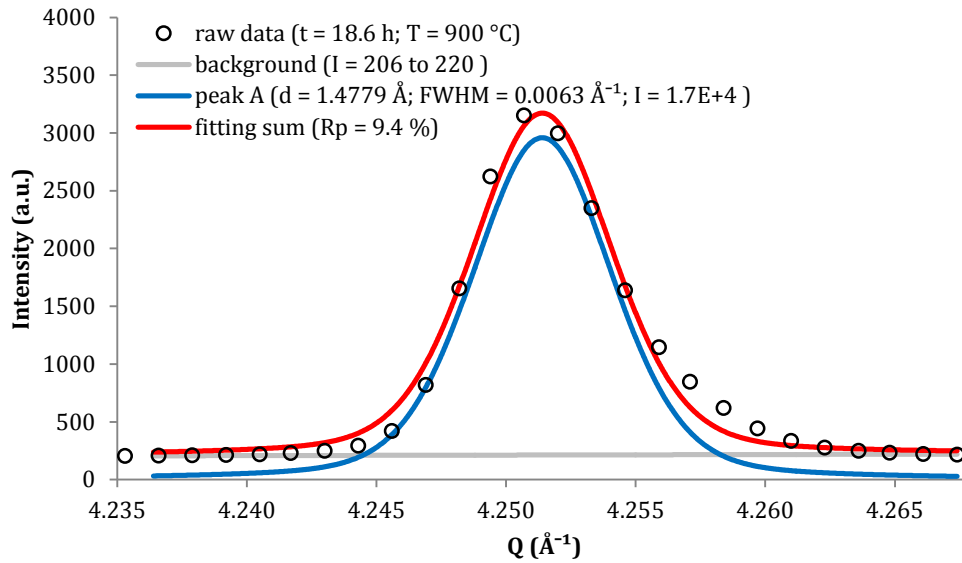


Figure 69 | Symmetrical pseudo-Voigt fitting of the Nb₃Sn (320) peak in the PIT $\varnothing = 0.8$ mm wire acquired during the 900 °C HT.

The lattice parameter evolution calculated from the Nb₃Sn (200) and Nb₃Sn (320) d-spacing is shown in Figure 70 and Figure 71, respectively. The lattice parameter calculated from the Nb₃Sn (320) d-spacing shows only marginal differences to the values determined with the Nb₃Sn (200) peak.

The strong initial the lattice parameter increases cannot be solely explained by thermal expansion and thus indicates an increase of Sn content in the Nb₃Sn phase. The results presented in Figure 70 and Figure 71 might indicate that the Nb₃Sn in PIT wires contains in average more Sn than in the RRP wire. However, the difference between average Sn content in PIT and RRP may also be explained by the presence of a relatively large amount of coarse Nb₃Sn grains with stoichiometric composition in the PIT wire (see Figure 7) [16].

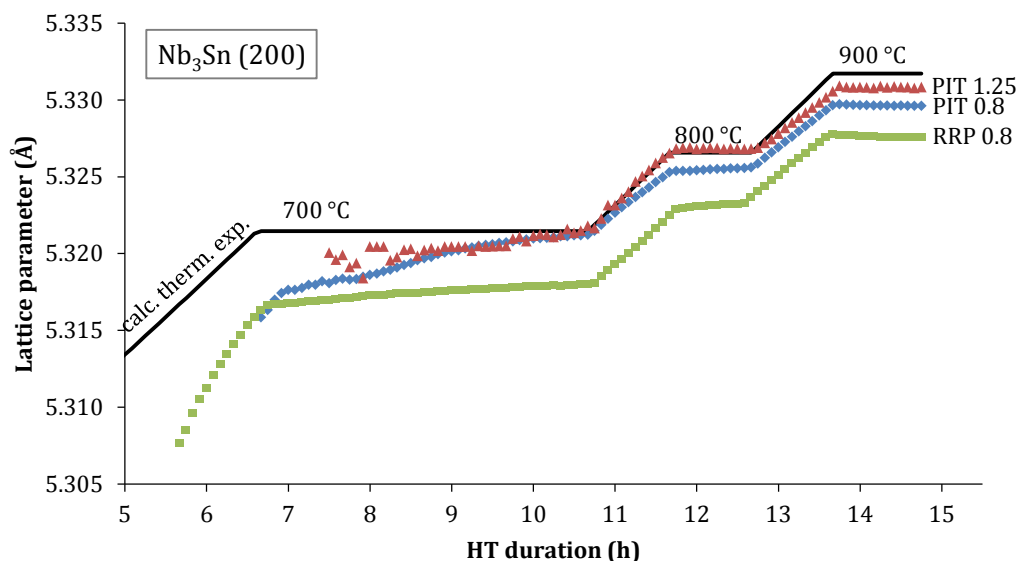


Figure 70 | Lattice parameter evolution of Nb₃Sn (200) in PIT $\varnothing = 0.8$ mm and RRP $\varnothing = 0.8$ mm wires. For comparison the calculated lattice parameter variation caused by thermal expansion [48] is shown for stoichiometric Nb₃Sn [47].

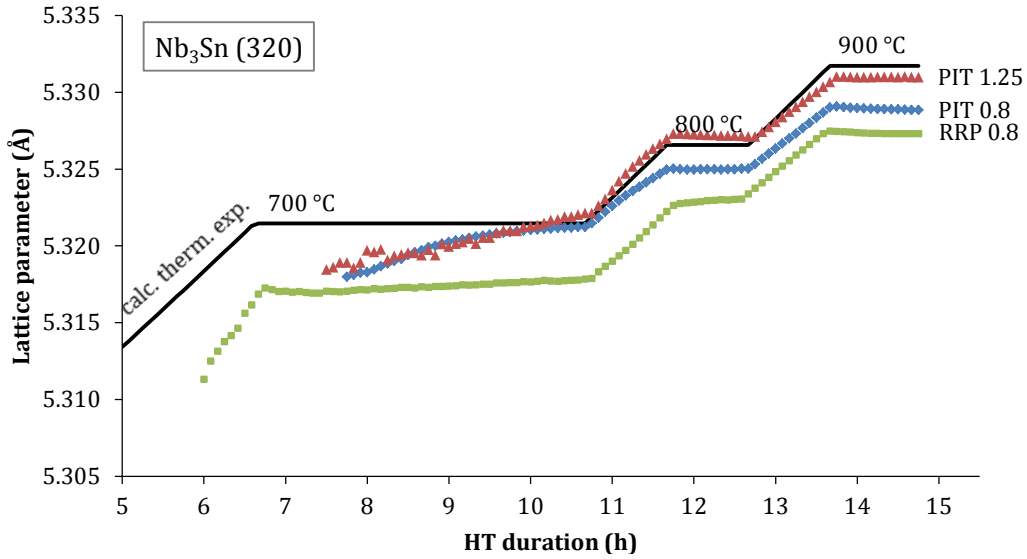


Figure 71 | Lattice parameter evolution of Nb_3Sn (320) in PIT $\varnothing = 0.8$ mm and RRP $\varnothing = 0.8$ mm wires. For comparison the calculated lattice parameter variation caused by thermal expansion [48] is shown for stoichiometric Nb_3Sn [47].

5.3. Nb_3Sn diffraction peak width

The width of diffraction peaks is influenced by crystallite size and non-uniform stress but can also be influenced by slight variance in the unit cells lattice parameter influenced by varying Sn content in Nb_3Sn lattice.

The evolution of peak width of the diffraction peaks Nb_3Sn (200) and Nb_3Sn (320) is presented in Figure 72 and Figure 73 respectively.

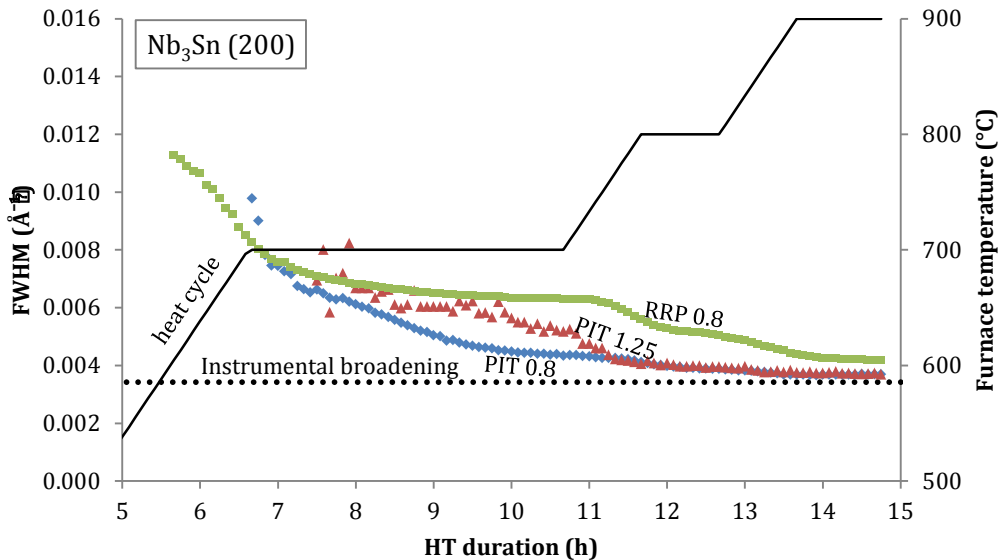


Figure 72 | Peak width (FWHM) evolution of Nb_3Sn (200) in PIT $\varnothing = 0.8$ mm and RRP $\varnothing = 0.8$ mm wires. The instrument induced broadening is indicated by the width of the closest LaB_6 peak (110) at $d = 2.94$ Å.

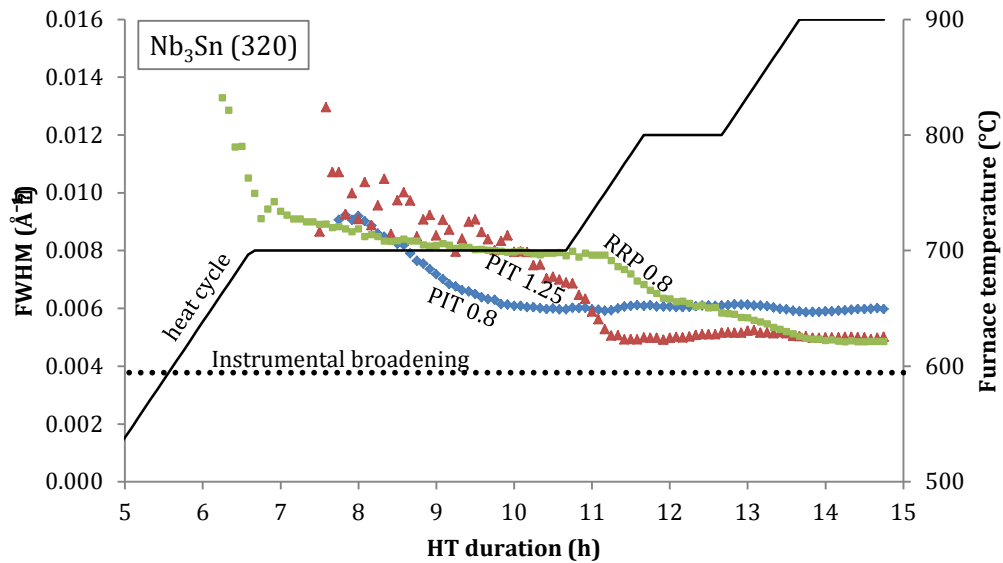


Figure 73 | Peak width (FWHM) evolution of Nb₃Sn (320) in PIT $\phi = 0.8$ mm and RRP $\phi = 0.8$ mm wires. The instrument induced broadening is indicated by the width of the closest LaB₆ peak (211) at $d = 1.47$ Å.

5.4. Asymmetry of Nb₃Sn diffraction peaks

As mentioned above, a slight asymmetry of Nb₃Sn diffraction peaks was observed in the diffraction patterns. The highest asymmetry is present in the Nb₃Sn (320) peak of the PIT $\phi = 0.8$ mm wire at 900 °C during the HT. A fit with two superimposed pseudo-Voigt functions is presented in Figure 74. Compared to the single peak fit ($R_p = 9.4$ %) presented in Figure 69, the double-peak fit ($R_p = 1.6$ %) has a better accordance to the measured data. The relative d-spacing difference of the two fitted curves is the same as it would be for the lattice parameter of Nb₃Sn with 25 wt.% and 22.8 wt.% of Sn [47].

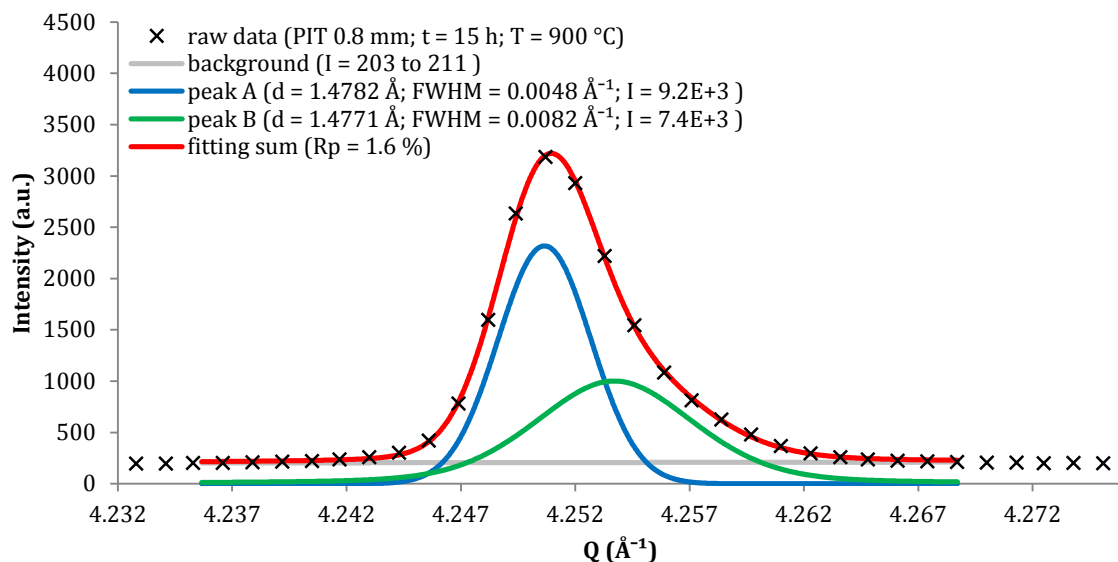


Figure 74 | Asymmetry of the Nb₃Sn (320) diffraction peak during HT at 900 °C of the PIT $\phi = 0.8$ mm wire. Fitting was done with two pseudo-Voigt functions after background subtraction.

6. Discussion

The participation in the experiment MA-1475 in June at ESRF, Grenoble showed the complexity of *in situ* XRD and μ -CT experiments performed at a state of the art synchrotron beam line. Discussions with the beam line scientists were helpful to understand the possibilities and limitations of the instruments in use. The single core Bi-2212/Ag wire experiment including XRD and μ -CT measurements that was performed during the MA-1475 experiment is representative to understand the other experiment data, which were recorded in advance of this work by C. Scheuerlein, M. Di Michiel and J. Andrieux and have been analysed in this thesis.

The use of a synchrotron X-ray source instead of a laboratory X-ray tube allows to select the photon energy from a continuous spectrum. Only with the high photon energies provided through high energy beam lines like ID15 of ESRF, XRD experiments could be performed in transmission geometry during *in situ* HTs. The large amount of XRD data recorded during the synchrotron experiments required an efficient and reliable analysis that could be provided by the here developed "PeakFitAndTrack.xlsm" program based on Excel-VBA. This program allows a fast fit and track of selected diffraction peaks during the whole HT after an initial set of approximate values and boundaries.

Thanks to the very high photon flux at ID15, tomograms can be acquired within one minute, which is much faster than the acquisition of tomograms with a laboratory X-ray tube, which typically lasts several hours. The fast tomography at ID15 enables time resolved studies in four dimensions: three space dimensions and time. With the knowledge of attenuation coefficients and phase density the evolution of filament powder packing, melting and solidifying could be monitored. A locating of secondary phases with different attenuation was possible as well. Depending on the selected X-ray energy of the photon beam, individual materials in the sample can be highlighted. The grain size of the Bi-2212 powder filling could, as expected, not be measured because the spatial resolution of the acquired tomograms is not detailed enough to resolve the particle size.

In the following paragraphs the XRD and μ -CT results are discussed. The influence of partial pressure on the phase evolution in Bi-2212/Ag wires is presented as a comparison of results acquired during the wire processing in 1 bar inert gas, 1 bar air and 100 bar air. With the processing of a single core Bi-2212/Ag wires the influence of filament size to the phase development (e.g. stability and intensity ratios) is shown as well. During the same experiment μ -CT measurements allowed to estimate the void space between the grains of the Bi-2212 powder filling. The influence of process route and filament size on Nb₃Sn growth is discussed based on the XRD results acquired during processing in inert gas.

6.1. Influence of oxygen partial pressure on the phase evolution in Bi-2212/Ag wires

The XRD results presented in this thesis confirm the importance of the oxygen partial pressure on the Bi-2212 formation during the wire processing. The comparison of Bi-2212 diffraction peak intensity evolution during the 1 bar N₂ ($p_{O_2} = 0$ bar), 1 bar air ($p_{O_2} = 0.21$ bar) and 100 bar air ($p_{O_2} = 21$ bar) HTs is presented in Figure 75 as a function of temperature, for heat-up and cool-down periods.

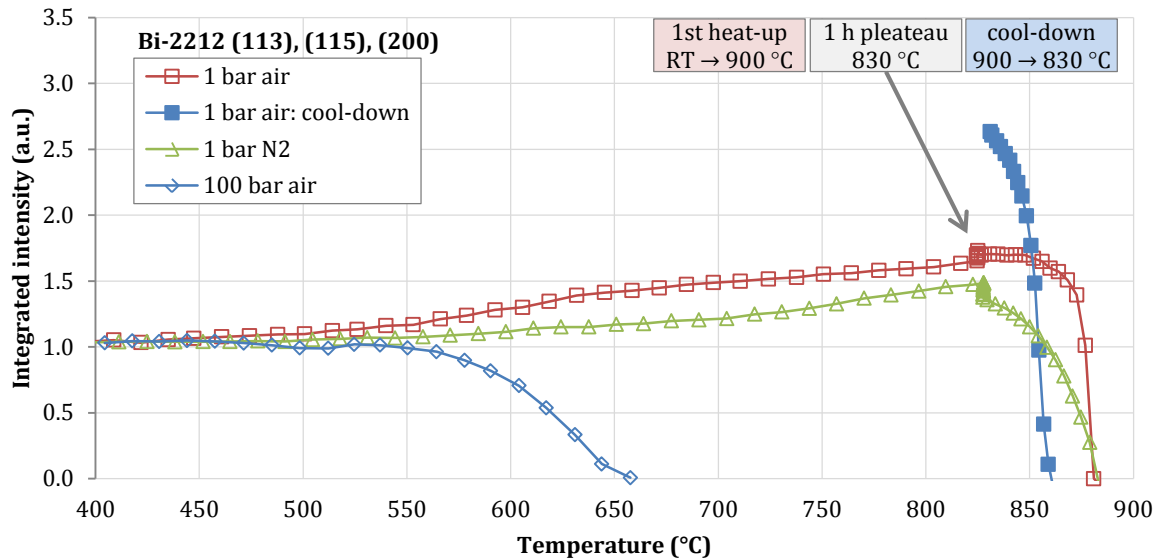


Figure 75 | Comparison of the Bi-2212 phase evolution during 1bar air, 1 bar N₂ and 100 bar air HT on identical $\phi = 1$ mm multifilament Bi-2212/Ag samples.

When the HT is performed without oxygen in the process gas, or when the oxygen partial pressure is too high, Bi-2212 cannot reform during cool-down from the melt state. In the present study only the HT in 1 bar air produces Bi-2212 at the end of the processing. A new finding of this thesis work is that Bi-2212 is not stable in 21 bar O₂ above 650 °C.

Until now a processing in 1 bar pure oxygen is assumed to produce Bi-2212/Ag wires with the highest critical current density [36]. Further XRD studies at variable pressure, as those described in this thesis, should help to optimise the oxygen partial pressure in order to further increase the critical current densities in Bi-2212/Ag wires.

6.2. Comparison of Bi-2212 phase evolution and crystallite orientation in multifilament and single core wires

The Bi-2212 phase evolution in a multifilament wire (with a filament size of $\phi = 15$ μm) and a single core wire (with a filament size of about $\phi = 650$ μm) has been compared. In both wires Bi-2212 is present in similar temperature intervals (see Figure 76). The small difference observed during warm up is likely influenced by the heating rate (50 °C/h vs. 25 °C/h) (see also Figure 35).

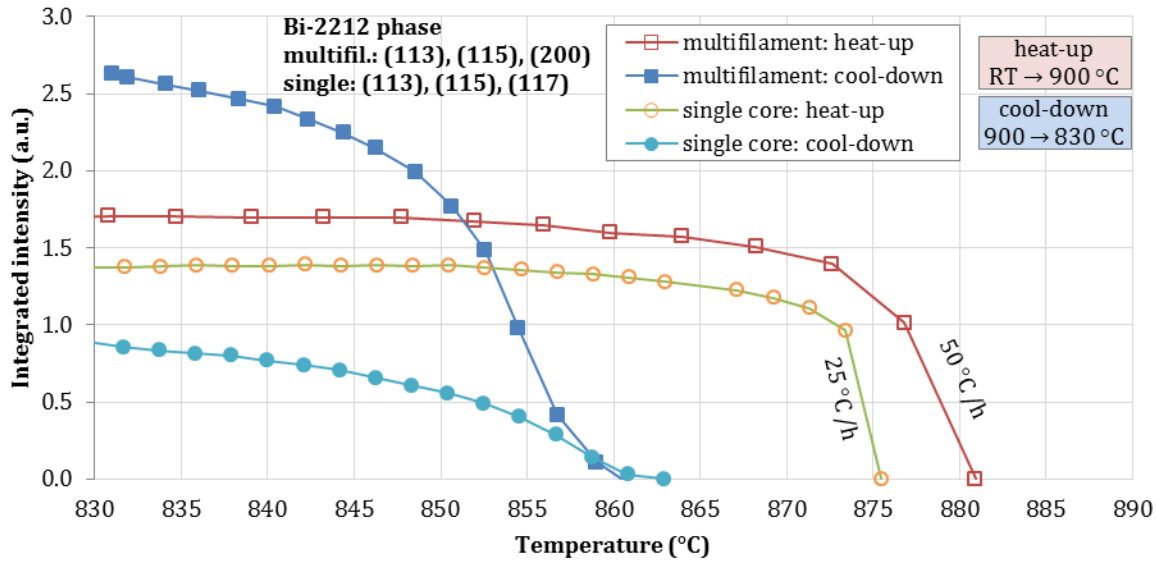


Figure 76 | Comparison of the Bi-2212 phase evolution during 1 bar air HT of a multifilament wire and a single core wire with larger filament diameter.

The comparison of Bi-2212 peak intensity ratios can be used to detect differences in preferential crystallite orientations. In Table 8 relative Bi-2212 diffraction peak intensity ratios in powder and granulate samples (with assumed random crystallite orientation) are compared with the relative intensities measured in the multifilament wire before processing, in air processed multifilament and single core wire, and in a multifilament wire fully processed in 1 bar pure O₂.

The Bi-2212 peak intensity ratios obtained for the multifilament wire before HT and the processed single core wire are similar to those of the powder and granulate, indicating a nearly random crystallite distribution in these wires. However, the significantly stronger Bi-2212 (200) peak intensity with respect to the intensity of the other peaks, indicates a clear Bi-2212 texturing in both processed multifilament wires.

Table 8 | Relative Bi-2212 peak intensities of the Bi-2212/Ag wire after 1 bar O₂ HT, a green Bi-2212/Ag wire and the Bi-2212 granulate. (“n.m.” = “not measured” due to peak superposition)

Bi-2212 reflections	Bi-2212 reference [13]	Bi-2212 granulate	multifil. wire before HT	multifil. wire 1 bar O ₂	multifil. wire 1 bar air	single core wire 1 bar air
(200):(113)	2.9	2.5	3.1	8.3	7.7	3.4
(200):(115)	1.1	0.8	1.3	3.6	2.9	1.4
(200):(117)	1.5	1.0	n.m.	5.3	4.0	1.8

With the present XRD data sets a full texture analysis is not possible, but could be obtained in future synchrotron XRD experiments.

6.3. Second phase formation during the Bi-2212/Ag wire processing

In comparison to reference powder diffraction patterns the identification of the main crystalline phases was possible. Some phases that are present in the partial melt state of the Bi-2212/Ag

wire were observed but could not be identified yet due to a lack of available reference diffraction patterns. Nevertheless a qualitative analysis of these phases was possible.

No phases apart from Bi-2212 and Ag have been detected in the as received precursor and wires. The phases which have been detected during processing in air when Bi-2212 in the wires melts, and also after resolidification of Bi-2212 during the cool-down, include Bi-2201 and $(\text{Ca}_{0.4}\text{Sr}_{0.6})\text{CuO}_2$. In addition at least one more phase is formed with approximate peak positions at $Q = 2.047, 2.078$ and 2.108 \AA^{-1} , which could not yet be identified.

When the HT is performed in inert gas, $\text{Bi}_2\text{Sr}_2\text{CaO}_{6+x}$ is formed upon Bi-2212 melting, and does not disappear during cool-down to $830 \text{ }^\circ\text{C}$ (see Figure 46).

Further interesting changes in the diffraction patterns are the strong background variations when Bi-2212 melts. Especially during the processing of the single core wire, a high background intensity in the approximate range of $Q = 1.8$ to 2.4 \AA^{-1} (see Figure 58) indicates the presence of a phase with short range order, but without long range order.

6.4. Crystallite size evolution during the Bi-2212/Ag wire processing

The aim of monitoring the Bi-2212 crystallite size in the sample has only been fulfilled partially. The orthorhombic crystal structure of Bi-2212 with almost identical lattice parameter “a” and “b” and a modulation of the crystal superstructure with periodically additional oxygen atoms results in many peak superposition in the diffraction pattern. Thus a clear measuring of peak broadening was only possible for a few peaks and is not sufficient for a satisfying fit of the Scherrer Equations. In order to better distinguish between crystallite size and anisotropic strain, diffraction patterns should be recorded over a greater angular range (see Figure 12).

6.5. Influence of process route and filament size on Nb_3Sn formation

The diffraction patterns acquired during identical HTs show that Nb_3Sn is forming earlier and that Nb_3Sn growth is faster in wires of RRP type as compared to PIT type wires. As expected, Nb_3Sn growth is faster in wires with smaller filament size, as the comparison between the PIT wires with a filament size of $50 \text{ }\mu\text{m}$ and $32 \text{ }\mu\text{m}$ shows (see Figure 67).

The lattice parameter evolution during the HT (see Figure 70) indicates that in RRP wires the Sn content increases faster than in PIT wires. Estimates of the Sn content in the Nb_3Sn phase of the PIT wires were not reliable because of the relatively strong concentration gradients in the PIT type wires [16]. Since the XRD experiments described here have no spatial resolution, the Sn content in different parts of the wire cannot be distinguished. The likely superposition of two diffraction peaks for high Sn content and low Sn content Nb_3Sn is indicated by a peak asymmetry, as shown in Figure 74.

The high resolution XRD recordings and the simple A15 cubic crystal structure of Nb_3Sn was expected to allow a crystallite size measurement in the $\text{Nb}_3\text{Sn}/\text{Cu}$ wires, as was already shown for RRP wires [45]. But a superposition of two close peaks at all Nb_3Sn diffraction peaks was

observed in the PIT wire diffraction patterns. This might also be explained by the division of the Nb₃Sn phase in two concentric rings within the filaments with strongly different crystallite size (see Figure 7). The position of the two superimposed peaks is in accordance with the lattice parameter of presumably two Nb₃Sn phases with a difference in Sn content of ~2 at.%. The intensity of the peaks however is not in accordance with the phase volume of the Nb₃Sn phases as it was determined by phase area measurements on metallographic cross sections. Other effects that influence the diffraction peak intensity might be an explanation but are not clarified yet.

In future experiments the Nb₃Sn formation in PIT wires could be analysed in more detail, by X-ray diffraction tomography [49]. Such experiments can provide diffraction patterns with spatial resolution, in order to provide a distinct view on the separately located Nb₃Sn phases with their different Sn content, crystallite size and texture.

7. Conclusion

The main goal of the work described in this thesis was the analysis of diffraction data acquired by synchrotron XRD *in situ* during the processing of Bi-2212/Ag superconducting wires. For the analysis of the different data sets, each containing hundreds of diffraction patterns, it was necessary to develop a semi-automatic software for peak fitting and tracking. Thanks to the very efficient XRD peak analysis program based on Excel-VBA that has been developed here, the scope of this thesis could be extended to analyse also diffraction data sets acquired previously during the processing of different Nb₃Sn/Cu superconducting wires.

The combination of XRD and μ -CT measurement has been particularly useful for the analysis of the partial melt processing of Bi-2212/Ag wires, as the different fundamentals allow a complementary view on the phases evolution during HTs. From the information obtained it can be concluded on the evolution of Bi-2212, Bi-2201 and Ag phases in detail. Especially the phase stability at varying temperature in different process gases and the influence of the heating and cooling rate and the filament diameter on the phase formations in Bi-2212/Ag round wires could be presented. μ -CT measurements gave a complementary view on the density evolution of the filaments powder filling and intersecting void space.

The Nb₃Sn formation in PIT and RRP type wires has been compared by XRD measurements during processing up to 900 °C. The results show a clear dependence of the filament diameter in the PIT wire on the Nb₃Sn growth rate, as well as a strong influence of the wire type, with a faster forming Nb₃Sn phase in RRP type wires.

8. Abbreviations

Elements	
Bi	Bismuth
Sr	Strontium
Ca	Calcium
Cu	Copper
O	Oxygen
Ag	Silver
Nb	Niobium
Sn	Tin
Ti	Titanium
N	Nitrogen
La	Lanthanum
B	Boride
Pb	Lead
Bi-2212	$\text{Bi}_2\text{Sr}_2\text{CaCu}_2\text{O}_x$ and slightly differing compositions
Bi-2201	$\text{Bi}_2\text{Sr}_2\text{Cu}_1\text{O}_x$ and slightly differing compositions
Units	
A	Ampere
μm	Micrometre
mm	Millimetre
m	Metre
K	Kelvin
$^\circ$	Degree
C	Celsius
T	Tesla
at.%	atoms per cent
wt.%	weight per cent
eV	electron volt
s	Second
min	Minute
h	Hour
\AA	Angstrom
Words	
e. g.	exempli gratia
approx.	approximately
multifil.	Multifilament
PIT	Powder-In-Tube
RRP	Restacked-Rod-Processing
RT	Room Temperature
HT	HT
XRD	X-ray diffraction
μ -CT	X-ray absorption micro tomography
LHC	Large Hadron Collider
CERN	Conseil Européen pour la Recherche Nucléaire
ICSD	Inorganic Crystal Structure Database
CF	Copper free phase

Variable	Name	SI-Unit
T	Temperature	°C
B	Field	T
B _A	Externally applied field	T
J _e	Critical engineering current density (across whole wire or cable)	A m ⁻²
J _c	Critical current density	A m ⁻²
I	Current	A
θ	Diffraction angle	°
d	Distance of lattice planes	Å
Q	Diffraction angle normalized to radiation wavelength	Å ⁻¹
T _c	Critical Temperature	K
h	1 st Miller index	1
k	2 nd Miller index	1
l	3 rd Miller index	1
a	Lattice parameter	m
b	Lattice parameter	m
c	Lattice parameter	m
ε	Strain	1
E	Energy	eV
FWHM	Full width at half maximum	Å ⁻¹
L	Crystallite size	m
K	Correction factor for Scherrer's Equation	1
λ	Wavelength	nm
B _{size}	Size induced FWHM broadening	radians
B _{strain}	Strain induced FWHM broadening	radians
ε	Strain	1
P _{O₂}	Oxygen partial pressure	bar

Constant	Name	Value	Unit
h	Planck constant	$4.135\ 667\ 43(35) \times 10^{-15}$	eV s
c ₀	Speed of light in vacuum	299 792 458 (exact)	m s ⁻¹
λ (Cu Kα ₁)	Wavelength of Cu Kα ₁ radiation	$1\ 537.400 \times 1.002\ 077\ 10(29) \times 10^{-13}$	m

9. Bibliography

- [1] LHC Design Report - Vol.I "The LHC main ring design report", CERN report.
- [2] CERN, Cross section of an LHC dipole in the tunnel, <http://cdsweb.cern.ch/record/1365795>, visited: 14.11.2012.
- [3] P. Lee and D. Larbalestier, Niobium-titanium superconducting wires: Nanostructures by extrusion and wiredrawing, P. Lee, D. Larbalestier, "Niobium-titanium superconducting wires: Nanostructures by extrusion and wiredrawing", *Wire Journal International* 36(2), (2003), 61-66.: Wire Journal International.
- [4] L. Bottura, G. d. Rijk, L. Rossi and E. Todesco, Advanced Accelerator Magnets for Upgrading the LHC, *IEEE Trans. Appl. Supercond.*
- [5] C. Scheuerlein, T. Boutboul, D. Leroy, L. Oberli and B. Rehmer, Hardness and tensile strength of multifilamentary metal–matrix composite superconductors for the Large Hadron Collider (LHC), *Journal of Materials Science*, Volume 42, Issue 12, pp 4298-4307 , 2007.
- [6] P. J. Lee, Engineering Critical Current Density vs. Applied Field, <http://fs.magnet.fsu.edu/~lee/plot/plot.htm>, visited: 08.05.2012.
- [7] K. Marken, M. Meinesz, B. Czabaj and S. Hong, Development of round multifilament Bi-2212/Ag wires for high field magnet applications, *IEEE Transactions on Applied Superconductivity*, 2005.
- [8] J. Parrell, Y. Zhang, R. Hentges, M. Field and S. Hong, Nb Sn strand development at Oxford Superconducting Technology, *IEEE Trans. Appl. Supercond.*, vol. 13, pp. 3470–3473, 2003.
- [9] M. H, M. R, M. M, C. B, H. S, R. M and B. J, Nexans precursor material, *Adv. Cryog. Eng.* 52B 673, 2006.
- [10] C. Scheuerlein, M. DiMichiel, M. Scheel, J. Jiang, F. Kametani, A. Malagoli, E. E. Hellstrom and D. C. Larbalestier, Void and phase evolution during the processing of Bi-2212 superconducting wires monitored by combined fast synchrotron micro-tomography and x-ray diffraction, IOP PUBLISHING, 2011.
- [11] T. Lang, B. Heeb, D. Buhl and L.J.Gauckler, The Role of Silver in the Processing and Properties of Bi-2212, *World Congress on Superconductivity*, Volume 2 p 753-761(SEE N96-10272 01-76).
- [12] F. kametani, T. Shen, J. Jian, C. Scheuerlein, A. Malagoli, M. D. Michiel, Y. Huang, H. miao, J. A. Parrell, E. E. Hellstrom and D. C. Larbalestier, Bubble formation within filaments of melt-

- processed Bi2212 wires and its strongly negative effect on the critical current density, *Supercond. Sci. Technol.* 24 (2011) 075009 (7pp).
- [13] D. P. Matheis and R. L. Snyder, X-ray powder diffraction analysis of the incommensurate modulated structure of Bi₂Sr₂CaCu₂O₈, 1994.
- [14] J. A. Slezak, J. Lee, M. Wang, K. McElroy, K. Fujita, B. M. Andersen, P. J. Hirschfeld, H. Eisaki, S. Uchida and J. C. Davis, Imaging the impact on cuprate superconductivity of varying the interatomic distances within individual crystal unit cells, *PNAS* March 4, 2008 vol. 105 no. 9 3203-3208 doi: 10.1073/pnas.0706795105.
- [15] J. Assal, Thermodynamic Optimization of the Ag-Bi-Sr-Ca-Cu-O System and Application to the Processing of Bi-2212 with Silver, Dissertation, 1998.
- [16] M. Cantoni, C. Scheuerlein, P.-Y. Pflüger, F. Borman, J. Rossen, G. Arnau, L. Oberli and P. Lee, Sn concentration gradients in Powder-in-Tube superconductors, *J. Phys.: Conf. Ser.* 234 022005 doi:10.1088/1742-6596/234/2/022005, 2010.
- [17] M. Di Michiel and C. Scheuerlein, Phase transformations during the reaction heat treatment of powder-in-tube Nb₃Sn superconductors, *Superconductor Science and Technology*, Volume 20, Number 10, October 2007, pp. L55-L58(4).
- [18] R. M. Scanlan, W. A. Fietz and E. F. Koch, Flux pinning centers in superconducting Nb₃Sn, *Journal of Applied Physics* Volume: 46, Issue: 5, 1975.
- [19] A. Godeke, Performance Boundaries in Nb₃Sn Superconductors, 2005.
- [20] C. Scheuerlein, M. D. Michiel, L. Thilly, F. B. X. Peng, E. Gregory, J. Parrell, I. Pong, B. Bordini and M. Cantoni, Phase transformation during the reaction heat treatment of Nb₃Sn superconductors, *J. Phys.: Conf. Ser.* 234 022032, 2010.
- [21] W. L. Bragg, The Diffraction of Short Electromagnetic Waves by a Crystal, *Proceedings of the Cambridge Philosophical Society*, 1913.
- [22] P. J. Mohr and B. N. Taylor, *Codata Recommended Values of the Fundamental Physical Constants*, NIST, 2005.
- [23] P. Debye and P. Scherrer, *Interferenzen an regellos orientierten Teilchen im Röntgenlicht. I.*, Göttingen, 1933.
- [24] W. Friedrich, P. Knipping and M. von Laue, *Interferenz-Erscheinungen bei Röntgenstrahlen*, *Sitzungsberichte der Mathematisch-Physikalischen Classe der Königlich-Bayerischen Akademie der Wissenschaften zu München* 1912: 303.

- [25] W. I. F. David, Powder Diffraction: Least-Squares and Beyond, J. Res. Natl. Inst. Stand. Technol, 2004.
- [26] T. Ungar, Microstructural parameters from X-ray diffraction peak broadening, Budapest: Elsevier Ltd., 2004.
- [27] P. Scherrer, Bestimmung der Größe und der inneren Struktur von Kolloidteilchen mittels Röntgenstrahlen, Göttingen, 1918.
- [28] J. Hubbell and S. Seltzer, Tables of X-Ray Mass Attenuation Coefficients and Mass Energy-Absorption Coefficients from 1 keV to 20 MeV for Elements $Z = 1$ to 92 and 48 Additional Substances of Dosimetric Interest, NIST; <http://www.nist.gov/pml/data/xraycoef/index.cfm>, visited: 24.05.2012.
- [29] A. Rack, Untersuchung komplexer Materialsysteme mittels Synchrotron-Tomographie und 3D-Bildanalyse, Dissertation, 2006.
- [30] T. Lundström, Structure, defects and properties of some refractory borides, 1985.
- [31] D. L. Kaiser and R. L. Watters, Certificate Standard Reference Material 660b, National Institute of Standards & Technology, 2010.
- [32] M. Rikel, S. Arzac, E. Soileux, J. Ehrenberg, J. Bock, K. Marken, H. Miao, C.-E. Bruzek, S. Pavard, A. Matsumoto, E. Hellstrom and L. Motowidlo, Effect of composition on the melting behaviour of Bi2212-Ag conductors, J. Phys.: Conf. Ser. 43 51 doi:10.1088/1742-6596/43/1/013, 2006.
- [33] W. Schmahl, M. Lehmann, S. Räth, M. Gerards and R. Riddle, An improved method to determine the weight fraction of 2212 and 2201 phase impurities in BSCCO-2223 powders from x-ray powder diffraction peaks, Supercond. Sci. Technol. 11 1269 doi:10.1088/0953-2048/11/11/013, 1998.
- [34] J. A. Parrell, Y. Zhang, M. B. Field, P. Cisek and S. Hong, High Field Nb₃Sn Conductor Development at Oxford Superconducting Technology, Applied Superconductivity, IEEE Transactions on , vol.13, no.2, pp. 3470- 3473, June 2003.
- [35] J. Lindenhovius, E. Hornsveld, A. den Ouden, W. Wessel and H. ten Kate, Powder-in-tube (PIT) Nb₃Sn conductors for high-field magnets, IEEE Transactions on Applied Superconductivity Volume: 10 , Issue: 1 , 2000.
- [36] T. Shen, J. Jiang, F. Kametani, U. P. Trociewitz, D. C. Larbalestier, J. Schwartz and E. E. Hellstrom, Filament to filament bridging and its influence on developing high critical current density in multifilamentary Bi₂Sr₂CaCu₂O_x round wires, 2009.

- [37] M. Di Michiel, J. M. Merino, D. Fernandez-Carreiras, T. Buslaps, V. Honkimäki, P. Falus, T. Martins and O. Svensson, Fast microtomography using high energy synchrotron radiation, *Rev. Sci. Instrum.* 76, 043702 (2005); <http://dx.doi.org/10.1063/1.1884194>.
- [38] M. Rikel, Private communication, Nov 2012.
- [39] P. Debye and I. Waller, Interferenz von Röntgenstrahlen und Wärmebewegung, *Annalen der Physik*, 1913.
- [40] A. A. Nayeb-Hashemi and J. B. Clark, *The Ag-Mg (Silver-Magnesium) system*, 1984.
- [41] E. Baker and M. Talukdar, *Inst. Mining Met. Trans. C* 77 (1968) 128.
- [42] T. Lang, D. Buhl and L. Gauckler, Melting of Bi-2212 under controlled oxygen partial pressures with silver, *Physica C: Superconductivity*, 1997.
- [43] J. K. Shin, S. Ochiai, M. Sugano, H. Okuda, Y. Mukai, M. Sato, S. S. Oh, D. W. Ha and S. C. Kim, Analysis of the residual strain change of Bi2212, Ag alloy and Ag during the heating and cooling process in Bi2212/Ag/Ag alloy composite wire, 2008.
- [44] J. Tenbrink and H. Krauth, Thermal expansion properties of Bi-2212 in Ag or an Ag-alloy matrix, 1994.
- [45] L. Thilly, M. Di Michiel, C. Scheuerlein and B. Bordini, Nb₃Sn nucleation and growth in multifilament superconducting strands monitored by high resolution synchrotron diffraction during in situ reaction, *Appl. Phys. Lett.*, 2011.
- [46] J. Charlesworth, I. Macphail and P. Madsen, Experimental work on the niobium-tin constitution diagram and related studies, *Journal of Materials Science*, July 1970, Volume 5, Issue 7, pp 580-603.
- [47] R. Flükiger, D. Uglietti, C. Senatore and F. Buta, Microstructure, composition and critical current density of superconducting Nb₃Sn wires, *Cryogenics*, Volume 48, Issues 7–8, July–August 2008, Pages 293–307.
- [48] N. Mitchell, Finite element simulations of elasto-plastic processes in Nb₃Sn strands, *Cryogenics*, Volume 45, Issue 7, July 2005, Pages 501–515.
- [49] S. D. M. Jacques, M. Di Michiel, A. M. Beale, T. Sochi, M. G. O'Brien, L. Espinosa-Alonso, B. M. Weckhuysen and P. Barnes, Dynamic X-Ray Diffraction Computed Tomography Reveals Real-Time Insight into Catalyst Active Phase Evolution, *Angewandte Chemie International Edition*, Volume 50, Issue 43, pages 10148–10152, October 17, 2011.

